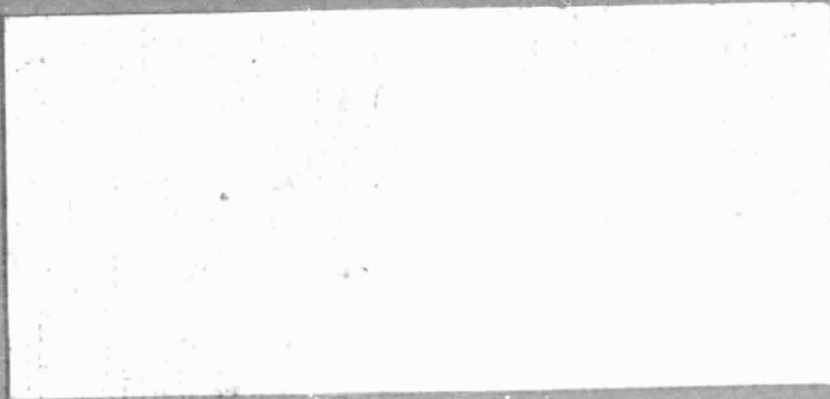


RAY W. HERRICK LABORATORIES

A Graduate Research Facility
of The School of Mechanical Engineering



Purdue University

West Lafayette, Indiana 47907

(NASA-CR-176295) PREDICTION OF SOUND FIELDS
IN ACOUSTICAL CAVITIES USING THE BOUNDARY
ELEMENT METHOD M.S. Thesis (Purdue Univ.)
163 p HC A08/MF A01 CSCL 20A

N86-13057

Unclas

15955

G3/71

TRANSMISSION OF SOUND THROUGH LIGHT AIRCRAFT
Purdue Research Foundation 520-1288-0353

PREDICTION OF SOUND FIELDS IN
ACOUSTICAL CAVITIES USING THE
BOUNDARY ELEMENT METHOD

Sponsored by

NASA

0353-1

HL 85-26

Submitted by:

Carl R. Kipp, Graduate Research Assistant
R.J. Bernhard, Principal Investigator

Approved by:

Raymond Cohen, Director
Ray W. Herrick Laboratories

August, 1985

PREDICTION OF SOUND FIELDS IN ACOUSTICAL
CAVITIES USING THE
BOUNDARY ELEMENT METHOD

A Thesis

Submitted to the Faculty

of

Purdue University

by

Carl R. Kipp

In Partial Fulfillment of the

Requirements for the Degree

of

Master of Science in Mechanical Engineering

August 1985

ACKNOWLEDGEMENTS

I would like to thank Dr. Robert J. Bernhard for serving as my major professor and for providing advice throughout this entire project. I would also like to thank Dr. Charles M. Krousgrill, Dr. James F. Hamilton and Dr. J. Stuart Bolton for serving on the advisory committee.

This research was funded by the Langley Research Center of the National Aeronautics and Space Administration (NASA) and I thank that organization for doing so.

Finally, but most importantly, I extend my most sincere heartfelt thanks to my fiancée, Ms. Paula Lewis. Throughout this endeavor, she has provided me with her love and support. During my times of bitter frustration, she was always ready with words of encouragement. She made it all worthwhile. I think I'll keep her.

TABLE OF CONTENTS

	Page
LIST OF FIGURES.....	v
LIST OF NOMENCLATURE.....	ix
ABSTRACT.....	xii
CHAPTER 1 - INTRODUCTION.....	1
CHAPTER 2 - LITERATURE REVIEW.....	4
2.1 Finite Element Methods in Cavity Acoustics.....	5
2.1.1 Duct Acoustics.....	6
2.1.2 Cavity Acoustics for Automotive Applications.....	10
2.2 Boundary Element Acoustics.....	13
2.2.1 Investigations of Exterior Acoustical Problems.....	16
2.2.2 Investigations of Interior Acoustical Problems.....	28
2.3 Conclusions.....	31
CHAPTER 3 - THEORY.....	33
CHAPTER 4 - NUMERICAL IMPLEMENTATION.....	42
4.1 Element Definition.....	42
4.2 Equation Discretization.....	46
4.3 Primary Numerical Integration Procedure.....	50
4.4 Singularity Numerical Integration Procedure.....	55
4.5 Solution Procedure.....	70
CHAPTER 5 - CASE STUDIES.....	72
5.1 Spherical Cavity Model.....	72
5.2 Spherical Model For Radiation.....	98
5.3 Rectangular Cavity Model.....	102
5.4 Summary.....	141

CHAPTER 6 - CONCLUSIONS.....142
LIST OF REFERENCES.....145

LIST OF FIGURES

Figure	Page
3.1 - Problem Description.....	34
4.1 - Local Isoparametric Element.....	43
4.2 - Global Isoparametric Element.....	44
4.3 - Integration Point Mesh.....	53
4.4 - Vectors For A Flat Element.....	57
4.5 - Singularity Cases.....	59
4.6 - Circular Domain Mesh.....	65
4.7 - Transformed Circular Domain Mesh.....	67
5.1 - Analytical Spherical Pressure Distribution For $k=8$	75
5.2 - Spherical Pressure Distribution For Pressure Boundary Conditions At $k=8$	77
5.3 - Spherical Pressure Distribution For Velocity Boundary Conditions At $k=8$	78
5.4 - Analytical Response For The Pressure At The Wall Of A Pulsating Spherical Cavity.....	82
5.5 - Numerical And Analytical Response For The Pressure At The Wall Of A Pulsating Spherical Cavity.....	84
5.6 - Spherical Cavity Pressure Distribution For Velocity Boundary Conditions At $kr=2$	86
5.7 - Spherical Cavity Pressure Distribution For Velocity Boundary Conditions At $kr=5.4$	87
5.8 - Spherical Cavity Pressure Distribution For Velocity Boundary Conditions At $kr=7.1$	88

5.9 - Pressure Distribution For A Sphere With Radiation Impedance Boundary Conditions At $k=0.583$	90
5.10 - Pressure Distribution For A Sphere With Radiation Pressure Boundary Conditions At $k=0.583$	92
5.11 - Pressure Distribution For A Sphere With Radiation Velocity Boundary Conditions At $k=0.583$	93
5.12 - Numerical Response For The Pressure At The Wall Of A Rigid-Walled Spherical Cavity.....	95
5.13 - Pressure Distribution In A Rigid-Walled Spherical Cavity With An Applied Source At $k_r=4.5$	96
5.14 - Analytical Pulsating Sphere Boundary Pressure Prediction For Radiation.....	100
5.15 - Numerical And Analytical Pulsating Sphere Boundary Pressure Predictions For Radiation.....	101
5.16 - Analytical Pressure Distribution For A Driven/Closed Cavity At $k=1$	105
5.17 - Analytical Pressure Distribution For A Driven/Closed Cavity At $k=2$	106
5.18 - Analytical Pressure Distribution For A Driven/Closed Cavity At $k=3$	107
5.19 - Pressure Distribution For First Box Model At $k=1$	109
5.20 - Pressure Distribution For First Box Model At $k=2$	110
5.21 - Pressure Distribution For First Box Model At $k=3$	111
5.22 - Pressure Distribution For Second Box Model At $k=1$	112
5.23 - Pressure Distribution For Second Box Model At $k=2$	113
5.24 - Pressure Distribution For Second Box Model At $k=3$	114

5.25 - Pressure Distribution For Third Box Model At k=1.....	115
5.26 - Pressure Distribution For Third Box Model At k=2.....	116
5.27 - Pressure Distribution For Third Box Model At k=3.....	117
5.28 - Rectangular Cavity Pressure Response - X Direction.....	121
5.29 - Rectangular Cavity Pressure Response - Y Direction.....	122
5.30 - Rectangular Cavity Pressure Response - Z Direction.....	123
5.31 - Rectangular Cavity Pressure Distribution At k=1.34 (XY Plane).....	126
5.32 - Rectangular Cavity Pressure Distribution At k=1.34 (XZ Plane).....	127
5.33 - Rectangular Cavity Pressure Distribution At k=1.34 (ZY Plane).....	128
5.34 - Rectangular Cavity Pressure Distribution At k=1.65 (XY Plane).....	130
5.35 - Rectangular Cavity Pressure Distribution At k=1.65 (XZ Plane).....	131
5.36 - Rectangular Cavity Pressure Distribution At k=1.65 (ZY Plane).....	132
5.37 - Rectangular Cavity Pressure Distribution At k=2.06 (XY Plane).....	134
5.38 - Rectangular Cavity Pressure Distribution At k=2.06 (XZ Plane).....	135
5.39 - Rectangular Cavity Pressure Distribution At k=2.06 (ZY Plane).....	136
5.40 - Rectangular Cavity Pressure Distribution At k=1 (XY Plane).....	138
5.41 - Rectangular Cavity Pressure Distribution At k=1 (XZ Plane).....	139

5.42 - Rectangular Cavity Pressure Distribution At
 $\alpha=1$ (ZY Plane).....140

LIST OF NOMENCLATURE

Symbol	Description
D	Problem domain
\bar{x}	Vector locating a point in the domain
B	Problem boundary
$\bar{\zeta}$	Vector locating a point on the boundary
\hat{n}	Normal vector at a point on the boundary
Ψ	Applied distributed source within the domain
Ψ_i	Applied monopole source strength
\bar{x}_s	Vector locating an applied source
Φ	Velocity potential
k	Wave number
δ	Dirac delta function
p	Pressure boundary condition
\bar{v}	Velocity boundary condition
j	The complex number $\sqrt{-1}$
ω	Circular frequency
ρ	Fluid density
r_{ij}	Distance between two points
σ	Source density distribution
c	Singularity integration 'free term'

B^-	Boundary excluding the region surrounding a singularity point
p^*	Fundamental pressure solution
v^*	Fundamental velocity solution
Ω	Solid domain angle
z	Impedance boundary condition
ϕ	A general variable
N_i	Lagrangian shape function
ξ	Local element coordinate
η	Local element coordinate
N	Number of boundary elements
M	Number of nodes per element
K	Number of applied sources
a_{il}	Numerical integration matrix term
d_k	Applied source vector term
α_l	Boundary condition vector term
g	General function
NG	Total number of integration points
ξ_i	Rectangular integration point coordinate
η_i	Rectangular integration point coordinate
w_i	Integration weighting factor
J	Jacobian
r	Radial integration point coordinate
θ	Angular integration point coordinate
j_0	Bessel's function of the first kind (0 order)
y_0	Bessel's function of the second kind (0 order)

r_0	Spherical surface radius
\bar{A}	Boundary condition constant
\bar{B}	Boundary condition constant
\bar{a}	Boundary condition constant
\bar{b}	Boundary condition constant

ABSTRACT

Kipp, Carl R. MSME., Purdue University, August 1985.
Prediction of Sound Fields in Acoustical Cavities Using
the Boundary Element Method. Major Professor: R. J.
Bernhard, School of Mechanical Engineering

A method is developed to predict sound fields in acoustical cavities. The method is based on the indirect boundary element method. An isoparametric quadratic boundary element is incorporated. Using this method, either pressure, velocity and/or impedance boundary conditions may be applied to a cavity. The capability to include acoustic point sources within the cavity is implemented.

The method is applied to the prediction of sound fields in spherical and rectangular cavities. All three boundary condition types are verified. Cases having a point source within the cavity domain are also studied. Numerically-determined cavity pressure distributions and responses are presented. The numerical results correlate well with available analytical results.

CHAPTER 1

INTRODUCTION

Sound fields in cavities affect many aspects of everyday life. It is well known that distribution of sound in an interior work environment can markedly influence the performance of those working within that environment. Most modern modes of transportation place the traveler in some form of cavity. The perceived comfort level of the traveler may again be influenced by the acoustical characteristics of the transporting cavity. Consequently, noise control engineers in the architectural and transportation industries become involved in optimizing acoustical cavities so as to minimize the possible negative effects on persons residing within those structures.

Computer aided design (CAD) procedures are very beneficial to individuals participating in noise control activities. Using CAD procedures, the acoustic characteristics of a cavity can be determined analytically, usually with less time and expense than required for experimentally-based techniques. Noise source identification can be accomplished with computerized modeling techniques. In addition, CAD procedures can readily be applied in optimizing the acoustical characteristics of a cavity after the noise sources have been identified.

The objective for the research presented here is the development of a numerical tool based on boundary element theory to predict the sound field within an acoustical cavity. The theory incorporates an indirect boundary element method utilizing isoparametric quadratic boundary elements. In addition to the usual boundary conditions of acoustic pressure and velocity, impedance boundary conditions are also formulated and implemented. Furthermore, capability to model acoustical point sources within the cavity domain is included. With all of the aforementioned features, the computer program developed during this research will provide a very useful tool for noise control activities.

The content of this thesis is organized in the following manner. Chapter 2 contains an extensive literature

review on numerical predictions of sound fields. The theoretical background of the indirect boundary element method for acoustics is presented in chapter 3. Numerical implementation of the indirect boundary element theory is presented in chapter 4. Chapter 5 presents case studies completed through the use of the computer program resulting from this research. Concluding remarks are given in chapter 6.

CHAPTER 2

LITERATURE REVIEW

Many researchers have been investigating techniques for numerical prediction of acoustic fields. Consequently, a significant body of technical and academic literature has been published. In contrast to numerical techniques developed for specific problems, such as Green's function methods and series solutions, the emphasis in this work will be generalized techniques. Such techniques are versatile and powerful and will someday play an important role in computer-aided noise control design. This chapter presents a review of the literature applicable to the numerical prediction of sound fields in acoustical cavities using generalized techniques. Two methods are used primarily, the finite element method and the boundary element method. The existing applications of each will be discussed.

2.1 Finite Element Methods in Cavity Acoustics

The finite element method is the most widely-known numerical tool available for engineering analysis of complex structures. A recent survey of finite element technology [1] contains a list of 155 textbooks and monographs relating to finite element technology. This list does not include the numerous journal articles relating to the topic. It is obvious from the survey that the finite element method (FEM) is now firmly rooted in various fields of engineering analysis.

In acoustics, the finite element method is an established analytical tool. Most commercially-available finite element codes (e.g., NASTRAN, ANSYS, SAP IV) are designed to be flexible, thereby providing the ability to solve various classes of problems. With an understanding of the specific code being utilized and the necessary acoustical fundamentals, a finite element code may be used to solve acoustical problems as shown by Bernhard [2].

The majority of finite element acoustical studies can be classified into two primary categories based on the application. These two categories are (1) duct acoustics and (2) cavity acoustics for automotive applications.

2.1.1 Duct Acoustics

A common analytical method used to analyze acoustical duct systems is four-pole network theory. In four-pole network theory, a transmission matrix can be used to define the relationships between the input and output variables of acoustic pressure and particle velocity for an acoustic device (e.g., a pipe, an expansion chamber, a Helmholtz resonator). The sound attenuation or transmission loss of a device may be determined using the transmission matrix. The transmission characteristics of an acoustical system comprised of a series of well-defined devices can be found by combining the respective transmission matrices.

Young and Crocker [3] employed the finite element method to determine the four-pole parameters of transmission matrices for expansion chambers. Since the initial studies were for simple expansion chambers, two-dimensional, four-node rectangular elements were used. Each element had twelve degrees-of-freedom: a pressure and two pressure gradients, one in each coordinate direction, at each of the nodes. Utilizing fourth-order Hermitian shape functions, the transmission loss of a rigid-wall expansion chamber was numerically evaluated and found to correlate well with theoretical results. The chamber was driven at the inlet with a harmonic velocity and

terminated at the outlet first with a rigid-wall boundary condition and then with a pressure release boundary condition.

As an extension of this work, Young and Crocker studied complicated muffler systems having multiple chambers [4]. Furthermore, the effects of non-rigid walls were included. Numerically, a multiple chamber system is assimilated by the cascade connection of the transmission matrices for the individual components. For a more complex system, the finite element method was well-suited for determining the four-pole parameters of the individual components to be used in calculating the transmission loss for the total system.

Astley and Eversman examined acoustical propagation above the cut-off frequencies in ducts in terms of the eigenvalue problem [5]. The research included the effects of steady mean flow or sheared flow within the duct. Capability was incorporated to study lined ducts by considering wall admittance. Two types of elements were considered. The primary element was a three-node element with quadratic shape functions. The variables in the formulation were the perturbed velocities in the x and y directions and the perturbed pressure. With the primary element, extraneous eigenvalues were found to result at relatively high frequencies. It was felt that the

extraneous eigenvalues were due to slope discontinuities in the quadratic shape functions. To overcome this difficulty, two-node elements incorporating shape functions having slope continuity were considered. The extraneous eigenvalues were eliminated although the solution accuracy was reduced at the higher eigenvalues. The finite element method proved to be applicable to the solution of an eigenvalue problem for ducts.

In addition to using acoustical finite elements, Craggs studied the use of absorptive finite elements for acoustical applications [6]. The implicit advantage of absorptive elements is that extended reaction of linings can be included. Most techniques supply the lining admittance as a boundary condition thereby only allowing for local reaction of the lining. Using the absorptive elements, the absorption coefficients for various resistivities of a constant thickness material were determined and found to compare quite well with analytical results. The acoustic and absorption finite elements were also coupled to study a lined expansion chamber. The transmission loss of the chamber as a function of lining resistivity was determined. Results for the lined expansion chamber would be very difficult to determine analytically. Thus, the advantage of the absorption finite element is evident.

The finite element method may also be used to examine the sound field within a duct as was shown by Cederfeldt [7]. Towards that objective, Cederfeldt studied a right-angle bend, a lined rectangular duct and an expansion chamber. The models were two-dimensional and comprised of four-node quadrilateral acoustic elements. Contour maps of the sound fields within the structures were presented. A variation of the right-angle bend created by adding a lining on the exterior corner provided quite a different sound field as compared to the bend without the lining. Even with the somewhat simplistic elements, dramatic representations of the sound fields were obtained.

A more sophisticated element was used by Ling, Hamilton and Allen to determine the sound field in axisymmetric ducts [8]. The element was a two-dimensional, isoparametric, axisymmetric element with cubic polynomials as the shape functions. With this element, the sound field in a bottle-like duct was determined numerically and compared with one-dimensional theoretical results and experimental measurements. Two types of lined ducts were also studied: (1) a duct with segmented lining (i.e., hard wall and impedance boundary conditions on different segments) and (2) a duct with an exponential distribution of absorbent material along its length. Both of the above lining conditions produce a pressure distribution within the duct which is difficult to obtain analytically but, as shown by

these researchers, can be obtained with the finite element method.

Whereas Ling, Hamilton and Allen used an isoparametric element, Doyle and Faulkner applied a subparametric element for acoustic pressure analysis [9]. The geometry variation within the element was linear while the pressure variation was made to be cubic under the philosophy that the subparametric element would be more computationally efficient than an isoparametric element. At each grid point, the four independent variables of pressure and the pressure gradient in each of the three orthogonal coordinate directions were used. An additional feature highlighted in this research is the ability to assign different fluid densities and speeds of sound at any grid point. With the method as described above, the eigenvalue problem for a uniform hard-walled duct was solved to find both the natural frequencies and the mode shapes of the duct. A second type of problem was analyzed where a harmonic velocity was assigned to one wall of the duct. The pressures in the duct were determined for a hard-walled case and cases with acoustic impedances on one or more walls.

2.1.2 Cavity Acoustics for Automotive Applications

Cavity acoustics problems for automotive applications are generally more complex than those for duct

acoustics problems. The geometry of the structures are not simple rectangular or cylindrical shapes. In addition, the interior of the cavity may contain obstacles affecting the sound field. Forcing functions can not normally be defined with ease when forced response problems are considered. For these reasons, the research presented below has been separated from the duct acoustics research presented in the previous section.

Craggs studied the sound field in a passenger car cavity when the cavity is coupled to the engine compartment through a flexible boundary [10]. The boundary motion was formulated in terms of the normal modes of the enclosure. The governing equations for a single enclosure with a flexible boundary and the structural coupling between two enclosures were developed. An example of a passenger car compartment coupled through a flexible boundary with the engine enclosure was then studied using the numerical formulation. The model could be used to study the sound field induced within the cavity due to an excitation within the engine compartment. From the results, some generalizations were made regarding the situations in which the passenger cavity either was or was not greatly influenced by the excitation in the engine compartment.

Sung studied finite element applications to the acoustics of a passenger car compartment and an engine

combustion chamber [11]. The NASTRAN finite element code was used for both cases. Three-dimensional models of the passenger compartment were constructed for two cases: (1) a compartment with a bench seat and (2) a compartment with bucket seats. The resonant frequencies of the cavities were determined and the corresponding mode shapes presented with an acoustic isobar representation. Inclusion of the seat in the model provided a more realistic situation than a model without the seat. For the combustion chamber model, a piston head with an asymmetric bowl was included in the chamber model. Again, the resonant cavity frequencies and mode shapes were determined from the finite element model. These resonant frequencies were compared with experimentally determined resonant frequencies and found to have good agreement. The final observation was that the acoustic finite element models were successful in predicting cavity boom frequencies in passenger compartments and knock-induced frequencies in a combustion chamber.

In conjunction with their work in duct acoustics, Doyle and Faulkner extended the research by studying the sound field in an automobile interior [9]. The first analyses performed were similar to those done by Sung [11] in that the resonant frequencies and mode shapes were quantified. However, more interesting results were obtained for a forced response problem. Experimentally determined

pressures at a sun roof opening were supplied to the finite element model as the forcing function. The acoustic field produced by the forced model was compared with a discrete number of points at which experimental data had been collected. Although the numerical pressures were slightly less than the experimental pressures, there was good correspondence between the two sets of data.

The above-cited references exemplify the types of acoustic cavity problems which may be studied with finite element techniques. Moreover, they indicate the popularity of finite element acoustics. The following section presents acoustical applications of the Boundary Element Method. Although not yet as popular as finite element techniques, boundary element techniques share many of the attractive features of the finite element method and are probably better adapted to certain problems.

2.2 Boundary Element Acoustics

There are two basic classifications of Boundary Element Methods: (1) Direct Boundary Element Methods (DBEM) and (2) Indirect Boundary Element Methods (IBEM). The distinction between the two methods must be made at this point for clarification of the following discussion. For the current project, an IBEM formulation is utilized as will be shown in Chapter 3.

The difference between the two classifications is evident in the integral equations. For the DBEM, "the unknown functions appearing in the integral equations are the actual physical variables of the problem" [12]. The physical variables for an acoustics formulation are the acoustic pressure and the particle velocity. A general form of the DBEM integral equation is

$$p(\bar{\xi}) = \int_B [p^*(\bar{x}, \bar{\xi})v(\bar{x}) - p(\bar{x})v^*(\bar{x}, \bar{\xi})] dB + \int_D p^*(\bar{x}, \bar{\xi})\Psi(\bar{x}) dD \quad (2.1)$$

where $p(\bar{\xi})$ is the pressure at any point, $p(\bar{x})$ is the pressure at a boundary point, $v(\bar{x})$ is the normal velocity at a boundary point, $p^*(\bar{x}, \bar{\xi})$ and $v^*(\bar{x}, \bar{\xi})$ are the respective fundamental pressure and velocity functions from a boundary point to any point and $\Psi(\bar{x})$ represents applied source strengths over the domain of the problem.

The formulation for an IBEM is significantly different from that for a DBEM. For the IBEM,

"The integral equations are expressed entirely in terms of a unit singular solution of the original differential equations distributed over the boundaries of the region of interest. The density functions themselves have no specific physical significance but once they have been obtained from a numerical solution of the integral equations the values of the solution parameters anywhere within the body can be calculated from them by simple integration processes." [12]

Or, in other words, the boundary is replaced by a distribution of sources which reproduce the specified boundary

solution and allow computation of the physical variables anywhere in the problem domain or boundary. Separate equations are required for portions of the boundary depending upon the specified boundary conditions on the particular portion of the boundary. The general form of the IBEM integral equation for a pressure boundary condition is

$$p(\bar{\xi}) = \int_B \sigma(\bar{x}) p^*(\bar{x}, \bar{\xi}) dB + \int_D p^*(\bar{x}, \bar{\xi}) \psi(\bar{x}) dD \quad (2.2a)$$

whereas the general equation for a velocity boundary condition is

$$v(\bar{\xi}) = \pm c \sigma(\bar{x}) + \int_B \sigma(\bar{x}) v^*(\bar{x}, \bar{\xi}) dB + \int_D v^*(\bar{x}, \bar{\xi}) \psi(\bar{x}) dD \quad (2.2b)$$

where $\sigma(\bar{x})$ represents the fictitious source density functions at the boundary points and c represents an integration constant due to integral singularities which will be further explained in chapter 3.

Although the details of the two formulations are not critical at this point, an understanding of the existence of differing formulations is important. Some of the following reviewed works use a DBEM while others use an IBEM. This point will be emphasized within each review.

2.2.1 Investigations of Exterior Acoustical Problems

Most of the boundary element research heretofore published has dealt with the acoustic field of a domain exterior to a vibrating or scattering structure. Primarily, this is a consequence of the capability of boundary element methods to model domains extending to infinity, a task not easily accomplished with finite element models. However, the integral formulations of interior regions are nearly equivalent to those for exterior regions. Hence, much of the development for exterior regions may be extrapolated to developments for interior regions.

Chen and Schweikert [13] were the earliest contemporary researchers to apply boundary element techniques to acoustic radiation problems. A numerical implementation of Huygen's principle, which is essentially a primal IBEM formulation, was utilized whereby a distribution of simple sources was imagined over the bounding surface. The surface itself was considered to be an array of triangular elements over which a uniform velocity with a constant phase angle was prescribed on each element. Each element was analogous to a rigid piston vibrating with a constant harmonic behavior. After defining a model by its geometry and boundary conditions, the boundary integral equations were numerically evaluated to calculate the simple source

distribution over the model boundary. The field pressures were quantified from the source distribution on the boundary. Two examples were given. The first example consisted of a piston in a rigid sphere for which the exterior field pressure radiation pattern was calculated. Likewise, similar exterior pressure patterns were determined for a stiffened cylinder immersed in water. The fluid-structure interface effects were included for the second example.

A DBEM was incorporated into a study of acoustic radiation from surfaces of revolution by Chertock [14]. The variables in the integral equations for a DBEM represent the acoustic pressure and particle velocity. So by specifying one type of boundary condition, the remaining unknown boundary condition may be determined with the Helmholtz integral equations. Furthermore, the field pressures can be calculated based on the boundary parameters. Chertock used this procedure to numerically evaluate the surface pressures and field pressures from the velocity boundary conditions for rigid-body vibration of a sphere, quadrupole vibration of a prolate spheroid (i.e., a cigar-shaped surface) and quadrupole vibration of an axisymmetric surface which was unsymmetric about all axes except the major axis. Surfaces of revolution were studied because theoretical results may be obtained for comparison with numerical results. Good correlation was found

between the numerical and theoretical solutions for the cases in question.

Copley [15] also applied a DBEM to the study of acoustic radiation from axisymmetric radiators. However, Copley [15] used an approach which differed from that of Chertock [14]. Copley utilized the Interior Helmholtz integral equation whereas Chertock utilized the Surface Helmholtz integral equation. In the interior Helmholtz integral approach, the field points of integration lie within the boundary of the vibrating body and, in fact, are located along the axis of symmetry for axisymmetric radiators. The corresponding field points lie on the boundary in the surface Helmholtz integral approach. Hence, the appropriate titles of each approach refer to the location of the field integration points. Using the Interior Helmholtz integral equation, the acoustic radiation from a spheroid and a finite cylinder with a capped end were studied. The farfield directivity pattern of the finite cylinder was compared to results obtained by Williams, et.al. using a method based on expansion in spherical harmonics [16]. Generally, the results correlated well with the exception of some discrepancy which was thought to be due to differences in which the velocity distributions were prescribed.

Taking a more general point of view, Copley [17] also studied failures which occur with integral formulations for acoustic radiation problems. At certain frequencies, the integral formulations are unable to represent the steady-state harmonic radiation from a finite, smooth, closed surface on which normal velocity is prescribed. These failures occur at the interior Dirichlet eigenfrequencies for both the IBEM and the Surface Helmholtz integral equation which is a DBEM. Copley [17] presented proofs that the failures were due to nonexistence of sources for the IBEM and as nonuniqueness of sources and doublets for the Surface Helmholtz integral equation. The failures are inherent in the formulations and do not represent physical attributes of the problem. However, the Interior Helmholtz integral formulation used by Copley [15] does not suffer from these failures.

Proofs similar to those of Copley [17] were presented by Burton and Miller [18]. Moreover, suggestions to overcome the failures were made. One alternative consisted of overdetermining the system of equations by using both the Surface Helmholtz integral equations and its differentiated form. The second but more economical alternative was to combine the two types of equations into a single set of equations which would not overdetermine the system. No computational examples were provided for these approaches.

A combined Helmholtz integral equation formulation was developed by Schenck [19] to overcome the deficiencies of the above mentioned formulations. The technique initially applied the Surface Helmholtz integral equations and then overdetermined the system of equations with the Interior Helmholtz integral equations. The overdetermined set of equations was solved by a least squares orthonormalizing procedure to evaluate the surface pressures. From the surface pressures, the field pressures were calculated with the Helmholtz integral equation. Essentially, the described procedure is a DBEM as all the equations are of the direct formulation type. A number of numerical examples were presented for the combined Helmholtz integral equation formulation of which only three will be discussed. The first example is a uniformly vibrating sphere. The problem illustrates the advantage of the combined equation formulation. At a characteristic wave number, the Surface Helmholtz integral equations fail to yield the correct surface pressure. However, the combined Helmholtz integral formulation was capable of correctly solving for the surface pressure on the sphere by specifying only one point within the sphere. A second example of a right circular cylinder with rigid ends on which velocity boundary conditions were prescribed was studied. The resulting far-field pressure pattern was found to be consistent with that obtained by Chertock [14] but inconsistent with that

obtained by Williams, et.al. [16]. As a variation on this model, the velocity distribution was revised to reflect the velocities that would occur at the boundary if a source were at the center of the cylinder and the cylinder was not physically present. The acoustic pressure radiation pattern was equivalent to a pattern for a simple source as was expected. A rectangular parallelepiped was the third model considered. Again, the velocity distribution due to a simple source was assigned on the boundary. The resulting radiation pattern was the expected simple source radiation pattern. For both of the latter cases, the Surface Helmholtz integral equation without the interior points failed at the characteristic wave numbers.

The concept of overdetermination of the system equations was also addressed by Piaszczyk and Klosner [20]. The overdetermining equations were developed with the Exterior Helmholtz integral equations unlike Schenck's research which used the Interior Helmholtz integral equations for the overdetermination [19]. An iterative procedure is required in the method proposed by Piaszczyk and Klosner [20]. At the surface, an approximate acoustic fluid impedance was assumed. The Exterior Helmholtz integral equations were used to solve for approximate pressures at selected field points. The approximate field pressures were then applied in conjunction with the Exterior and Surface Helmholtz integrals to solve for the

surface pressures. A least squares procedure was required to calculate the surface pressures. The surface pressures were then substituted into the overdetermined set of equations to solve for the field pressures which were considered to be the next iterative value of the field pressures. The entire iterative process continued until a convergence was established. For this exterior overdetermination scheme, the selection of the overdetermining points is not critical due to its iterative nature. Thus, the scheme may be applied without loss of generality to structures of arbitrary shape. A number of computational examples were presented displaying the versatility and accuracy of the exterior overdetermination method.

The research of Schenck [19] was used in combination with finite element analysis to study acoustic radiation from sonar transducers by Smith, Hunt and Barach [21]. Although the combined Helmholtz integral equation formulation was applied, only the Surface Helmholtz integral equations were utilized in the sonar transducer study. A specific acoustic impedance matrix was derived with the integral equations. Definition of consistent mass and stiffness matrices for the complex structures came from the finite element analysis. The total structural-acoustical system of equations combined the mass and stiffness matrices with the acoustic loading included as surface loading forces. Finally, the pressure radiation

patterns were determined using the results of the structural-acoustical analysis and the Helmholtz integral equations to evaluate the pressures at points in the field surrounding the transducer. Numerical results for a piezoelectric sphere and a piezoelectric free-flooded cylinder were compared with experimental results and found to agree within 5 per cent. Some of the error was attributed to the piezoelectric nature of the material in the transducers.

Engblom and Nelson [22] expanded upon the work of Smith, Hunt and Barach [21] by the addition of two features. The first additional feature involved allowing quadratic variation of the acoustic variables and linear variation of the geometrical variables over the surface of an element. Prior to this work, a constant variation of the acoustic variables had been assumed. In doing so, discontinuities of acoustic variables may arise at the boundary of neighboring elements. A quadratic variation ensures that the acoustic variables become continuous at the element boundaries. The second feature added was a coordinate transformation used to integrate around the singularity which exists in the Helmholtz integral formulations. Since the elements were triangular, the coordinate transformation involved a change from area coordinates to polar coordinates. In doing so, the singularity was removed thus allowing the integration to be completed

without the singularity complications. The common examples of acoustic radiation from a sphere and a right circular cylinder were numerically evaluated with good results.

Unlike the approach originally developed by Schenck [19] to overcome the difficulty of nonuniqueness, Meyer, Bell, Zinn and Stallybrass [23] implemented an approach suggested by Burton and Miller [18]. That is, the system of equations consisted of the Surface Helmholtz integral equation and its differentiated form, both of which were direct formulations. The system of equations was not an overdetermined set but a combination of the two types of integral equations. A difficulty arose in that the differentiated form of the Surface Helmholtz integral equation contained a strong singularity which could not be directly numerically integrated. Nevertheless, the authors proved through rigorous mathematics and computational considerations that the integration was possible. For an example of a piston set in a rigid sphere, the error for the numerical farfield pressures remained less than 10 per cent as compared with exact analytical solutions.

One further refinement of the DBEM for acoustic radiation problems was achieved by Seybert, Soenarko, Rizzo and Shippy [24]. The authors provided further sophistication in the discretization process through the use of an isoparametric element. With the isoparametric element,

both the geometry and the acoustic variables were interpolated with quadratic shape functions. Although not immediately apparent, the isoparametric element is somewhat more refined than the element used by Engblom and Nelson [22] which used a linear geometrical variation. Consequently, efficiency and accuracy were increased as less elements were required to model curved or other irregular surfaces. To illustrate the isoparametric element capability, the examples of a pulsating sphere and an oscillating sphere were considered and found to compare well with theoretical results except at the characteristic wavenumbers. The nonuniqueness of the formulation was not accounted for by these authors.

The preceding reviews in this section represent the advances which have occurred in boundary element technology for exterior domain acoustics, particularly for radiation problems. Many of the same authors have also studied scattering problems. Thus far, the theoretical implications have been discussed. The remaining portion of this section will review applications of the aforementioned theory to somewhat more complicated problems.

A DBEM has been used by Seznec [25] to study the diffraction of sound around barriers. The barriers were any general type or shape used for noise abatement (e.g., a barrier around a roadway to hinder traffic noise). The

capability to include reflectivity and absorptivity effects of both the ground and the barrier was achieved through the application of impedance boundary conditions on the surfaces. Prior to the work of Sez nec, researchers had been unable to adequately account for the reflectivity and absorptivity effects. The diffraction of sound around barriers of various shapes were determined. For one barrier, that of a infinitely thin reflecting barrier, the numerical solution was favorably compared with solutions already existent in the literature. Overall, the DBEM was found to be effective as a design tool in studying the diffraction of sound around barriers.

Sadek and his coworkers developed a procedure to predict the acoustic emission from a machine using the design drawings for the machine [26]. A finite element model of the machine structure was used to predict the structural modes of vibration and the modal response to typical operating loads for the machine. The modal response yielded the surface velocities which were used as boundary conditions for a DBEM formulation to predict the acoustic emission. Two applications of the procedure were presented. The first example was for a forging machine structure under impulse loading characteristic of the machining operation. Reflections of sound from the ground could be and were included in determining the acoustic emission. Comparison of the numerical results with

experimental results showed that each exhibited the same general trends and magnitudes although there were variations at specific points. The second application involved studying the acoustic emission from one component of a hydraulic hammer [27]. The component considered to be the most offending noise source was studied. The acoustic emission analysis procedure was applied to the initial design and possible redesign configurations. As a result of these analyses, one redesign configuration quantitatively produced less acoustic emission than the initial design and the other redesigns. The process followed in this work emphasizes the manner in which a boundary element method may be used in the design process.

A method to predict acoustic intensity on the surface of a vibrating body utilizing a DBEM formulation has been developed by Benner and Koopmann [28,29]. Much like the previously presented research, a finite element code was used to define the dynamics of the structure. Since determination of acoustic intensity requires both the pressure and velocity, both of these quantities were calculated with the boundary element computer code. In addition, acoustic pressure and velocity, and hence acoustic intensity, were calculated at any field point. The boundary element acoustic intensity method was applied to the study of crack propagation along the boundary of a flat plate [30]. To simulate crack propagation, successive collinear

degrees-of-freedom were released within the finite element model. The acoustic surface intensity was calculated for various modes of vibration as each additional degree-of-freedom was released. A definite change in the intensity distribution occurred as the crack propagated. This application highlighted the possible use of a boundary element program as a tool in analyzing cracked or flawed structures for non-destructive testing. A second application was to study the radiation characteristics of a slender box-type structure representative of a box girder in a rapid transit transportation system [31]. The intent was to isolate high radiation efficiency modes so that damping treatments could concentrate on reducing those modes. Relatively high radiation efficiency modes were identified using the boundary element formulation but analysis of the structure with damping was not presented. This application highlights one manner in which boundary element formulations may be used for design modifications.

2.2.2 Investigations of Interior Acoustical Problems

The preceding section and the vast majority of literature relating to boundary element technology for acoustical applications consider exterior domain problems. The following discussion reviews literature applied to acoustical problems in the interior domain.

Tai and Shaw [32] have used a DBEM formulation to determine eigenvalues and eigenmodes of the Helmholtz equation for arbitrary domains. The technique is applicable to both two- and three-dimensional domains. However, the numerical example presented was for a two-dimensional domain. Within an element, the acoustic variable was considered to be constant. The numerical example presented consisted of a right triangle along whose hypotenuse the eigenmodes were determined after the eigenvalues had been found. The first two modes were found for three cases having varying magnitudes of the acute angles. This problem was so chosen to emphasize that the integral formulation is capable of providing results when a separation of variables approach is not. The separation of variables technique can be used when the boundaries are along constant coordinate lines thereby allowing the equations to separate into individual coordinate directions. For the case of a right isosceles triangle, which has a known analytical solution, the numerical solution with the DBEM formulation and analytical solution showed excellent agreement.

Tanaka, Fujikawa, Abe and Utsuno developed a method incorporating a DBEM formulation to calculate the transfer matrices used in analyzing muffler systems [33]. This method was found to yield good accuracy and better efficiency than the finite element approach applied by Young

and Crocker [3,4]. Boundary element theory was applied in regions where it is difficult to apply plane-wave theory. Plane-wave theory was applied in regions where that theory was still applicable. The transfer matrix for the entire system was obtained by multiplying the matrices from each component and used to calculate the insertion loss. Impedance boundary conditions were included for some cases. The method combining boundary element and plane-wave theory gave good results and also decreased both modeling and computational time as compared to other numerical techniques.

Sestieri, Del Vescovo and Lucibello have considered the problem of structural-acoustical coupling in cavities by application of a DBEM [34]. The effects of the acoustic loading were included as forces on the structure in an inhomogeneous Helmholtz formulation (i.e., a forced acoustical problem). An overdetermination procedure similar to that used by Schenck [19] was used whereby the resulting pressures were a least squares solution of the problem. Constant acoustic variable variation was implied on an element surface. Impedance boundary conditions were also included. A series of studies involving a cylindrical cavity excited by a harmonic driver at one end produced very good agreement with experimentally obtained results. Other studies investigating the quantity and placement of

the interior overdetermining points were also presented but will not be discussed here.

2.3 Conclusions

This chapter has presented a number of references related to prediction of sound fields in cavities and boundary element applications in acoustics. It reviews the status of techniques being applied to the problems within the concern of the current research. In addition to the technical literature, there are good academic references available relevant to boundary element techniques for both general and specific topics [12,35,36].

A few developments from the literature review should be emphasized due to their significance to the current research. IBEM's require less information than DBEM's. Equations 2.1 and 2.2 illustrate that less information is required in the integral equations. More importantly, only one quantity, the surface source distribution, is initially computed at the boundary whereas, for DBEM's, both pressure and its gradient, depending on the boundary condition, are resultants. Hence, the IBEM may be preferred for noise source identification since interpretation of the results would be more straightforward. Impedance boundary conditions have been applied in past research and will be applied in the current research. The information relating to the failures of the boundary element

formulations may provide guidance in case difficulties of this nature are encountered. The literature review has shown that isoparametric representation, which is to be utilized in the current research, has been previously utilized successfully. One very important concept discovered during this review is that of domain transformation to integrate around the singularity inherent in the Helmholtz integral formulations. A similar approach will be used and is detailed in chapter 4. Finally, the literature review shows a definite lack of boundary element applications to acoustical cavity problems. Of the 21 boundary element references cited, only 3 were concerned with cavities.

CHAPTER 3

THEORY

The problems to be considered are those dealing with acoustical behavior within cavities. A description of the problem is shown in Figure 3.1. A point within the domain D is located by the vector \bar{x} . Likewise, a point on the boundary B is defined by the vector \bar{r} . The vector normal to the boundary is signified by \hat{n} and is considered to be directed outward from the cavity. An applied distributed source of strength Ψ within the domain is located by the vector \bar{x}_s .

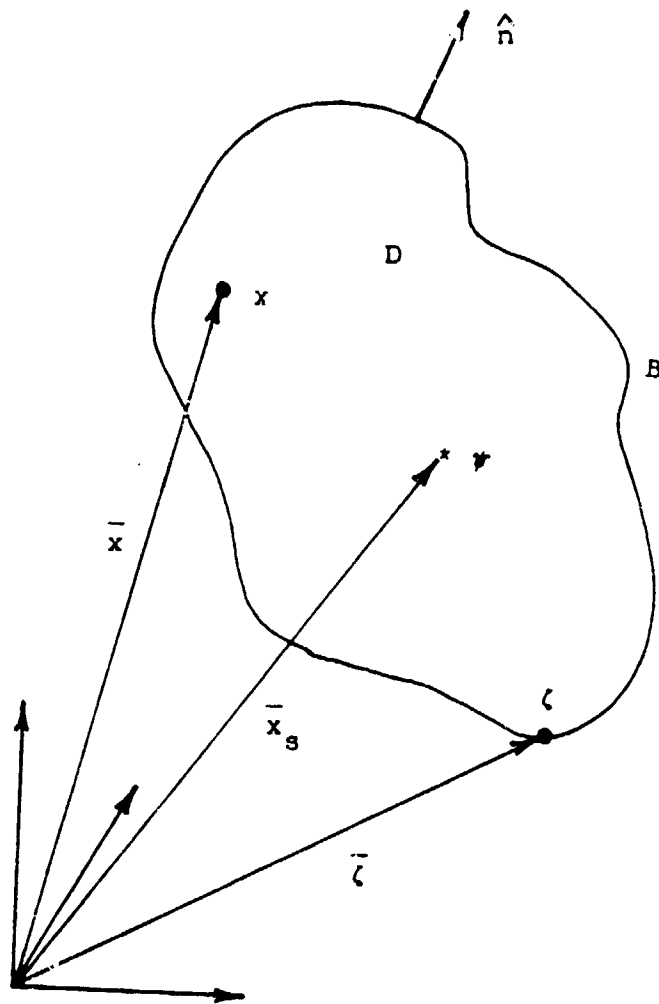


Figure 3.1 - Problem Description

For a problem of this type, the governing equation is the familiar non-homogeneous Helmholtz equation.

$$\nabla^2 \Phi + k^2 \Phi = \Psi(\bar{x}_s) \quad (3.1)$$

where \bar{x}_s is the vector locating the applied source. Equation 3.1 is the linearized, lossless Helmholtz equation formulated in terms of velocity potential, Φ . The variables of acoustic pressure and particle velocity can be related to the velocity potential through the relationships [37]

$$p = -j\omega\rho\Phi \quad (3.2)$$

$$\bar{v} = \nabla\Phi. \quad (3.3)$$

A Huygen's principle formulation which may be used to solve the homogeneous form of equation 3.1 has been developed by Chen and Schweikert [13]. In this formulation, a distribution of simple sources is considered to exist at the boundary of the cavity in question. The boundary source magnitudes are determined in such a way that the boundary conditions for the problem are satisfied. Chen and Schweikert's method is essentially a simple indirect boundary element method. To develop a more complete indirect boundary element method, a variable distribution of sources may be assumed as will be shown in Chapter 4. The velocity potential at any point due to the assumed source distribution is

$$\Phi(\mathbf{x}) = \int_B \sigma(\zeta) \frac{e^{-jk r}}{r} dB \quad (3.4)$$

where r is the distance between the points $\bar{\mathbf{x}}$ and $\bar{\zeta}$ and $\sigma(\zeta)$ is the source strength. Although equation 3.4 is written for a point in the domain, it applies equally as well for a point on the boundary. Similarly, the gradient of the velocity potential is

$$\nabla\Phi(\mathbf{x}) = 4\pi c\sigma(\mathbf{x}) + \int_{B^-} \sigma(\zeta) \nabla \left[\frac{e^{-jk r}}{r} \right] dB \quad (3.5)$$

where c results from a singularity integration which will be defined further in this chapter and B^- is the boundary excluding a small region at the singularity.

At this stage, a definition of two quantities will be made to ease notational difficulties. Combination of equations 3.2 and 3.4 allows an integral representation of the pressure at a point to be expressed as

$$p(\mathbf{x}) = -j\omega\rho \int_B \sigma(\zeta) \frac{e^{-jk r}}{r} dB. \quad (3.6)$$

A quantity known as the fundamental pressure solution, p^* , is defined by

$$p^*(\bar{\zeta}, \bar{\mathbf{x}}) = -j\omega\rho \frac{e^{-jk r}}{r}. \quad (3.7)$$

Hence, equation 3.6 may be more concisely written as

$$p(\mathbf{x}) = \int_B \sigma(\zeta) p^*(\bar{\zeta}, \bar{\mathbf{x}}) dB. \quad (3.8)$$

Likewise, the fundamental velocity solution, v^* , may be defined by considering the partial derivative within the integral portion of equation 3.5, that is

$$\nabla \left[\frac{e^{-jkx}}{r} \right] \quad (3.9)$$

Since, for a well-posed boundary value problem, the component of velocity of interest is the normal velocity, the following relationship from Kaplan [38] is used.

$$\frac{\partial(\quad)}{\partial \hat{n}} = \nabla(\quad) \cdot \hat{n} \quad (3.10)$$

Using equations 3.9 and 3.10, the fundamental velocity solution may be defined as

$$v^*(\bar{\zeta}, \bar{x}) = \hat{n} \cdot \nabla_r \left[\frac{-1}{r^2} - \frac{jk}{r} \right] e^{-jkx} \quad (3.11)$$

Equation 3.5 may now be written more concisely as

$$v(x) = 4\pi c \sigma(x) + \int_{B^-} \sigma(\zeta) v^*(\bar{\zeta}, \bar{x}) dB \quad (3.12)$$

where v is the normal velocity component of the velocity potential gradient in equation 3.3.

The quantity c in equation 3.12 results from integration around a singularity point. From examination of the fundamental solutions, it is evident that as the distance between the two points of concern approaches zero the fundamental solutions become infinite. However, the fundamental pressure solution is a $\frac{1}{r}$ singularity while the fundamental velocity solution is a $\frac{1}{r^2}$ singularity. The $\frac{1}{r}$

singularity is weak and may be integrated but the $\frac{1}{r^2}$ singularity is strong and must be treated as a Cauchy principal value [40]. The basic premise is to exclude a small region surrounding the singularity from the integration and account for the exclusion with the added 'free term' (i.e., the quantity c) [41,42]. Evaluation of the 'free term' for an interior domain can be done with the following rules.

- $c = 0$ for an exterior point
- $c = -1$ for an interior point
- $c = -\frac{1}{2}$ for a point on a smooth boundary
- $c = -\frac{\Omega}{4\pi}$ for a point on a corner

A smooth boundary is any boundary with a unique tangent plane. For a corner point, Ω is the value of the solid angle included in the domain at the corner expressed in steradians.

The previous discussion is for the homogeneous problem but the inhomogeneous problem can be solved by augmenting equations 3.8 and 3.12 with a domain integral [39]. The domain integral represents the contribution of an applied distributed source of strength ψ . After including the domain integral, the equations become

$$p(\mathbf{x}) = \int_B \sigma(\zeta) p^*(\zeta, \mathbf{x}) d\mathbf{B} + \int_D \psi(\mathbf{x}_s) p^*(\mathbf{x}_s, \mathbf{x}) dD \quad (3.13)$$

and

$$v(\mathbf{x}) = 4\pi c \sigma(\mathbf{x}) + \int_B \sigma(\zeta) v^*(\zeta, \mathbf{x}) d\mathbf{B} + \int_D \psi(\mathbf{x}_s) v^*(\mathbf{x}_s, \mathbf{x}) dD \quad (3.14)$$

where $\bar{\mathbf{x}}_s$ indicates the location of the applied source.

If the applied sources are considered to be monopole sources, evaluation of the domain integral is significantly simplified. For a point source, the domain integral is easy to evaluate as the point source may be represented by a Dirac delta function multiplied by the source strength. Thus, the integral exists only at the point of application of the source. The domain integral becomes

$$\int_D \psi(\bar{\mathbf{x}}_s) p^*(\bar{\mathbf{x}}_s, \bar{\mathbf{x}}) dD = \sum_{i=1}^{n_{\text{source}}} \int_D \psi_i \delta(\bar{\mathbf{x}}_{s_i} - \bar{\mathbf{x}}) p^*(\bar{\mathbf{x}}_s, \bar{\mathbf{x}}) dD = \sum_{i=1}^{n_{\text{source}}} 4\pi \psi_i p^*(\bar{\mathbf{x}}_{s_i}, \bar{\mathbf{x}}) \quad (3.15)$$

for a pressure boundary condition and

$$\int_D \psi(\bar{\mathbf{x}}_s) v^*(\bar{\mathbf{x}}_s, \bar{\mathbf{x}}) dD = \sum_{i=1}^{n_{\text{source}}} \int_D \psi_i \delta(\bar{\mathbf{x}}_{s_i} - \bar{\mathbf{x}}) v^*(\bar{\mathbf{x}}_s, \bar{\mathbf{x}}) dD = \sum_{i=1}^{n_{\text{source}}} 4\pi \psi_i v^*(\bar{\mathbf{x}}_{s_i}, \bar{\mathbf{x}}) \quad (3.16)$$

for a velocity boundary condition where n_{source} is the total number of applied sources. Distributed internal sources are not difficult to evaluate but are rare.

Vibrating sources which do not behave as point sources can be treated as additional boundaries.

Impedance boundary conditions may also be applied with this IBEM. Specific acoustic impedance is defined as the ratio between pressure and particle velocity [43] or

$$z = \frac{p}{v}. \quad (3.17)$$

Manipulation of equation 3.17 yields an equation which is applicable to the integral equations.

$$p - zv = 0 \quad (3.18)$$

In terms of the integral equations, impedance boundary conditions may be formulated as

$$-4\pi z c \sigma(x) + \int_B \sigma(\zeta) \left[p^*(\zeta, \bar{x}) - z v^*(\zeta, \bar{x}) \right] dB + \sum_{i=1}^{n_{\text{source}}} 4\pi \Psi_i(\bar{x}_{s_i}) \left[p^*(\bar{x}_{s_i}, \bar{x}) - z v^*(\bar{x}_{s_i}, \bar{x}) \right] = 0. \quad (3.19)$$

Equation 3.19 can be solved for the unknown fictitious source distribution σ .

All the integral equations have now been developed for this indirect boundary element formulation. Depending on the type of boundary condition applied, equations 3.13, 3.14 and/or 3.19 are used to solve for the assumed source density distribution, σ , on the boundary of the body in question. Once the source density distribution has been evaluated, the same three equations may be applied to solve for both the unknown boundary conditions and the

acoustic variables at desired points within the domain. The numerical implementation of the preceding theory is presented in the next chapter. For the purpose of the current research, only the acoustic pressures at the boundary and field points will be evaluated as those quantities adequately describe the sound field within the cavity.

CHAPTER 4

NUMERICAL IMPLEMENTATION

The preceding chapter describes the theory of the indirect boundary element formulation of the cavity acoustics problem. To implement the theory into a usable computer procedure, a number of numerical analysis techniques were applied. This chapter presents the details of the numerical analysis techniques which were used for the implementation.

4.1 Element Definition

The boundary element incorporated into this research is an isoparametric element with quadratic shape functions. The term isoparametric means the same interpolation function is employed for both the geometric approximation and the acoustic variable approximation. For an isoparametric element, the number of nodes is equal in both

the local and the global coordinate systems. Consequently, a node in the local coordinate system correlates directly to a node in the global system. The local element is shown in figure 4.1. An example of a global element is shown in figure 4.2.

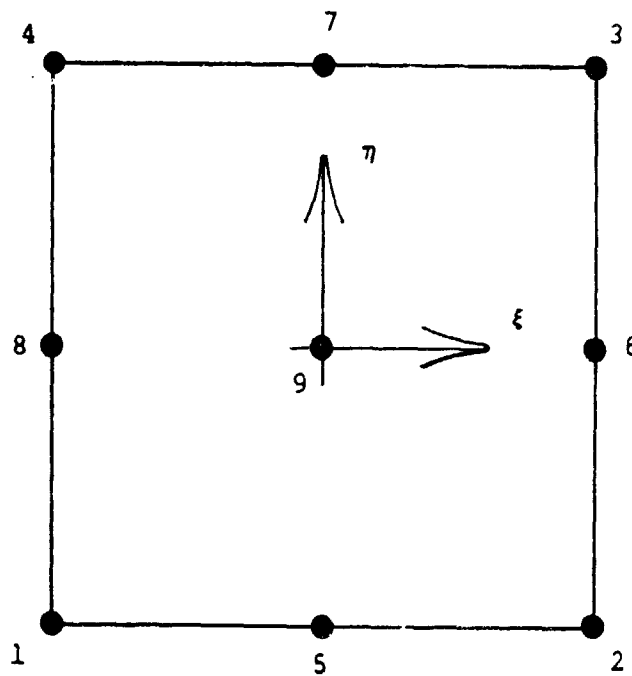


Figure 4.1 - Local Isoparametric Element

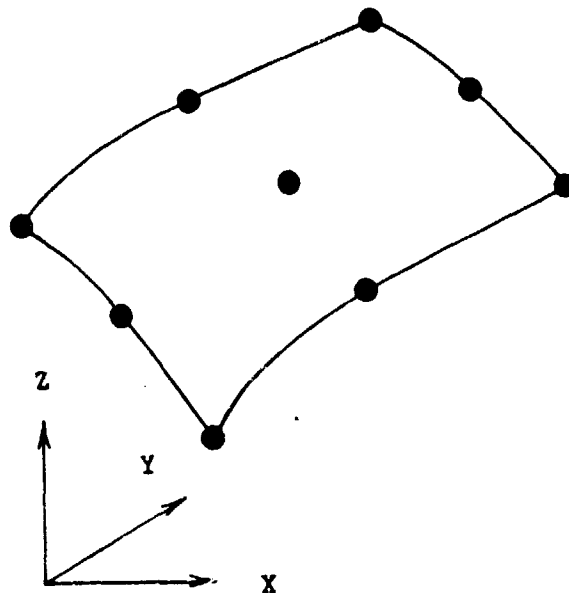


Figure 4.2 - Global Isoparametric Element

The important feature of the element is the shape functions. The shape functions are used to interpolate the variation of the variables within an element. For the isoparametric element, one set of functions describe the variation of both the element geometry and the solution variables. The element in figure 4.1 has a 3×3 nodal distribution in a two-dimensional space (i.e., the ξ and the η directions). Consequently, a quadratic variation can occur. The interpolation procedure for a general variable,

ϕ , is

$$\phi = \sum_{i=1}^9 N_i \phi_i \quad (4.1)$$

where i is an index which varies with the node number, N_i is the shape function for the i^{th} node and ϕ_i is the value of the variable at the i^{th} node. The Lagrangian shape functions for the quadratic, isoparametric element on the parent shape are [44]

$$N_1 = \frac{1}{4}(\xi^2 - \xi)(\eta^2 - \eta) \quad (4.2a)$$

$$N_2 = \frac{1}{4}(\xi^2 + \xi)(\eta^2 - \eta) \quad (4.2b)$$

$$N_3 = \frac{1}{4}(\xi^2 + \xi)(\eta^2 + \eta) \quad (4.2c)$$

$$N_4 = \frac{1}{4}(\xi^2 - \xi)(\eta^2 + \eta) \quad (4.2d)$$

$$N_5 = \frac{1}{2}(1 - \xi^2)(\eta^2 - \eta) \quad (4.2e)$$

$$N_6 = \frac{1}{2}(\xi^2 + \xi)(1 - \eta^2) \quad (4.2f)$$

$$N_7 = \frac{1}{2}(1 - \xi^2)(\eta^2 + \eta) \quad (4.2g)$$

$$N_8 = \frac{1}{2}(\xi^2 - \xi)(1 - \eta^2) \quad (4.2h)$$

$$N_9 = (1 - \xi^2)(1 - \eta^2). \quad (4.2i)$$

The Lagrangian shape function, N_i , is a continuous function having a value of unity at node i and a value of zero at node $j \neq i$. In the numerical implementation, unknown variable distributions will be replaced by an approximation with the form of equation 4.1. By this approximation, a finite number of parameters may then be solved.

4.2 Equation Discretization

Having defined the element, the next stage of numerical implementation is to discretize the integral equations. The discretization concept in boundary element methods is similar to that in finite element methods. The concept is that by subdividing the domain of the problem into smaller subdomains, or elements, the integrals for the complete domain may be approximated on a piecewise basis. Furthermore, by enforcing certain boundary conditions between the subdomains, an approximate solution over the entire problem domain may be determined.

The matrix equations are assembled by satisfying boundary conditions at an appropriate number of discrete points. The specific points used in this development are the nodes of the model. If the given boundary condition is a pressure boundary condition, the pressure at that point in terms of the boundary source distribution, σ , is, by equation 3.13,

$$p_1 = \int_B \sigma p^*(r) dB + \sum_{k=1}^K 4\pi\psi_k p_{k1}^* \quad (4.3)$$

where p_1 is the pressure at the 1^{th} boundary condition point and p_{k1}^* is the fundamental pressure solution from the k^{th} applied source to the 1^{th} boundary condition point. The unknown boundary source distribution, σ , on each element is approximated by

$$\sigma = \sum_{i=1}^9 \sigma_i N_i \quad (4.4)$$

utilizing equation 4.1. Furthermore, the boundary integral term will be evaluated on a piecewise basis (i.e., on an elemental basis). Hence, equation 4.3 can be rewritten as

$$p_1 = \sum_{n=1}^N \int_{B_n} \sum_{i=1}^M \sigma_i N_i p^*(r_1) dB_n + \sum_{k=1}^K 4\pi \Psi_k p_{k1}^* \quad (4.5)$$

where N is the number of boundary elements, M is the number of nodes per element, K is the number of applied sources, r_1 is the variable distance from the l^{th} boundary condition point to the n^{th} element and B_n represents the surface of the n^{th} element. Since the boundary source values, σ_i , are constants, the integral in equation 4.5 may be rewritten as

$$\begin{aligned} & \sum_{n=1}^N \int_{B_n} \left(\sum_{i=1}^M \sigma_i N_i \right) p^*(r_1) dB_n = \\ & \sum_{i=1}^M \sigma_i \sum_{n=1}^N \int_{B_n} N_i p^*(r_1) dB_n = \sum \sigma_i a_{i1} \end{aligned} \quad (4.6)$$

The numerical evaluation of the a_{i1} term will be discussed in sections 4.3 and 4.4. Finally, equation 4.3 can be more simplistically rewritten in approximate form as

$$p_1 = \sum \sigma_i a_{i1} + \sum_{k=1}^K 4\pi \Psi_k p_{k1}^* \quad (4.7)$$

A similar approach can be used for the velocity and impedance boundary conditions. With these two types of

boundary conditions, an additional term due to the singularity integration is present. To show the consequence of the 'free terms', the equation discretization for the velocity boundary condition will be presented. In equation 3.14, the velocity in terms of the boundary source distribution is given as

$$v_1 = 4\pi c_0 + \int_B \sigma v^*(r_1) dB + \sum_{k=1}^K 4\pi \Psi_k v_{kl}^* \quad (4.8)$$

Evaluating the integral on a piecewise basis yields

$$v_1 = 4\pi c_{il} \sigma_i + \sum_{n=1}^N \int_{B_n} \sum_{i=1}^M \sigma_i N_i v^*(r_1) dB_n + \sum_{k=1}^K 4\pi \Psi_k v_{kl}^* \quad (4.9)$$

where the variables maintain the same meanings as in equation 4.5. The 'free term', c_{il} , is zero when $i \neq 1$. When $i=1$, c_{il} is $-\frac{1}{2}$ for a point on a smooth boundary and $-\frac{\Omega}{4\pi}$ for a point on a corner where Ω is the solid interior angle at the corner. The constant source distributions can be factored out of the integral.

$$\begin{aligned} 4\pi c_{il} \sigma_i + \sum_{n=1}^N \int_{B_n} \left(\sum_{i=1}^M \sigma_i N_i \right) v^*(r_1) dB_n = \\ \sum_{i=1}^M \sigma_i \left(4\pi c_{il} + \sum_{n=1}^N \int_{B_n} N_i v^*(r_1) dB_n \right) = \\ \sum_{i=1}^M \sigma_i (4\pi c_{il} + a_{il}) \end{aligned} \quad (4.10)$$

The final approximation equation for a velocity boundary condition is

$$v_1 = \sum \sigma_i (4\pi c_{i1} + a_{i1}) + \sum_{k=1}^K 4\pi \Psi_k v_{k1}^* \quad (4.11)$$

Likewise, for impedance boundary conditions, the integral equation is

$$\int_{B_n} \sigma_i (p^*(r_1) - z_1 v^*(r_1)) dB_n - 4\pi z_1 c_{i1} \sigma_i + \sum_{k=1}^K 4\pi \Psi_k (p_{k1}^* - z_1 v_{k1}^*) = 0 \quad (4.12)$$

on a piecewise basis or

$$\sum \sigma_i (-4\pi z_1 c_{i1} + a_{i1}) + \sum_{k=1}^K 4\pi \Psi_k (p_{k1}^* - z_1 v_{k1}^*) = 0 \quad (4.13)$$

for the approximation equation.

For all boundary conditions, a general matrix equation can be written as

$$\left[A + A' \right] \left[\sigma \right] + \left[D \right] = \left[\alpha \right] \quad (4.14)$$

where either equation 4.7, 4.10 or 4.13 are used as each row of the matrix. The evaluation of the matrix terms for each boundary condition type are:

1. For Pressure Boundary Conditions

$$a_{i1} = \int_{B_n} N_i p^*(r_1) dB_n \quad (4.15a)$$

$$a'_{i1} = 0 \quad (4.15b)$$

$$d_k = \sum_{k=1}^K 4\pi \Psi_k p_{k1}^* \quad (4.15c)$$

$$\alpha_1 = p_1 \quad (4.15d)$$

2. For Velocity Boundary Conditions

$$a_{i1} = \int_{B_n} N_i v^*(r_1) dB_n \quad (4.16a)$$

$$a'_{i1} = 4\pi c_{i1} \quad (4.16b)$$

$$d_k = \sum_{k=1}^K 4\pi \Psi_k v_{k1}^* \quad (4.16c)$$

$$\alpha_1 = v_1 \quad (4.16d)$$

3. For Impedance Boundary Conditions

$$a_{i1} = \int_{B_n} (P^*(r_1) - z_1 v^*(r_1)) dB_n \quad (4.17a)$$

$$a'_{i1} = -4\pi z_i c_{i1} \quad (4.17b)$$

$$d_k = \sum_{k=1}^K 4\pi \Psi_k (P_{k1}^* - z_1 v_{k1}^*) \quad (4.17c)$$

$$\alpha_1 = 0 \quad (4.17d)$$

In the D matrix terms, the fundamental solutions are from the k^{th} applied source to the l^{th} node. The theory can be implemented into a computer format using equations 4.14 through 4.17.

4.3 Primary Numerical Integration Procedure

To numerically evaluate the integrals in equations 4.15a, 4.16a and 4.17a, a numerical integration procedure must be utilized. A numerical integration procedure using a Gauss-Legendre quadrature was selected. The numerical evaluation of the integral equations is performed on a

piecewise basis by mapping the integral in the global element coordinate system into the local element coordinate system. The domain of the local element is defined between the ξ and η coordinates of -1 and 1 . The limits are consistent with those of a Gauss-Legendre quadrature as the quadrature formula is [45]

$$\int_{-1}^1 g(\xi) d\xi = \sum_{i=1}^{NG} g(\xi_i) w_i \quad (4.18)$$

for a one-dimensional integration of a general function, $g(\xi)$. The values ξ_i and w_i are the integration point and weighting factor, respectively, and NG is the total number of integration points used in the integration. A boundary integration is essentially an area integration (when considering three-dimensional problems) which may be represented by

$$\int_{B_n} g(\xi, \eta) dB_n = \int_{-1}^1 \int_{-1}^1 g(\xi, \eta) d\xi d\eta \quad (4.19)$$

For a two-dimensional integration, the quadrature formula is [46]

$$\int_{B_n} g(\xi, \eta) dB_n = \sum_{m=1}^{NG_\xi} \left[\sum_{n=1}^{NG_\eta} g(\xi_n, \eta_m) w_n \right] w_m \quad (4.20)$$

Equation 4.20 was used to numerically evaluate the boundary integrals everywhere except where a singularity exists in the fundamental solutions as will be discussed in section 4.4.

The location of the integration points and the values of the weighting factors must be determined to finalize the local element integration procedure. A 4x4 Gaussian quadrature having coordinates

$$\xi_1 = \eta_1 = -0.861136311594053 \quad (4.21a)$$

$$\xi_2 = \eta_2 = -0.339981043584856 \quad (4.21b)$$

$$\xi_3 = \eta_3 = 0.339981043584856 \quad (4.21c)$$

$$\xi_4 = \eta_4 = 0.861136311594053 \quad (4.21d)$$

was selected. The mesh is shown in figure 4.3. The weighting factors corresponding to the integration points are

$$w_1 = 0.347854845137454 \quad (4.22a)$$

$$w_2 = 0.652145154862546 \quad (4.22b)$$

$$w_3 = 0.652145154862546 \quad (4.22c)$$

$$w_4 = 0.347854845137454. \quad (4.22d)$$

The abovementioned integration quadrature is exact for a seventh-order or lower polynomial, $g(\xi)$. The functions being integrated in the boundary integrals are the fundamental solutions, p^* and v^* times the shape functions, N_i , which are quadratic polynomials. The fundamental pressure solution is

$$p^*(\zeta, x) = -j\omega\rho \frac{e^{-jkx}}{r} \quad (4.23)$$

The series expansion of the fundamental solution is

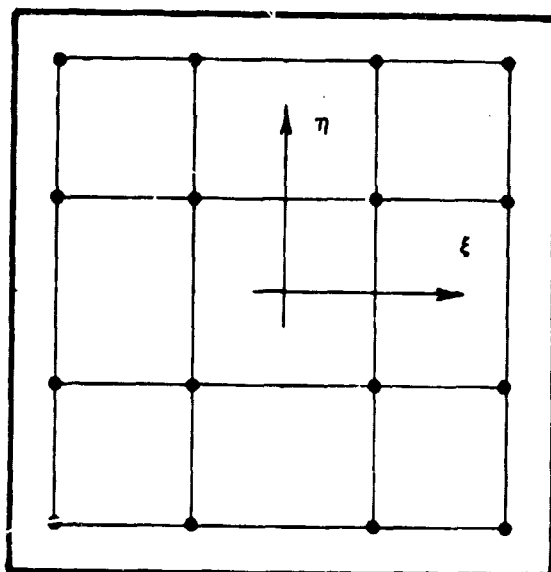


Figure 4.3 - Integration Point Mesh

$$\begin{aligned}
 p^*(\zeta, x) = & -j\omega\rho \left(\left(\frac{1}{x} - \frac{k^2 x}{2!} + \frac{k^4 x^3}{4!} - \frac{k^6 x^5}{6!} + \frac{k^8 x^7}{8!} \right) + \dots \right. \\
 & \left. -j \left(k - \frac{k^3 x^2}{3!} + \frac{k^5 x^4}{5!} - \frac{k^7 x^6}{7!} \right) + \dots \right) \quad (4.24)
 \end{aligned}$$

Hence, from equation 4.24, some of the limitations of this integration can be illustrated. The function will be accurately integrated only if the first few terms of the series approximation dominate. The $\frac{1}{x}$ term poses a problem

near a singularity point and will be addressed in the next section.

The preceding discussion applies equally as well for the fundamental velocity solution but will not be presented here.

The final point to be made for the integration procedures involves transformation from the global domain. Since the integration is for the global element, a transformation between the domains is necessary as follows [47].

$$\int G(x,y,z) dA = \int g(\xi,\eta) |J(\xi,\eta)| d\xi d\eta \quad (4.25)$$

In equation 4.25, the function $G(x,y,z)$ is a general function written in terms of the global element coordinates, x , y and z . The function $g(\xi,\eta)$ represents the transformation of $G(x,y,z)$ into the local coordinates, ξ and η . The quantity $|J(\xi,\eta)|$ is the determinant of the Jacobian matrix $J(\xi,\eta)$. For the application at hand, a three-dimensional global element is mapped into a two-dimensional local element. The determinant of the Jacobian for this transformation is [48]

$$|J(\xi,\eta)| = (a_1^2 + a_2^2 + a_3^2)^{\frac{1}{2}} \quad (4.26)$$

where

$$a_1 = \left(\frac{\partial y}{\partial \xi} \frac{\partial z}{\partial \eta} - \frac{\partial y}{\partial \eta} \frac{\partial z}{\partial \xi} \right) \quad (4.27a)$$

$$a_2 = \left(\frac{\partial z}{\partial \xi} \frac{\partial x}{\partial \eta} - \frac{\partial x}{\partial \xi} \frac{\partial z}{\partial \eta} \right) \quad (4.27b)$$

$$a_3 = \left(\frac{\partial x}{\partial \xi} \frac{\partial y}{\partial \eta} - \frac{\partial y}{\partial \xi} \frac{\partial x}{\partial \eta} \right) . \quad (4.27c)$$

The partial derivatives in equation 4.27 are determined with interpolations such as

$$\frac{\partial x}{\partial \xi} = \sum_{i=1}^9 x_i \frac{\partial \phi_i}{\partial \xi} , \quad (4.28)$$

as an example.

The procedure described above can be applied to any element which does not contain a singularity point. When the value of r in the fundamental solution approaches zero, special considerations are necessary for the integration. These considerations are explained in the following section.

4.4 Singularity Numerical Integration Procedure

A singularity occurs in the fundamental solutions whenever the particular boundary condition under consideration is located on a node of an element over which the boundary integral is being evaluated. The variable r in the fundamental solutions is the distance between the boundary condition point and the integration point. The primary Gaussian quadrature is unable to adequately evaluate the integrals whenever this singularity occurs. Hence, a new quadrature had to be developed to handle the singularity situation.

In some cases, the singularity can be removed from the integration domain. As detailed in the previous section, the integration domain is a quadrilateral region in a rectangular coordinate system. However, if the region were considered in polar coordinates, the differential area is

$$dA = r dr d\theta . \quad (4.29)$$

The radius appearing in equation 4.29 may be used to cancel the $\frac{1}{r}$ factor in the fundamental solution. Consider, for example, the fundamental pressure solution.

$$-j\omega\rho \int_{B_n} \frac{e^{-jkr}}{r} dB_n = -j\omega\rho \int_{B_n} e^{-jkr} dr d\theta \quad (4.30)$$

A similar result occurs for the fundamental velocity solution.

$$\int_{B_n} \hat{n} \cdot \nabla r \left(\frac{-1}{r} - jk \right) e^{-jkr} dr d\theta \quad (4.31)$$

In equation 4.31, it is apparent that a $\frac{1}{r}$ singularity still exists even after transforming to a polar coordinate system. However, the dot product of the vector normal to the surface and the gradient of the radius is zero for a flat plate element and tends to zero as the radius of curvature approaches infinity for curvilinear elements. For example, in figure 4.4, the fundamental solution is evaluated near the upper right corner. The $\hat{n} \cdot \nabla r$ will tend to zero. Thus, the integral in equation 4.31 is integrable

as a Cauchy principle value. (Hence, the 'free term' mentioned in chapter 3.)

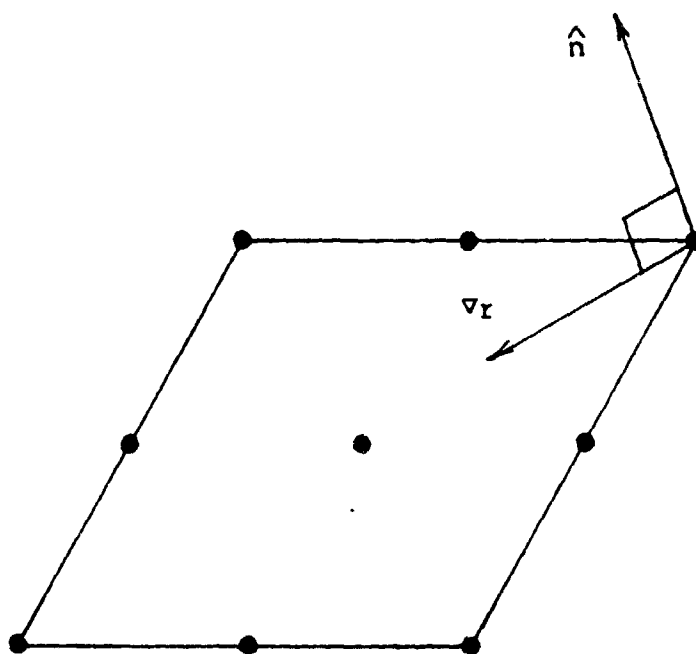


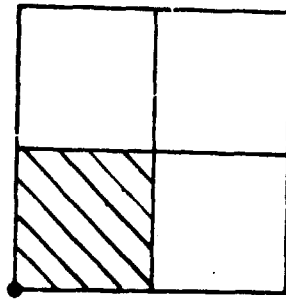
Figure 4.4 - Vectors For A Flat Element

There are three singularity integration cases which arise. Those cases are:

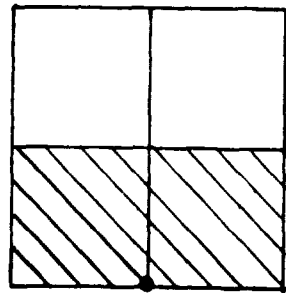
1. Boundary condition at a corner node
2. Boundary condition at a midside node

3. Boundary condition at the center node

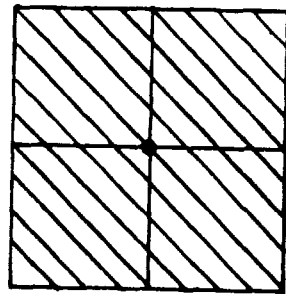
One polar domain transformation can be developed to accommodate all three cases. The transformation for a quadrant will apply for a corner node singularity. In addition, the remaining two cases can be considered as multiple quadrants and utilize the transformation for the corner node singularity. The transformation can be applied to both quadrants neighboring a midside node singularity and all four quadrants neighboring the center node singularity. Figure 4.5 shows the three cases. The shaded areas represent the quadrants transformed to a polar domain.



Corner node singularity



Midside node singularity



Center node singularity

Figure 4.5 - Singularity Cases

In general, a Gauss-Legendre quadrature similar to that explained in the previous section can be used for the polar domain. The difference lies in the integration variables, in this case r and θ .

The integration points in the polar coordinate system can be transformed from the rectangular coordinate system. The values of the ξ and η coordinates range from -1 to 1 . In the circular sector, the radial coordinate ranges from 0 to 1 and the angular coordinate from 0 to $\frac{\pi}{2}$. Mapping functions can be established which allow the polar coordinates to be obtained from the rectangular coordinates. These mapping functions are

$$r = \frac{1}{2}(\xi + 1) \quad (4.32a)$$

for the radial coordinate and

$$\theta = \frac{\pi}{4}(\eta + 1) \quad (4.32b)$$

for the angular coordinate. With equations 4.32, the polar integration points become a function of the rectangular integration points.

Determination of the polar weighting factors requires more work than for the determination of the polar integration points. Weighting factors are evaluated by the equation

$$w_i = \int_{\substack{a_{j=1} \\ j \neq i}}^b \prod_{n=1}^n \frac{(\xi - \xi_j)}{(\xi_i - \xi_j)} d\xi \quad (4.33)$$

for a Gauss-Legendre quadrature. To illustrate the determination of the polar weighting factors, consider a two point quadrature with points ξ_1 and ξ_2 in the rectangular system and points r_1 and r_2 in the polar system. The equation for the first weighting factor in the rectangular system is

$$w_{\xi_1} = \int_{-1}^1 \frac{\xi - \xi_2}{\xi_1 - \xi_2} d\xi. \quad (4.34)$$

For the first weighting factor in the polar system, the equation is

$$w_{r_1} = \int_0^1 \frac{r - r_2}{r_1 - r_2} dr. \quad (4.35)$$

Using equation 4.32 with equation 4.35, the weighting factor may be expressed as

$$w_{r_1} = \int_{-1}^1 \frac{\frac{1}{2}(\xi + 1) - \frac{1}{2}(\xi_2 + 1)}{\frac{1}{2}(\xi_1 + 1) - \frac{1}{2}(\xi_2 + 1)} \left(\frac{1}{2}d\xi\right) \quad (4.36)$$

or

$$w_{r_1} = \frac{1}{2} \int_{-1}^1 \frac{(\xi + 1) - (\xi_2 + 1)}{(\xi_1 + 1) - (\xi_2 + 1)} d\xi \quad (4.37)$$

or

$$w_{r_1} = \frac{1}{2} \int_{-1}^1 \frac{\xi - \xi_2}{\xi_1 - \xi_2} d\xi. \quad (4.38)$$

Equation 4.38 may now be written as

$$w_{r_1} = \frac{1}{2} w_{\xi_1} \quad (4.39)$$

by substituting in equation 4.34. The resulting

relationship is independent of the number of integration points but dependent solely on the multiplicative factor in the mapping functions (i.e., equations 4.32). Consequently, the weighting factors for the polar domain are

$$w_r = \frac{1}{2}w_\xi \quad (4.40a)$$

for the radial weighting factor and

$$w_\theta = \frac{\pi}{4}w_\eta \quad (4.40b)$$

for the angular weighting factor. The weighting factors and the integration points in the rectangular domain may be found in any reference containing Gaussian quadratures [49].

In the circular domain, a 4x16 mesh of integration points was selected; 4 radial coordinates and 16 angular coordinates. The integration points and weighting factors for the four point scheme are shown in equations 4.19 and 4.20. For the 16 point scheme, the integration points and weighting functions are

$$\eta_1 = -0.989400934991649 \quad (4.41a)$$

$$\eta_2 = -0.944575023073232 \quad (4.41b)$$

$$\eta_3 = -0.865631202387831 \quad (4.41c)$$

$$\eta_4 = -0.755404408355003 \quad (4.41d)$$

$$\eta_5 = -0.617876244402643 \quad (4.41e)$$

$$\eta_6 = -0.458016777657227 \quad (4.41f)$$

$$\eta_7 = -0.281603550779258 \quad (4.41g)$$

$\eta_8 = -0.095012509837637$ (4.41h)
 $\eta_9 = 0.095012509837637$ (4.41i)
 $\eta_{10} = 0.281603550779258$ (4.41j)
 $\eta_{11} = 0.458016777657227$ (4.41k)
 $\eta_{12} = 0.617876244402643$ (4.41l)
 $\eta_{13} = 0.755404408355003$ (4.41m)
 $\eta_{14} = 0.865631202387831$ (4.41n)
 $\eta_{15} = 0.944575023073232$ (4.41o)
 $\eta_{16} = 0.989400934991649$ (4.41p)

$w_1 = 0.027152459411754$ (4.42a)
 $w_2 = 0.062253523938647$ (4.42b)
 $w_3 = 0.095158511682492$ (4.42c)
 $w_4 = 0.124628971255533$ (4.42d)
 $w_5 = 0.149595988816576$ (4.42e)
 $w_6 = 0.169156519395002$ (4.42f)
 $w_7 = 0.182603415044923$ (4.42g)
 $w_8 = 0.189450610455068$ (4.42h)
 $w_9 = 0.189450610455068$ (4.42i)
 $w_{10} = 0.182603415044923$ (4.42j)
 $w_{11} = 0.169156519395002$ (4.42k)
 $w_{12} = 0.149595988816576$ (4.42l)
 $w_{13} = 0.124628971255533$ (4.42m)
 $w_{14} = 0.095158511682492$ (4.42n)
 $w_{15} = 0.062253523938647$ (4.42o)
 $w_{16} = 0.027152459411754$ (4.42p)

The mesh for the circular quadrant is illustrated in figure 4.6.

Examination of figure 4.6 reveals a gap between the circular domain and the original rectangular domain. As shown, the boundary integration for the circular domain would exclude that portion of the boundary outside the circular domain yet still within the original rectangular domain. This omission was corrected with a second domain transformation from the circular domain to a rectangular domain. The values of the ξ' and η' coordinates range from -1 to 0 since a quadrant of the element is being considered. Note that primes are used to differentiate the rectangular coordinates in the second transformed domain from the original rectangular coordinates. The mapping functions for the integration points are

$$\xi' = r - 1 \quad \text{for } \theta < \frac{\pi}{4} \quad (4.43a)$$

$$\xi' = r \cot \theta - 1 \quad \text{for } \theta > \frac{\pi}{4} \quad (4.43b)$$

and

$$\eta' = r \tan \theta - 1 \quad \text{for } \theta < \frac{\pi}{4} \quad (4.43c)$$

$$\eta' = r - 1 \quad \text{for } \theta > \frac{\pi}{4} \quad (4.43d)$$

For the weighting factors, the mapping functions are

$$w_{\xi'} = w_r \quad (4.44)$$

and

$$w_{\eta'} = \frac{w_\theta}{\cos \theta} \quad \text{for } \theta < \frac{\pi}{4} \quad (4.45a)$$

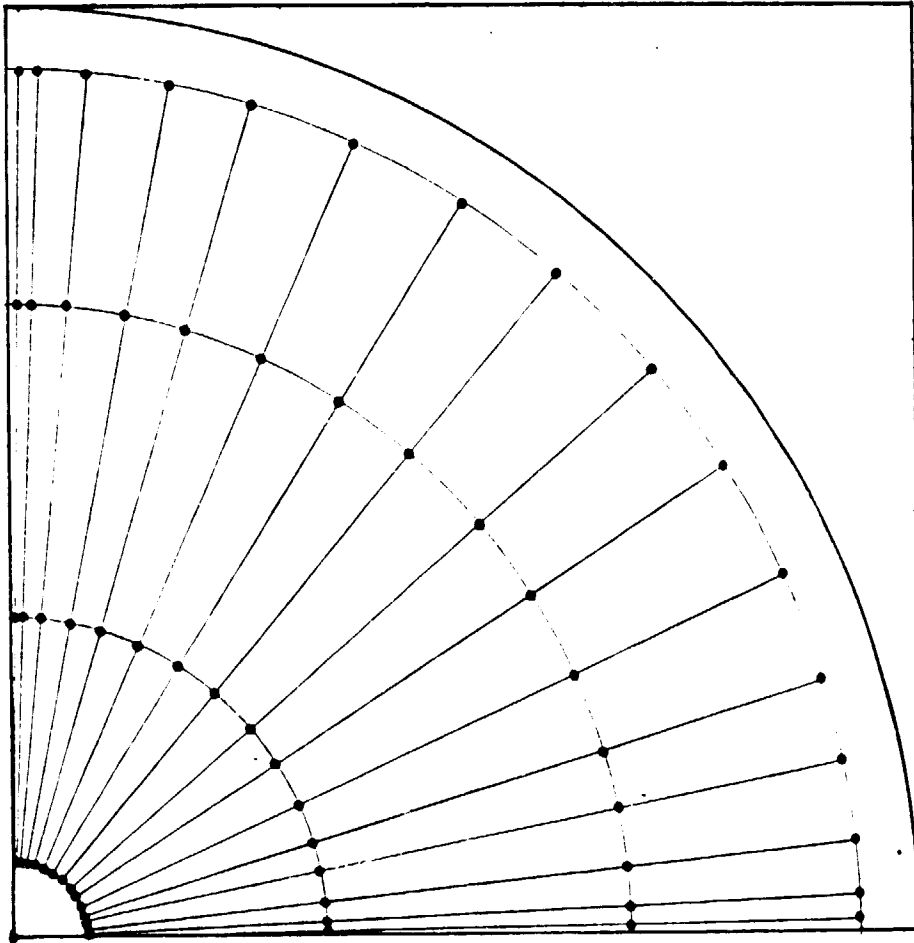


Figure 4.6 - Circular Domain Mesh

$$w_{\eta'} = \frac{w_{\theta}}{\sin \theta} \quad \text{for } \theta > \frac{\pi}{4} \quad (4.45b)$$

These mapping functions were determined in the same manner as the mapping functions for the first domain transformation (i.e., rectangular to polar). Figure 4.7 shows the mesh for the transformed circular domain.

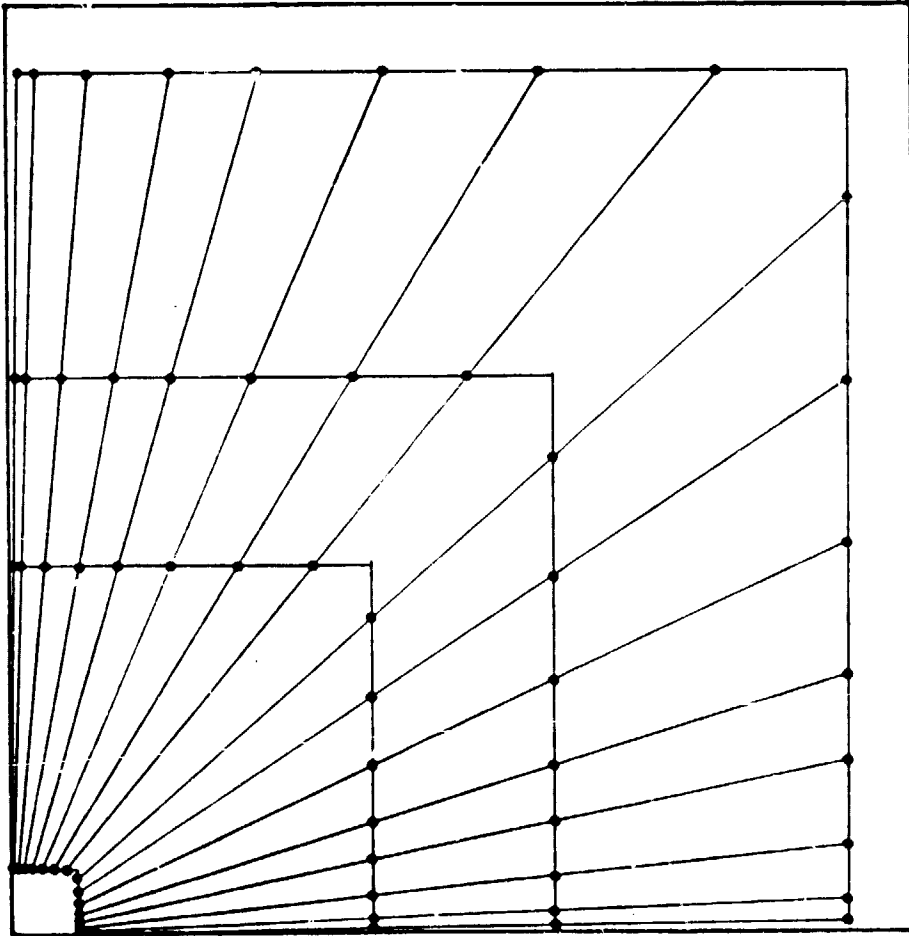


Figure 4.7 - Transformed Circular Domain Mesh

The final term required for the numerical integration is the determinant of the Jacobian. For a normal integration procedure, the determinant of the Jacobian is computed using equations 4.26 and 4.27. The determinant of the Jacobian can also be viewed as a ratio of the global area to that of the local area.

$$|J| = \frac{dx dy}{d\xi d\eta} \quad (4.46)$$

In polar coordinates, equation 4.46 is rewritten as

$$|J| = \frac{r_g dr_g d\theta_g}{r_l dr_l d\theta_l} \quad (4.47)$$

where the subscripts indicate the global and local domain variables. For the singularity integration, the integral is of the form

$$\int f(r_g, \theta_g) dr_g d\theta_g = \int F(r_l, \theta_l) |J|_r dr_l d\theta_l \quad (4.48)$$

where $|J|_r$ is the determinant of the Jacobian required for the singularity integration procedure. From equation 4.48, the required determinant of the Jacobian will be

$$|J|_r = \frac{dr_g d\theta_g}{dr_l d\theta_l} \quad (4.49)$$

and can be calculated from the normal determinant of the Jacobian by

$$|J|_r = \frac{r_l}{r_g} |J| \quad (4.50)$$

If the mapping between the global and local domains is simply a scaling of the same angular dimension sector, the

mapping equations can be written as

$$r_g = ar_1 \quad (4.51a)$$

for the radial component and

$$\theta_g = \theta_1 \quad (4.51b)$$

for the angular coordinate since it is assumed that the element is only varying in size and not in shape. Thus, the differentials are expressed as

$$dr_g = adr_1 \quad (4.52a)$$

and

$$d\theta_g = d\theta_1 \quad (4.52b)$$

For this case, the normal determinant of the Jacobian is

$$|J| = \frac{r_g dr_g d\theta_g}{r_1 dr_1 d\theta_1} = \frac{(ar_1)(adr_1)d\theta_1}{r_1 dr_1 d\theta_1} = a^2 \quad (4.53)$$

and the required determinant of the Jacobian is

$$|J|_r = \frac{dr_g d\theta_g}{dr_1 d\theta_1} = \frac{(adr_1)d\theta_1}{dr_1 d\theta_1} = a \quad (4.54)$$

Therefore, the required determinant of the Jacobian may be calculated from the normal determinant by

$$|J|_r = \sqrt{|J|} \quad (4.55)$$

The relationship in equation 4.55 is an approximation if the shape of the global element is distorted from that of the local element. Nevertheless, this relationship is utilized for the singularity integration. Hence, the quadrature formula becomes

$$\int f(x,y) dx dy = \int F(r_1, \theta_1) \sqrt{|J|} dr_1 d\theta_1 . \quad (4.56)$$

The numerical integration procedures detailed above can be utilized to evaluate the discretized integral equations to establish the system matrices for a boundary element model. Although this numerical integration procedure is successful, it is not the only possible procedure to apply. An alternative integration procedure has been suggested by Zimmerle and Bernhard [50] but was not attempted in this research.

4.5 Solution Procedure

Equation 4.14 is used to solve for the assumed source densities once the numerical procedures described above have been used to evaluate and assemble the system matrices. To solve for the source densities, a full matrix, complex equation solver is required. The matrix equation is neither banded nor symmetric so a robust equation solver is required. The subroutine used, the IMSL subroutine LEQTLIC, is a linear equation solver for equations having complex quantities. It uses a full matrix storage mode. This storage mode is required since the matrices for boundary element methods, unlike finite element methods, are fully populated matrices. The IMSL subroutines are readily accessible as a commercial code which was the primary reason for the application in this

research. It is possible that a more efficient equation solving routine is available or may be generated for use in solving the boundary integral equations.

The goal for this research was to predict the sound fields in acoustical cavities. To accomplish this, the source densities, after quantization, were used to solve for the acoustic pressures at field points interior to the cavity domain. Equations 4.14 and 4.15 were again utilized. The unknown variables, the pressures at the field points, can now be solved utilizing the source density distribution found earlier. The only major difference in the formulation is that the distance r in the fundamental pressure solution is the distance from the source density to the field point at which the pressure is desired. Using this procedure, the pressures at the interior field points may be evaluated.

The procedures required for numerical implementation of the boundary integral equations have been discussed. To illustrate the techniques, a number of examples were considered. The numerical results of these examples are presented in the following chapter.

CHAPTER 5

CASE STUDIES

A number of case studies were undertaken to illustrate the theory and numerical implementation discussed in chapters 3 and 4. Two models were considered in these studies: a spherical cavity model and a rectangular cavity model. This chapter presents the numerical and, where available, the analytical results of the case studies.

5.1 Spherical Cavity Model

A spherical cavity was chosen as the first case study for a number of reasons. A sphere with a velocity distribution which is uniform with respect to angle can be treated as a one-dimensional problem as will be demonstrated in the derivation of the analytical solution. Consequently, the analytical solution for the spherical cavity can be easily determined. Another advantage for the sphere is the absence of corners and edges. Corners and

create difficulties with boundary element methods as
 be shown for the rectangular cavity.

The analytical solution for the spherical cavity is
 deduced from the wave equation for spherically symmetric
 pressure fields [51].

$$\frac{\partial^2 p}{\partial r^2} + \frac{2}{r} \frac{\partial p}{\partial r} = \frac{1}{c^2} \frac{\partial^2 p}{\partial t^2} \quad (5.1)$$

Using the time dependence from equation 5.1 yields the
 time-independent wave equation

$$\frac{\partial^2 p}{\partial r^2} + \frac{2}{r} \frac{\partial p}{\partial r} + k^2 p = 0 \quad (5.2)$$

Equation (5.2) represents the time-independent wave equation in a
 spherically symmetric geometry without applied sources.
 Equation (5.2) is a special case of the spherical Bessel's
 equation

$$r^2 \frac{\partial^2 p}{\partial r^2} + 2r \frac{\partial p}{\partial r} + k^2 (r^2 - n^2) p = 0 \quad (5.3)$$

Equation (5.3) is solved by r^2 and with $n=0$. Thus, the solution to equation
 (5.2) will involve spherical Bessel functions and will be of
 the form

$$p(r) = \bar{A} j_0(kr) + \bar{B} y_0(kr) \quad (5.4)$$

where the constants \bar{A} and \bar{B} are determined by the boundary
 conditions. Alternatively, a second general solution to
 spherical Bessel's equation of equal validity is

$$p(r) = a \frac{e^{-jkr}}{r} + b \frac{e^{jkr}}{r} \quad (5.5)$$

where \bar{a} and \bar{b} are determined by the boundary conditions.

For the first verification of the numerical code, the specific solution of

$$p(r) = 100j_0(kr) \quad (5.6)$$

was selected. The spherical model has a radius of $\frac{1}{2}$ meters. Also, an arbitrary wave number of 8 was selected. This corresponds to a frequency of 437 Hz in air with a speed of sound of 343 meters/second. Figure 5.1 shows the analytical solution of the pressure distribution within the the cavity. The sphere center corresponds to a radial position of zero while the sphere boundary corresponds to a radial position of $\frac{1}{2}$.

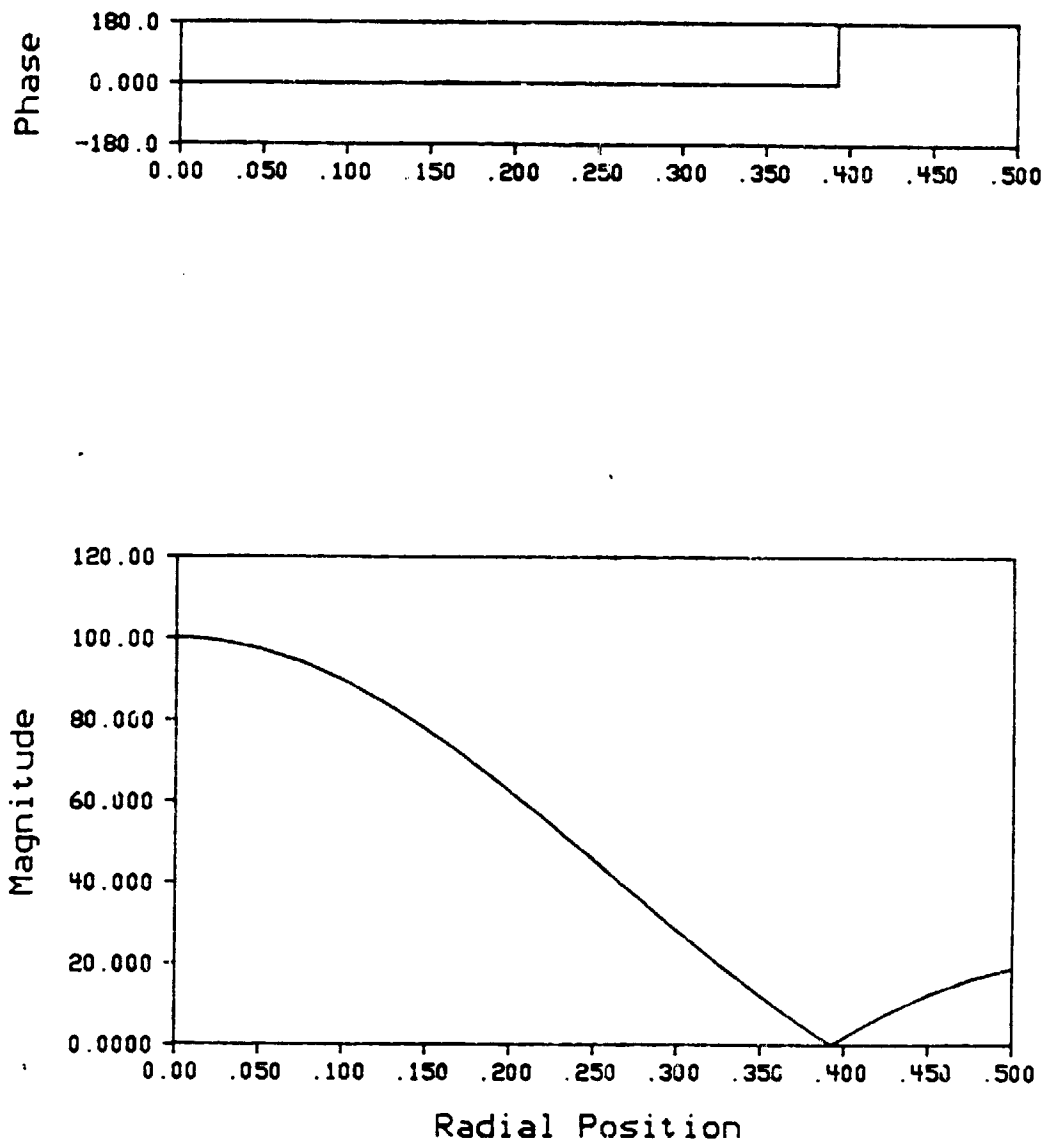


Figure 5.1 - Analytical Spherical Pressure Distribution
For $k=8$

Appropriate boundary conditions of various types were derived to verify the solution in the cavity interior. The solution of equation 5.6 at the boundary is $p(\frac{1}{2}) = -18.92$ with the selected wave number. For the first example, this pressure was applied at the outer boundary of the sphere. The numerical results are shown with the analytical results in figure 5.2. The numerical solution is represented by the solid line marked with Y's at the discrete solution points. The dashed line represents the analytical solution.

A sphere with uniform velocity boundary conditions was the second numerical example. The velocity boundary conditions were determined by

$$\bar{v} = (1 - \frac{j}{kr}) \frac{P}{\rho c} \hat{r} \quad (5.7)$$

which relates the velocity of a spherical wave to the pressure [51]. For the numerical example, the velocity boundary condition was $\bar{v} = -0.0456 + j0.0114$. Figure 5.3 shows the numerical and analytical results.

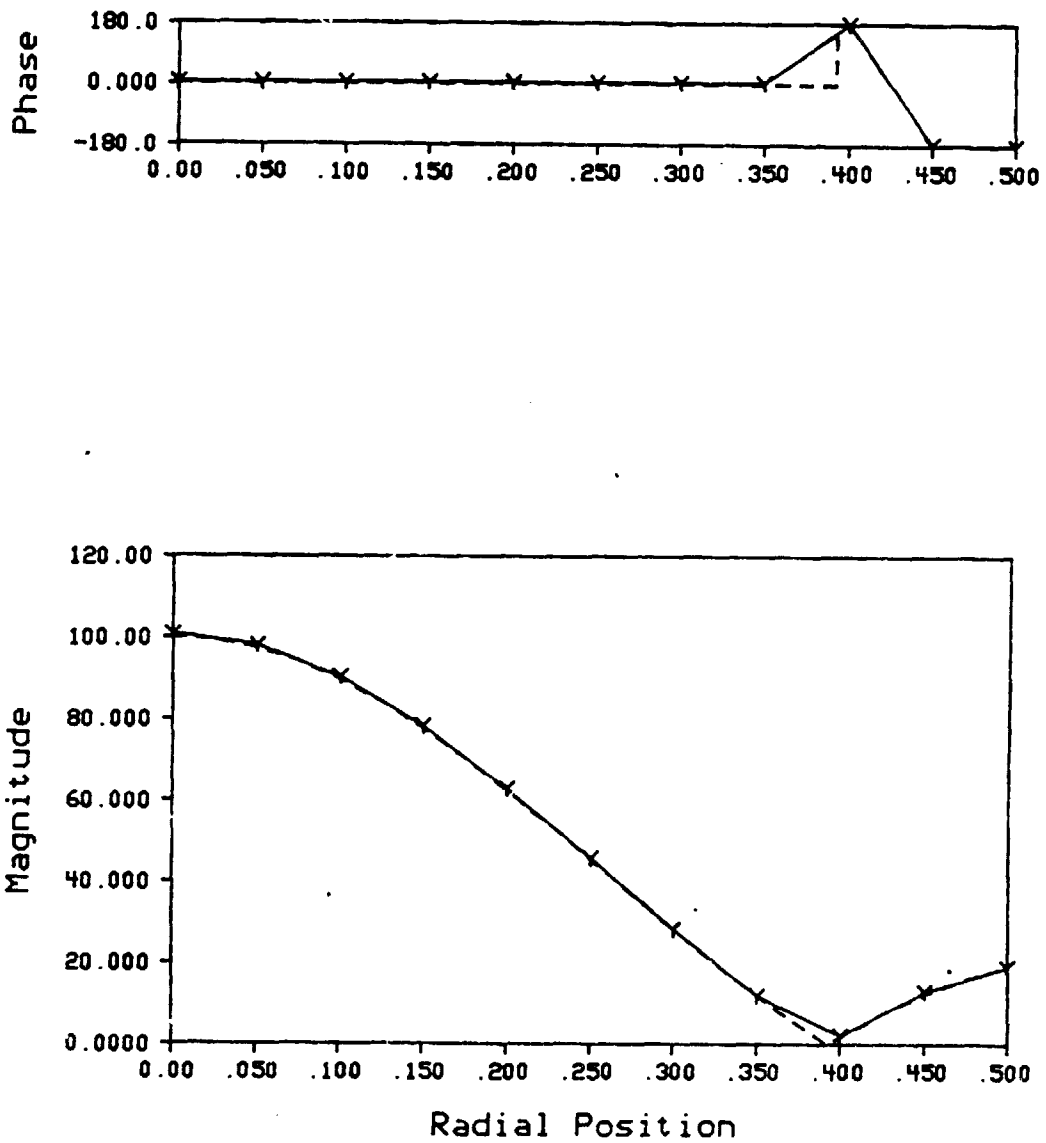


Figure 5.2 - Spherical Pressure Distribution For Pressure Boundary Conditions At $k=8$

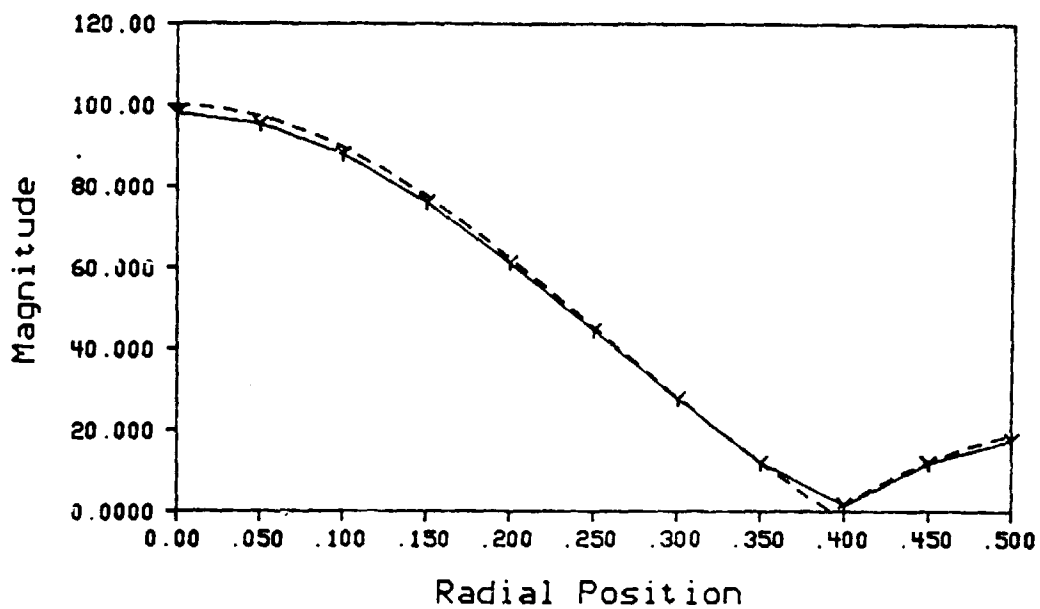
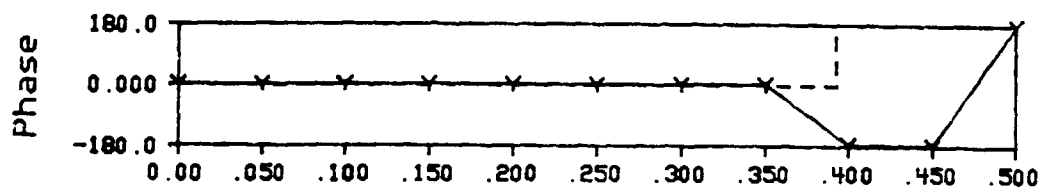


Figure 5.3 - Spherical Pressure Distribution For Velocity Boundary Conditions At $k=8$

The analytical and the numerical results in both figures 5.2 and 5.3 are in excellent agreement. In fact, the correlation is so good for figure 5.2 that the two results are nearly coincident. One note must be made regarding the phase plot. When examining the phase, it must be understood that a phase of 180° is equivalent to a phase of -180° . Hence, the apparent jumps in phase in the region from $r = 0.4$ to $r = 0.5$ do not actually represent phase differences as it may appear at first glance. For the velocity boundary condition model represented in figure 5.3, a slight amount of difference can be detected between the analytical and numerical solutions. This slight error is due to the interpolation of the radial distances between the boundary condition points and the integration points. As previously noted, the shape functions are quadratic functions. However, the radial distance is determined by

$$r = \sqrt{(x_2 - x_1)^2 + (y_2 - y_1)^2 + (z_2 - z_1)^2} \quad (5.8)$$

which is not a purely quadratic function due to the radical involved in its determination. Consequently, some interpolation error can be expected and, in fact, is evident. The interpolation error is more prevalent when the velocity boundary conditions are used because of the $\frac{1}{r^2}$ term in the fundamental velocity solution as opposed to

the $\frac{1}{r}$ term in the fundamental pressure solution. Regardless, for cases where derived boundary conditions are specified, the prediction of the solution in the domain is very good.

The next case study was that of a pulsating spherical cavity. The analytical solution for this problem can be represented by equation 5.5 where the boundary conditions for this problem are

$$\frac{\partial p}{\partial r} = 0 \quad (5.9a)$$

at the center of the sphere and

$$\frac{\partial p}{\partial r} = -j\omega\rho V(r_0) \quad (5.9b)$$

at the surface of the sphere. Boundary condition 5.9a represents the condition that the pressure is finite at the sphere center. Equation 5.9b is derived from Euler's equation. Using equation 5.5 with the boundary conditions of equations 5.9, the analytical solution for the pressure is

$$p(r) = j \frac{\rho c k r_0^2 V(r_0)}{(\sin(kr_0) - kr_0 \cos(kr_0))} \frac{\sin(kr)}{r} \quad (5.10)$$

For the model in question, the radius at the sphere surface is $r_0 = \frac{1}{2}$.

Resonant frequencies can be determined for the spherical cavity using equation 5.10. Resonance occurs whenever the impedance $\frac{p}{v}$ becomes infinite. From equation 5.10,

resonance for the spherical cavity occurs whenever

$$\sin(kr_0) - kr_0 \cos(kr_0) = 0 . \quad (5.11)$$

The transcendental equation for the natural frequencies is

$$\tan(kr_0) = kr_0 \quad (5.12)$$

for the spherical cavity. Thus, the first three natural frequencies occur at $kr_0 = 0$, $kr_0 = 4.493$ and $kr_0 = 7.725$.

The analytical solution of equation 5.10 at $r = r_0$ is shown in figure 5.4 as a function of the frequency. The natural frequencies are evident in figure 5.4 as peaks in the pressure magnitude. In addition, figure 5.4 shows zero pressures and 180° phase shifts occurring at $kr_0 = \pi$ and $kr_0 = 2\pi$. The zero pressures are expected since $p = 0$ whenever $\sin(kr_0) = 0$ in equation 5.10. The velocity at the boundary of the sphere was chosen to be 1 to generate the analytical solution in figure 5.4.

To numerically evaluate the response of the spherical cavity, a sweep of frequencies from 0 to 873 Hz was used to generate results comparable to those in figure 5.4. The frequency range corresponds to kr_0 values from 0 to 8. A uniform velocity boundary condition of 1 was applied to the spherical cavity model. Both the analytical and numerical results are shown in figure 5.5. The solid line marked with Y's represents the numerical results and the dashed line is the analytical solution.

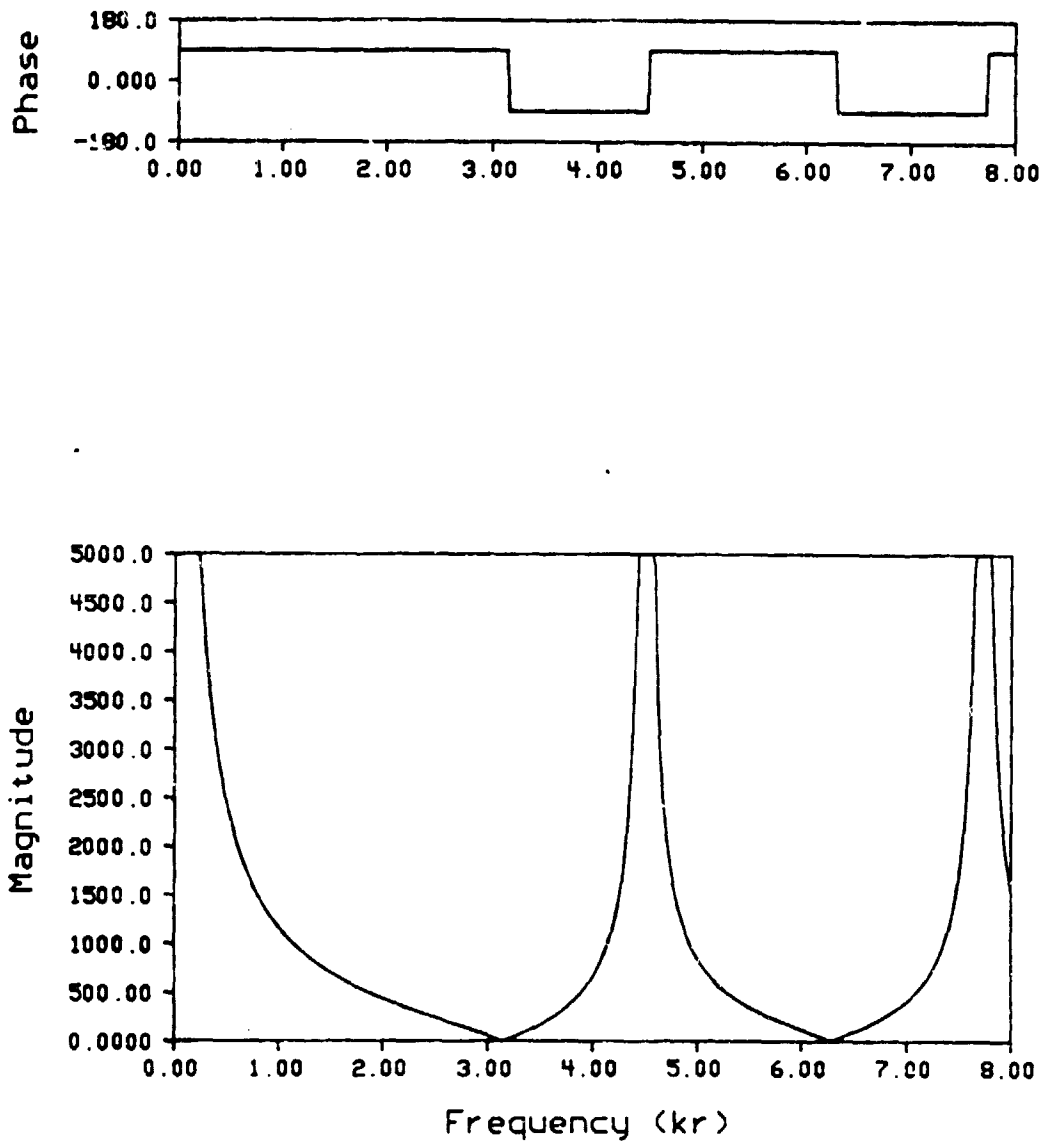


Figure 5.4 - Analytical Response For The Pressure At The Wall Of A Pulsating Spherical Cavity

Figure 5.5 shows excellent correlation between analytical and numerical results throughout the frequency range studied except in the very low frequency regime. The numerical results from $kr = 0.25$ to $kr = 0$ tend to approach zero whereas the analytical results tend to approach infinity within that same region. A definitive reason for this phenomenon has not been clearly identified. However, work published by other researchers may be drawn upon to formulate possible explanations. Researchers such as Copley [17] and Burton and Miller [18] have presented evidence that the coincidence of frequencies with interior eigenfrequencies cause boundary element formulations to fail for acoustic radiation problems. For the indirect boundary element methods, the difficulty stems from a nonexistence of surface source distributions at those eigenfrequencies as shown by Copley [17]. As was mentioned in chapter 2, overdetermination procedures were utilized by Shenck [19] and Piszczyk and Klosner [20] in direct boundary element methods to overcome the interior eigenfrequency difficulties. Although it is possible, but not proven, that an overdetermination procedure may resolve the low frequency discrepancies shown in figure 5.5, an approach of this type was not used in the current research. The primary reason is that the phenomenon occurs in a very low frequency regime which is not of interest in most problems.

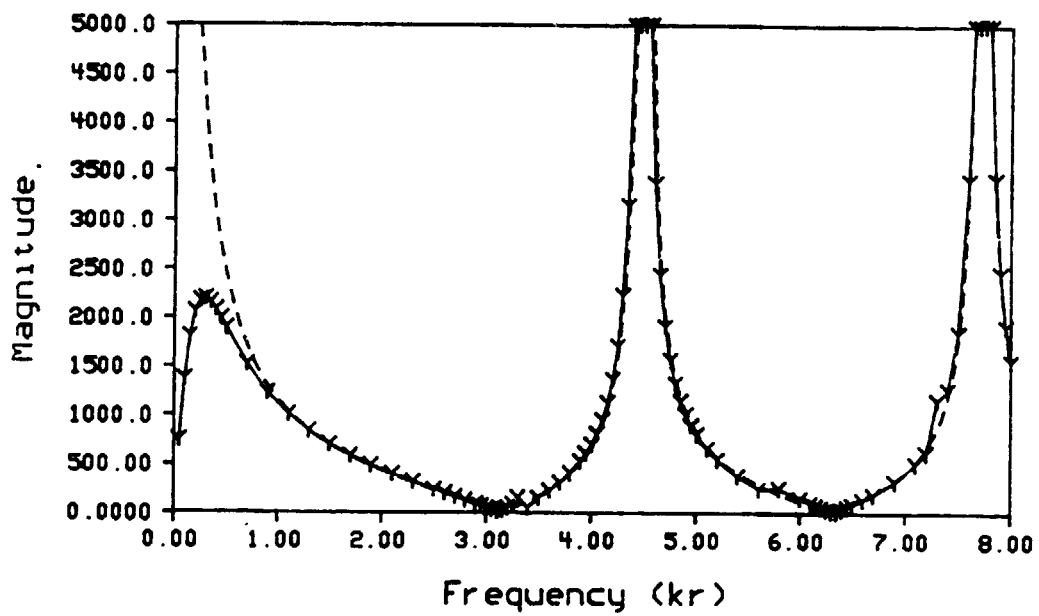
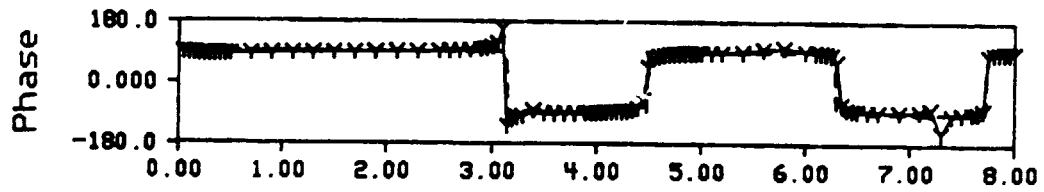


Figure 5.5 - Numerical And Analytical Response For The Pressure At The Wall Of A Pulsating Spherical Cavity

C-2

To further investigate the spherical cavity response, pressure distributions within the cavity were numerically determined at three frequencies. The three frequencies are $kr_0 = 2, 5.4$ and 7.1 corresponding to 1372, 3704 and 4871 Hz, respectively if $r_0 = \frac{1}{2}$ meters and $c = 343$ m/s. The spherical cavity pressure distributions for each of these frequencies are shown in figures 5.6, 5.7 and 5.8. All three distributions exhibit the expected spherical Bessel's function-type behavior. The particular frequencies were selected to show the behaviors occurring before and after the zero pressure frequencies, i.e., $kr = \pi$ and 2π . The analytical solutions shown in these figures are from equation 5.10. As in figures 5.2 and 5.3, excellent correlation is shown in figures 5.6 through 5.8.

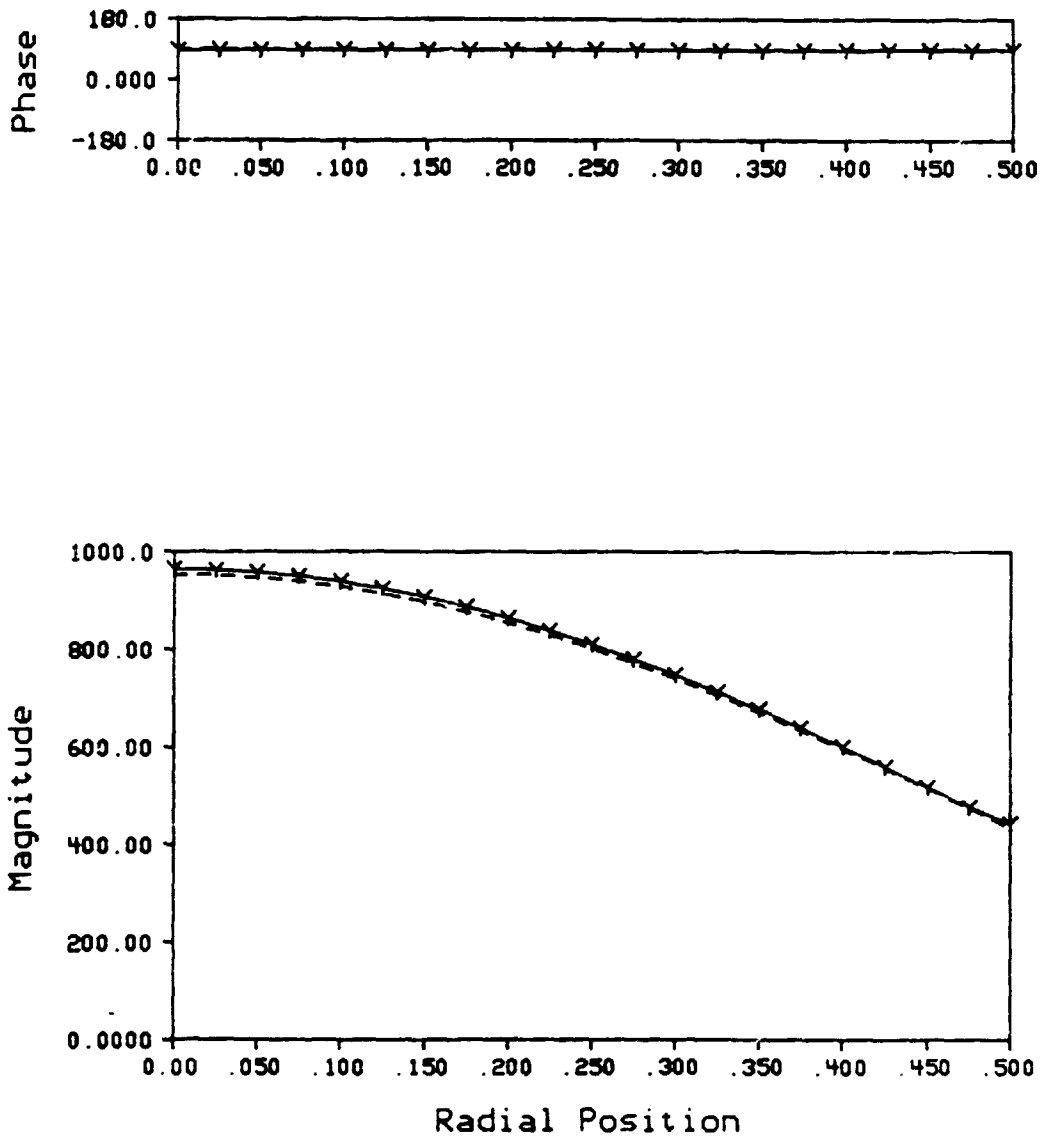


Figure 5.6 - Spherical Cavity Pressure Distribution For Velocity Boundary Conditions At $kr=2$

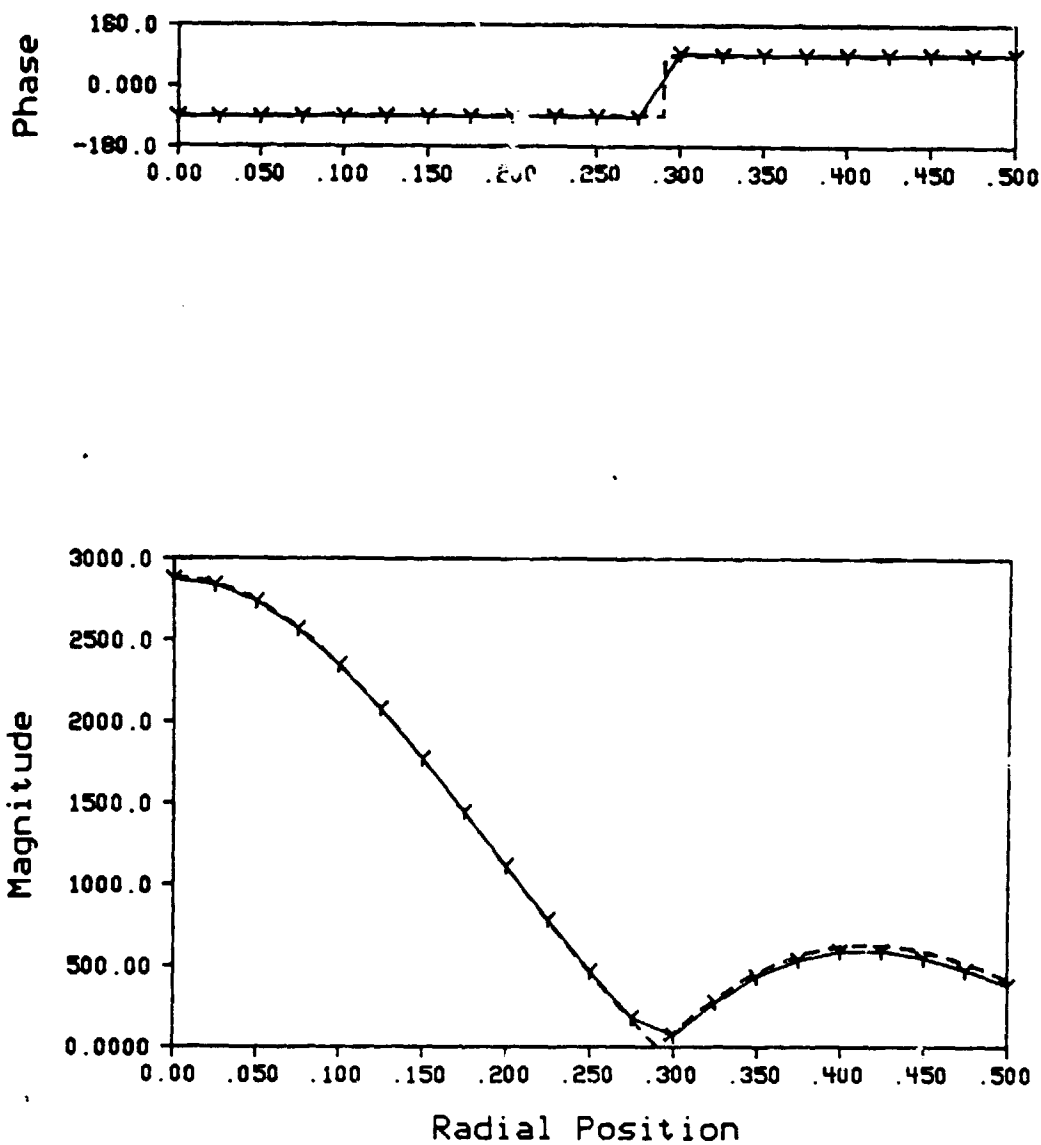


Figure 5.7 - Spherical Cavity Pressure Distribution For Velocity Boundary Conditions At $kr=5.4$

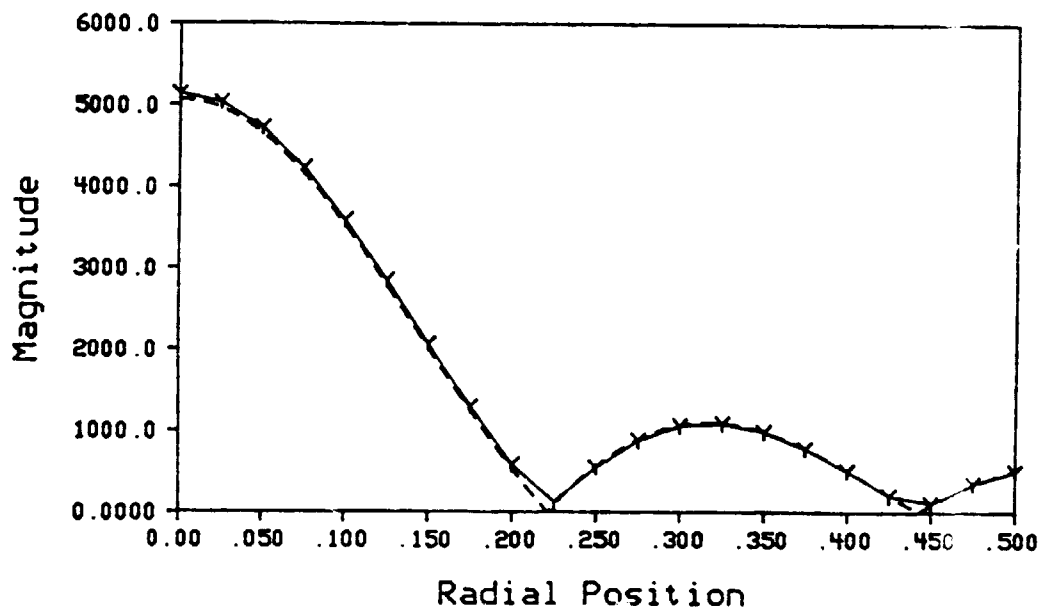
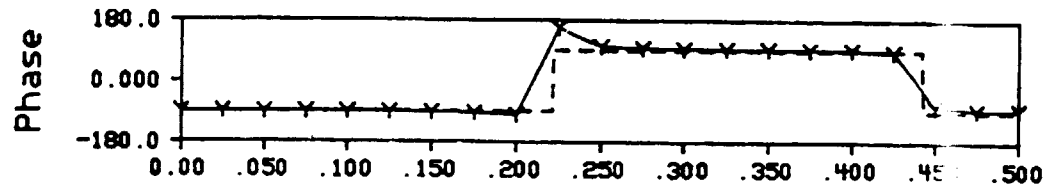


Figure 5.8 - Spherical Cavity Pressure Distribution For Velocity Boundary Conditions At $kr=7.1$

Although the results presented thus far have only been for pressure and velocity boundary conditions, impedance boundary conditions have also been implemented. Models having only impedance boundary conditions must contain an applied source within the cavity. Otherwise, the α vector in equation 4.14 is a zero vector (see equation 4.17d) and the resulting source distribution is trivial. In other words, there is no excitation of any sort in the problem. To verify the impedance boundary condition implementation, a spherical cavity with purely impedance boundary conditions and an applied source of strength 1 located at the sphere center was utilized. The impedance boundary conditions were established such that they would simulate the impedance experienced by a point source radiating into an infinite free space. The impedance relationship can be derived from equation 5.6 as

$$z = \frac{p}{v} = \frac{\rho c}{\left(1 - \frac{j}{kr}\right)} \quad (5.13)$$

With a wave number of $k = 0.583$ (200 Hz) and $r = \frac{1}{2}$ at the boundary, the resulting impedance is $z = 32.5 + j111.5$. Figure 5.9 is the pressure distribution obtained numerically for the described model.

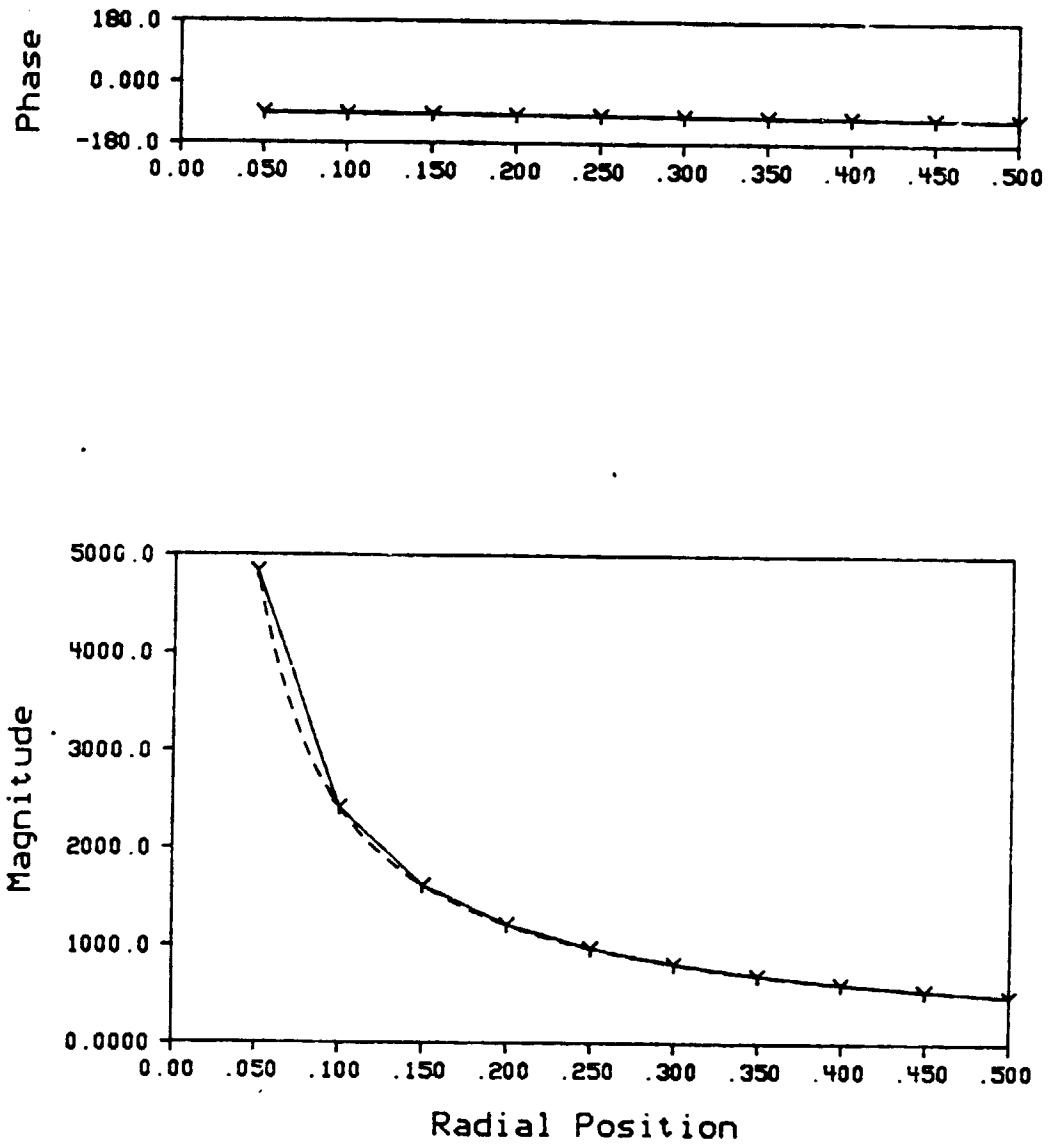


Figure 5.9 - Pressure Distribution For A Sphere With Radiation Impedance Boundary Conditions At $k=0.583$

For comparative purposes, similar distributions for models with pressure and velocity boundary conditions were obtained. The pressure solution and, consequently, the boundary conditions may be determined in a number of ways. In this case, the pressure boundary conditions were determined from equation 3.13 and 3.15.

$$\bar{p}(\mathbf{x}) = \int_B \sigma(\zeta) \bar{p}^*(\zeta, \mathbf{x}) + \sum_{i=1}^1 4\pi\psi_i \bar{p}^*(\mathbf{x}_{s_i}, \mathbf{x}) \quad (5.14)$$

The pressure at any point is due entirely to the applied source if the boundary simulates an infinite domain problem. Hence, the source density distribution is zero at the model boundary (i.e., $\sigma(\zeta) = 0$). Equation 5.14 becomes

$$p(r) = -j\omega\rho 4\pi\psi_1 \frac{e^{-jkr}}{r} \quad (5.15)$$

after the fundamental pressure solution is inserted. With an applied source strength of 1, the equation to determine the pressure boundary condition is

$$p(r) = -j\omega\rho 4\pi \frac{e^{-jkr}}{r} . \quad (5.16)$$

For the model with $k = 0.583$ and $r = \frac{1}{2}$ at the boundary, the pressure boundary condition is $p = -139.07 - j463.51$. The numerical results obtained are shown in figure 5.10. Equivalent velocity boundary conditions found using equation 5.6 are $v = -4.167 + j0.033$. Figure 5.11 shows the pressure distribution numerically obtained using velocity boundary conditions.

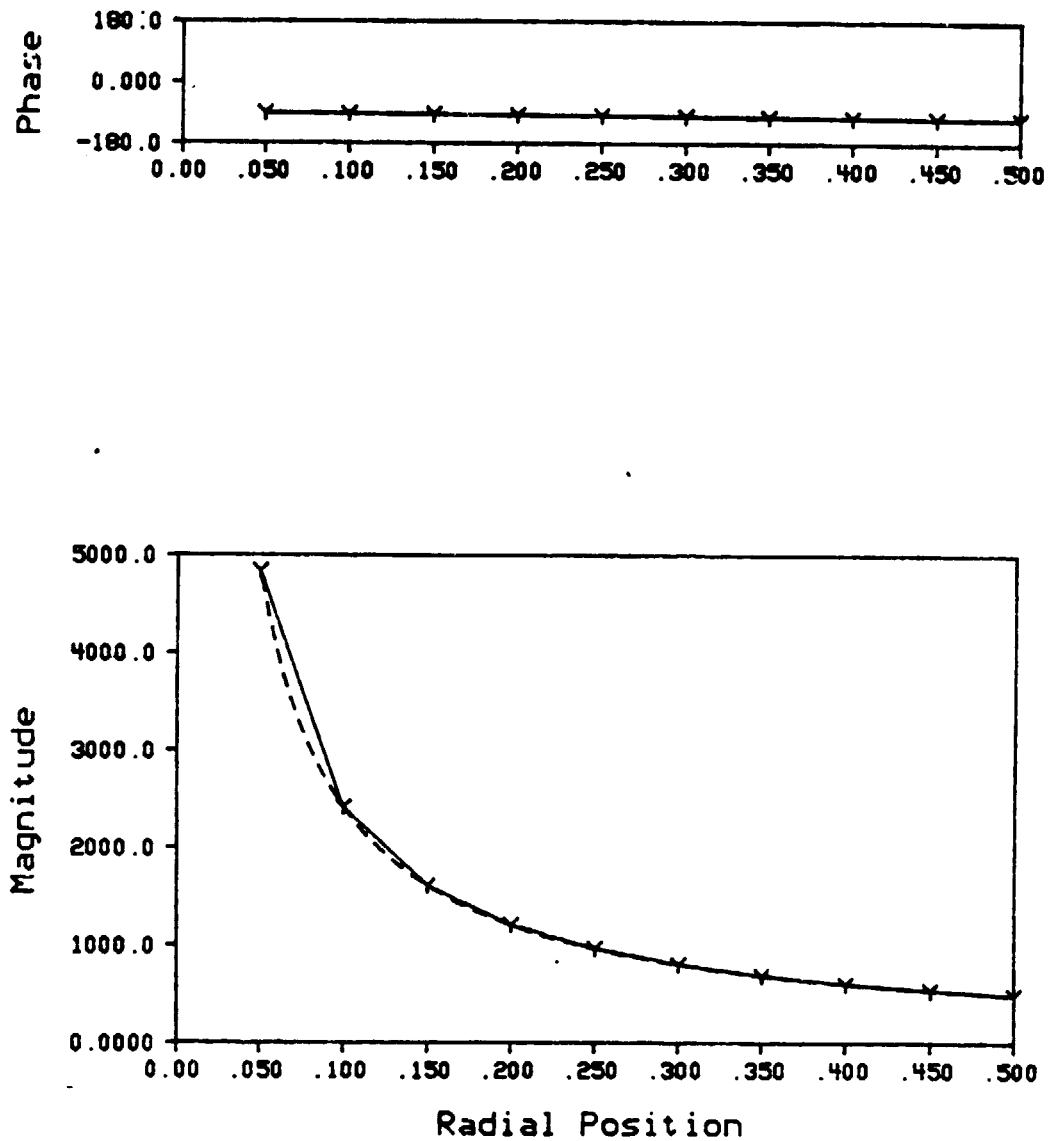


Figure 5.10 - Pressure Distribution For A Sphere With Radiation Pressure Boundary Conditions At $k=0.583$

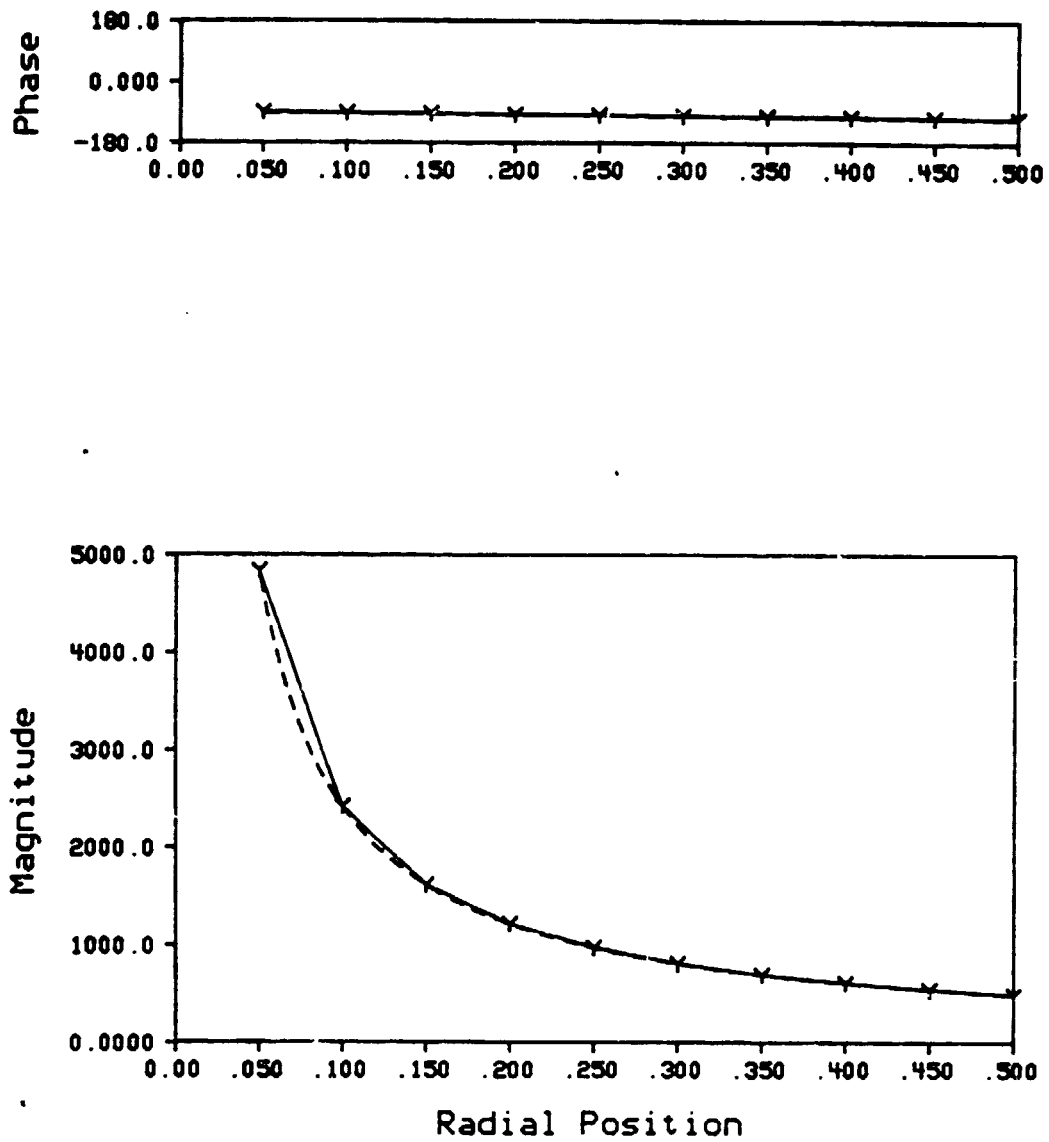


Figure 5.11 - Pressure Distribution For A Sphere With Radiation Velocity Boundary Conditions At $k=0.583$

To evaluate the validity of the impedance boundary condition capability of the program, figure 5.9 may be compared with figures 5.10 and 5.11. Both pressure and velocity boundary conditions have previously been shown to produce excellent results in the spherical cavity model. Figures 5.9, 5.10 and 5.11 are identical pressure distributions. Regardless of the type of boundary condition being applied, the numerical results for this model are unchanged.

The final study using the spherical cavity was to numerically generate a forced response prediction for the case of a point source in a rigid-walled cavity. Velocity boundary conditions of zero were applied to the sphere. A source having a strength of 1 was placed at the center of the cavity to excite the model. The swept frequency band ranged from 0 to 873 Hz (or kr from 0 to 8) as was the case for the previous response in figure 5.5. The response for the rigid-walled spherical cavity is shown in figure 5.12. In addition, a pressure distribution within the cavity for a frequency of 3087 Hz ($kr = 4.5$), near the first resonant frequency, is shown in figure 5.13.

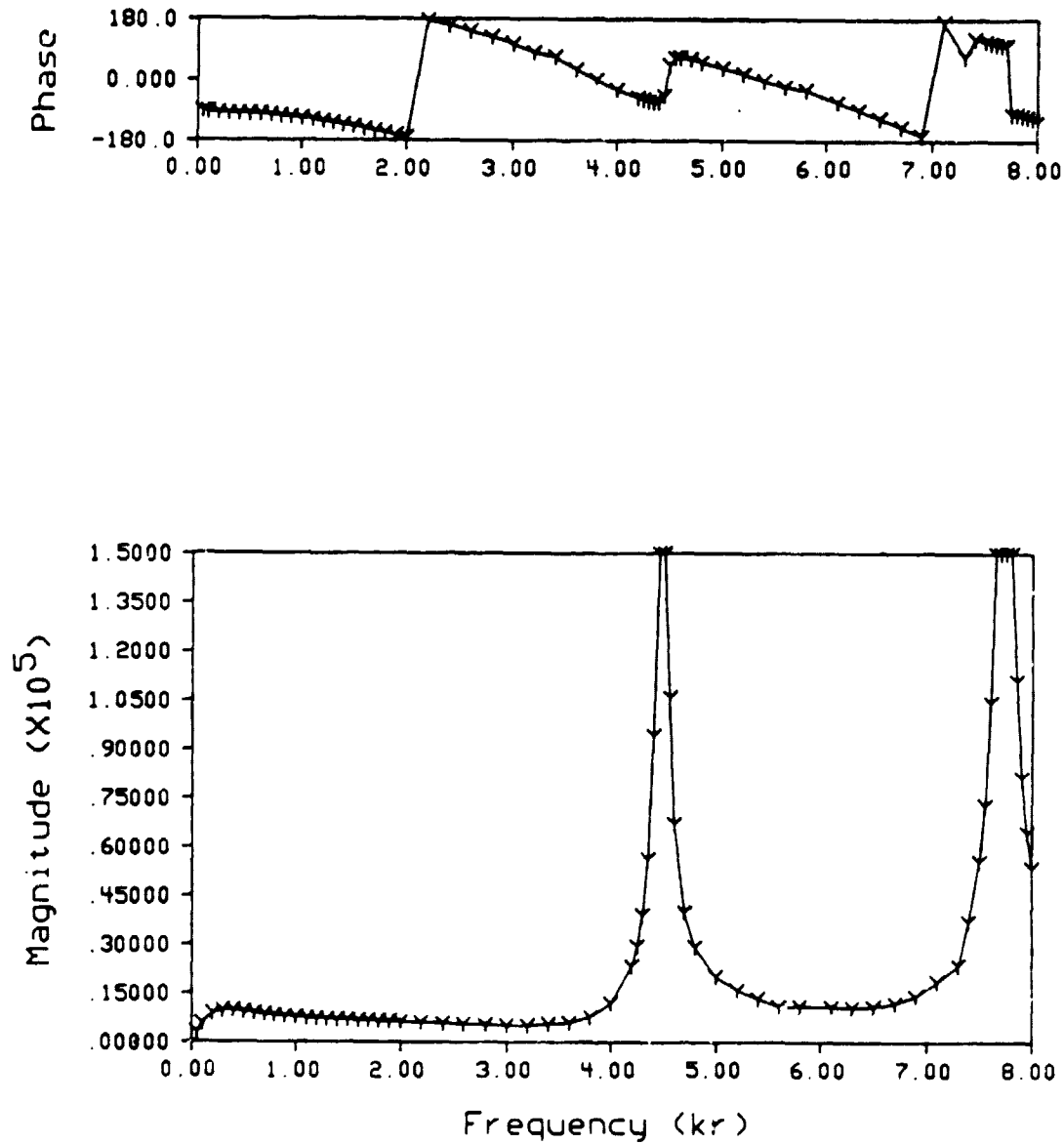


Figure 5.12 - Numerical Response For The Pressure At The Wall Of A Rigid-Walled Spherical Cavity

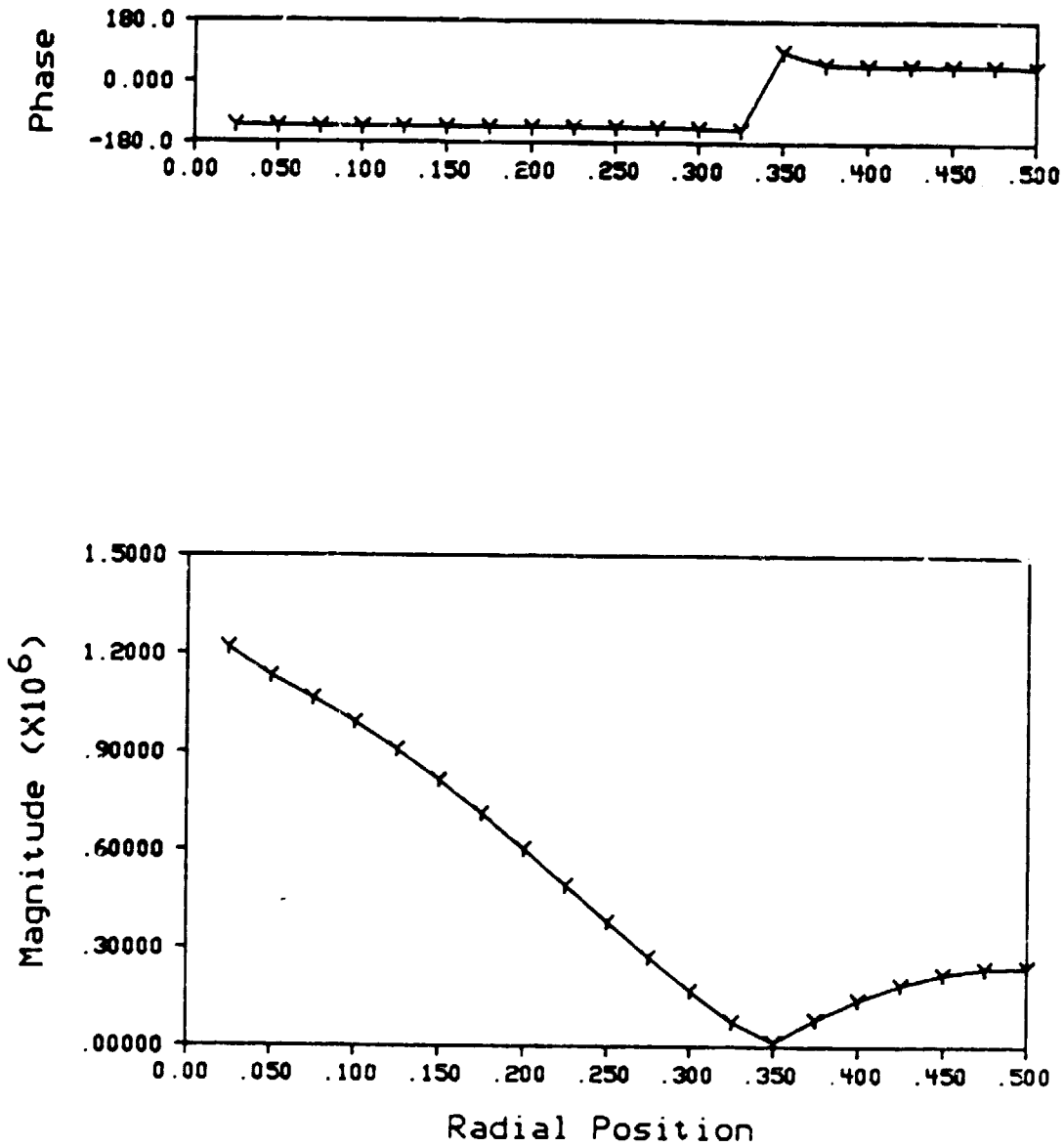


Figure 5.13 - Pressure Distribution In A Rigid-Walled Spherical Cavity With An Applied Source At $kr=4.5$

The rigid-walled spherical cavity response compares well with the response in figure 5.5 in terms of the resonant frequency identification. Both responses identify peaks occurring at approximately 3080 Hz and 5300 Hz (kr 's of 4.493 and 7.725). For the rigid-walled cavity, the pressure magnitudes are much higher due to the effect of the applied source. The phase relationships differ between the two responses for the same reason. The cavity pressure distribution on figure 5.13 exhibits the expected Bessel's function-type behavior. However, the effect of the applied source can be seen near the radial position of zero. Since the pressure at the applied source is infinite, the near-field effect close to a radius of zero is expected. Otherwise, the pressure distribution is dominated by the response of the cavity near the resonant frequency. This behavior could be expected to be much different if the cavity was being excited at a frequency away from a resonant frequency. Note that the low frequency regime in figure 5.12 is characteristic of the low frequency regime in figure 5.5. Once again, the low frequency results are affected by the formulation and do not approach infinity as they should.

In general, the indirect boundary element method has done an excellent job for the variety of spherical cavity problems tested. The models for boundary excitation, internal point source excitations and with impedance

boundary conditions all perform very well with the one exception at low frequency.

5.2 Spherical Model For Radiation

Although the research being presented deals primarily with cavity acoustics, it is possible to deal with acoustical radiation problems applying the same formulation. To do so, the models need only have negated 'free terms' (i.e., the quantity c in equations 4.16b and 4.17b). In other words, instead of having the 'free terms' be negative (as is done for cavity problems), the 'free terms' must be positive.

The acoustical radiation model for the sphere was studied only to determine whether the formulation would fail at the interior eigenfrequencies for the exterior radiation problems. As mentioned in the previous section, this type of formulation failure has been demonstrated by other researchers.

Radiation from a pulsating sphere can be modeled by applying uniform velocity boundary conditions to the sphere and applying the 'free term' negation. The analytical solution for the pressure on the surface of a pulsating sphere is [52]

$$p(r_0) = \rho c V_0 \frac{kr_0}{((kr_0)^2 + 1)} (kr_0 + j) . \quad (5.16)$$

Equation 5.16 was utilized to generate the analytical boundary pressure response in figure 5.14 for a velocity boundary condition of 1.

The sphere model was used to numerically determine a boundary pressure response plot for a pulsating sphere. A uniform velocity boundary condition of 1 was applied to the sphere. The 'free terms' were negative of those used for the spherical cavity studies. Figure 5.15 contains the analytical solution represented by the dashed line and the numerical solution represented by the solid line marked with Y's at discrete frequency points.

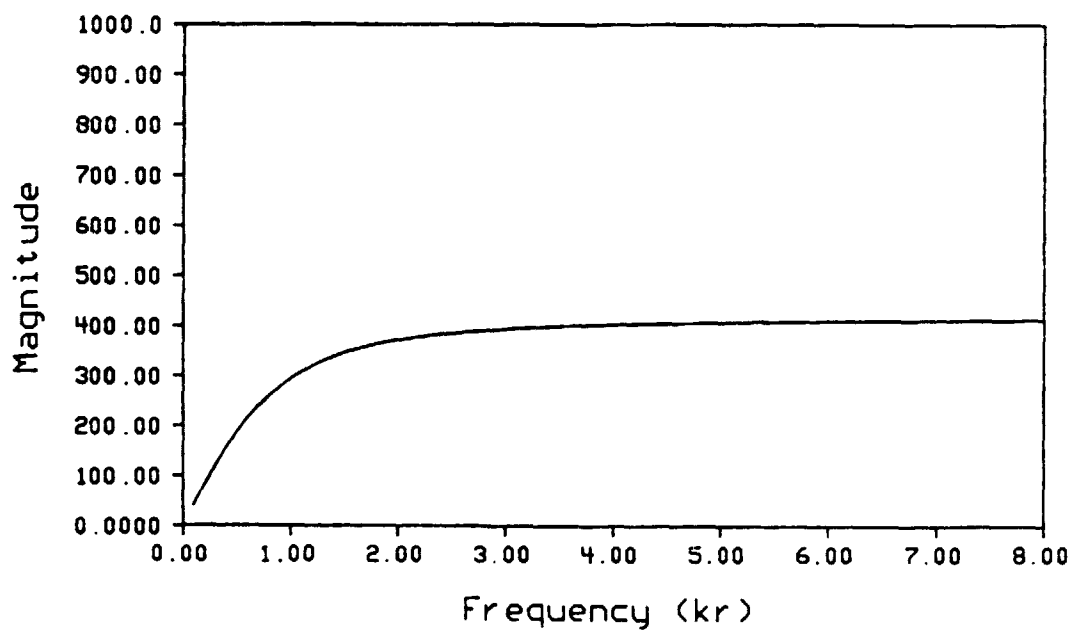
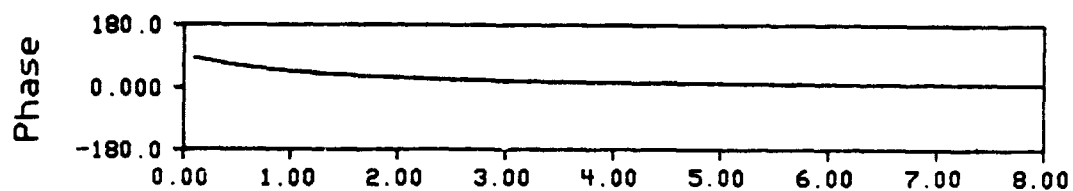


Figure 5.14 - Analytical Pulsating Sphere Boundary Pressure Prediction For Radiation

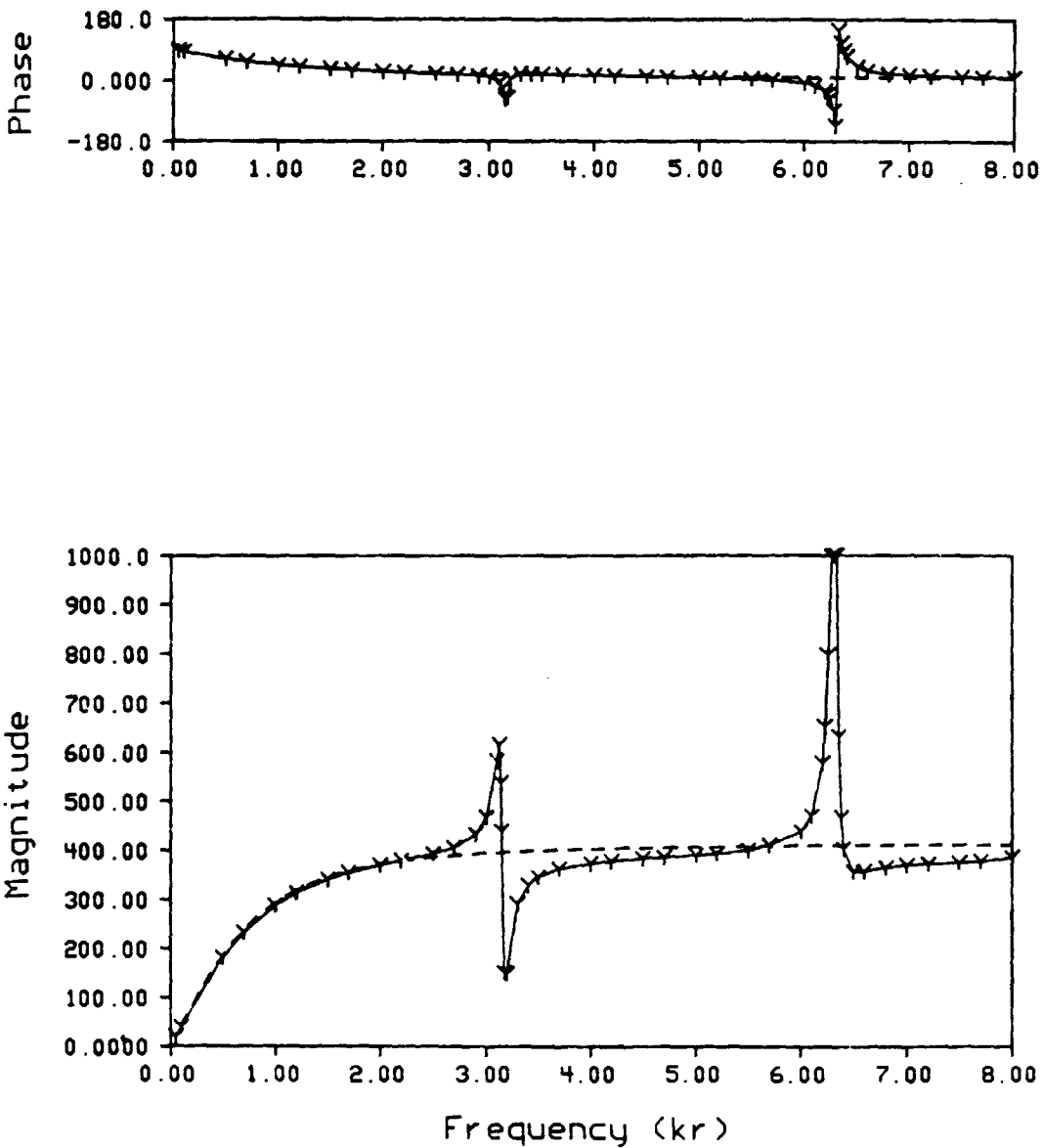


Figure 5.15 - Numerical And Analytical Pulsating Sphere Boundary Pressure Predictions For Radiation

Figure 5.15 very clearly shows that the formulation failures for the radiation problem are present in the formulation being applied in this research. At the interior eigenfrequencies of kr equal to π and 2π , the boundary pressures diverge from the analytical solution. Koopmann and Benner [29] present results for a pulsating sphere which portray the same behavior as shown in figure 5.15. Thus, the conclusion to be drawn is that an overdetermination procedure should be applied if this formulation were to be used for radiation problems. Also, these results lend support to the hypothesis that the difficulties obtained in the low frequency regime for the cavity problems may be due to a formulation failure. Near a frequency of zero, rigid-body modes exist which this formulation is evidently incapable of determining for cavity problems.

5.3 Rectangular Cavity Model

All the results presented heretofore in this chapter have been for a spherical model. For boundary element methods, corners and edges are known to create difficulties for boundary element techniques due to the boundary discontinuities. These difficulties are described in the literature in some detail. Banerjee and Butterfield [12] have devoted an entire chapter in their text to the subject. Although the problem is well-documented, there does not exist one ultimate solution for all cases.

To investigate the consequences of corners and edges, a rectangular cavity with dimensions of 4x5x3 was studied. Three different methods of modeling the corners and edges were attempted. The first method was to model the corners and edges as intersections of adjacent sides. Essentially, the first method is the intuitive approach one would assume having no knowledge of the inherent difficulties. The normal vectors for the nodes on the corners and edges were given components perpendicular to each intersecting wall. The second method involved leaving gaps between the intersecting walls. In essence, the nodes at the corners and edges were not physically attached to adjacent walls of the box. Hence, compatibility of adjacent node points is not enforced. (Element formulations of this type are referred to as 'noncompatible' elements.) The final method involved rounding off the corners and edges to avoid the boundary discontinuities.

To evaluate the three methods of modeling the corners and edges, one wall of the cavity was driven while the remaining five walls were rigid. A simplistic analytical approach for this situation is to consider the problem on a one-dimensional basis as a driven/closed cavity. The pressure solution for this problem is

$$p = \bar{A}e^{jk(L-x)} + \bar{B}e^{-jk(L-x)} \quad (5.17)$$

where L is the length of the cavity in the direction

normal to the driven end, x is the length variable ranging from 0 to L and the constants \bar{A} and \bar{B} are determined by the boundary conditions. The boundary conditions are that the velocity at the closed end is zero ($V(L) = 0$) and the velocity at the driven end is equal to the driving velocity ($V(0) = V_0$). With these boundary conditions and equation 5.17, the approximate analytical pressure solution is

$$p = -j\rho c V_0 \frac{\cos k(L - x)}{\sin(kL)} . \quad (5.18)$$

To quantify equation 5.18, a driving velocity of 1 and a dimension of $L = 5$ (corresponding to the y dimension of the cavity) were used. The pressure distribution along the y coordinate for wave numbers of k equal to 1, 2 and 3 (or frequencies of 343, 686 and 1092 Hz with a speed of sound of 343 m/s) are shown in figures 5.16, 5.17 and 5.18, respectively.

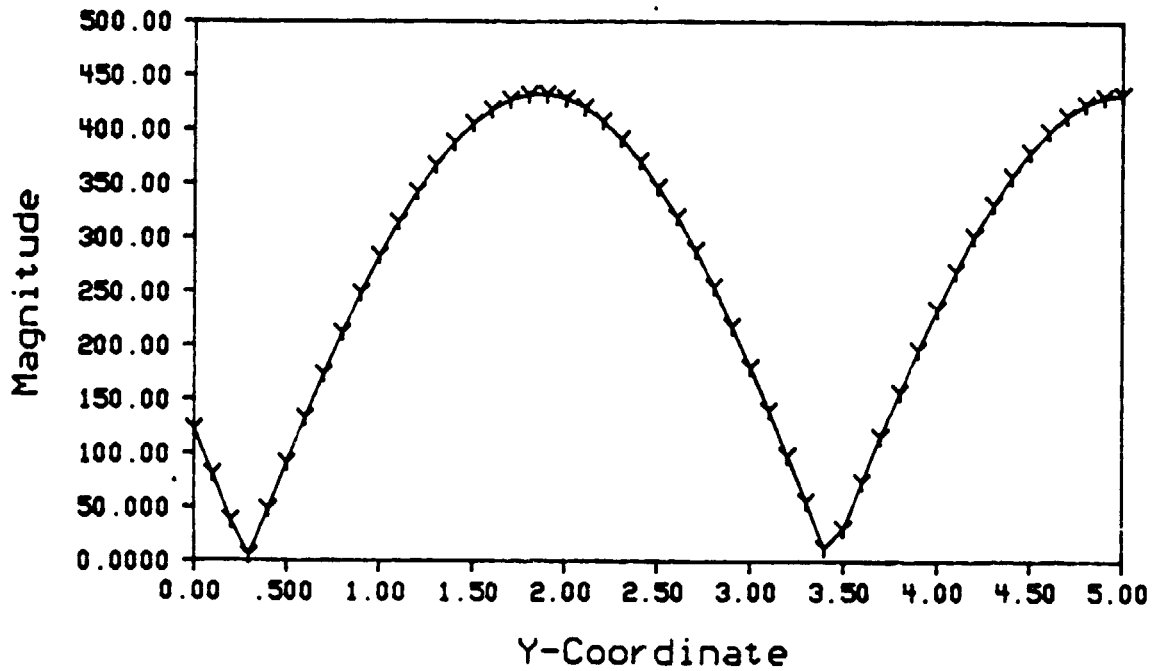
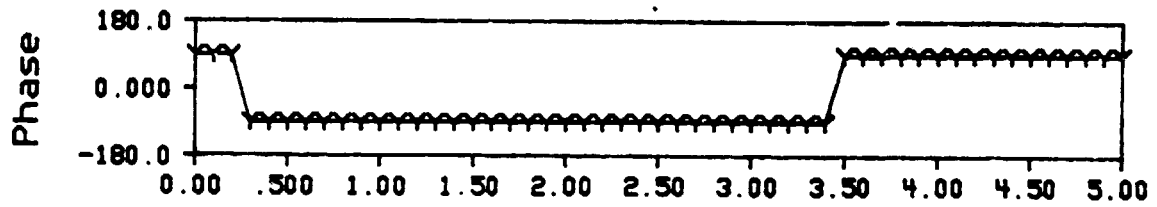


Figure 5.16 - Analytical Pressure Distribution For A Driven/Closed Cavity At $k=1$

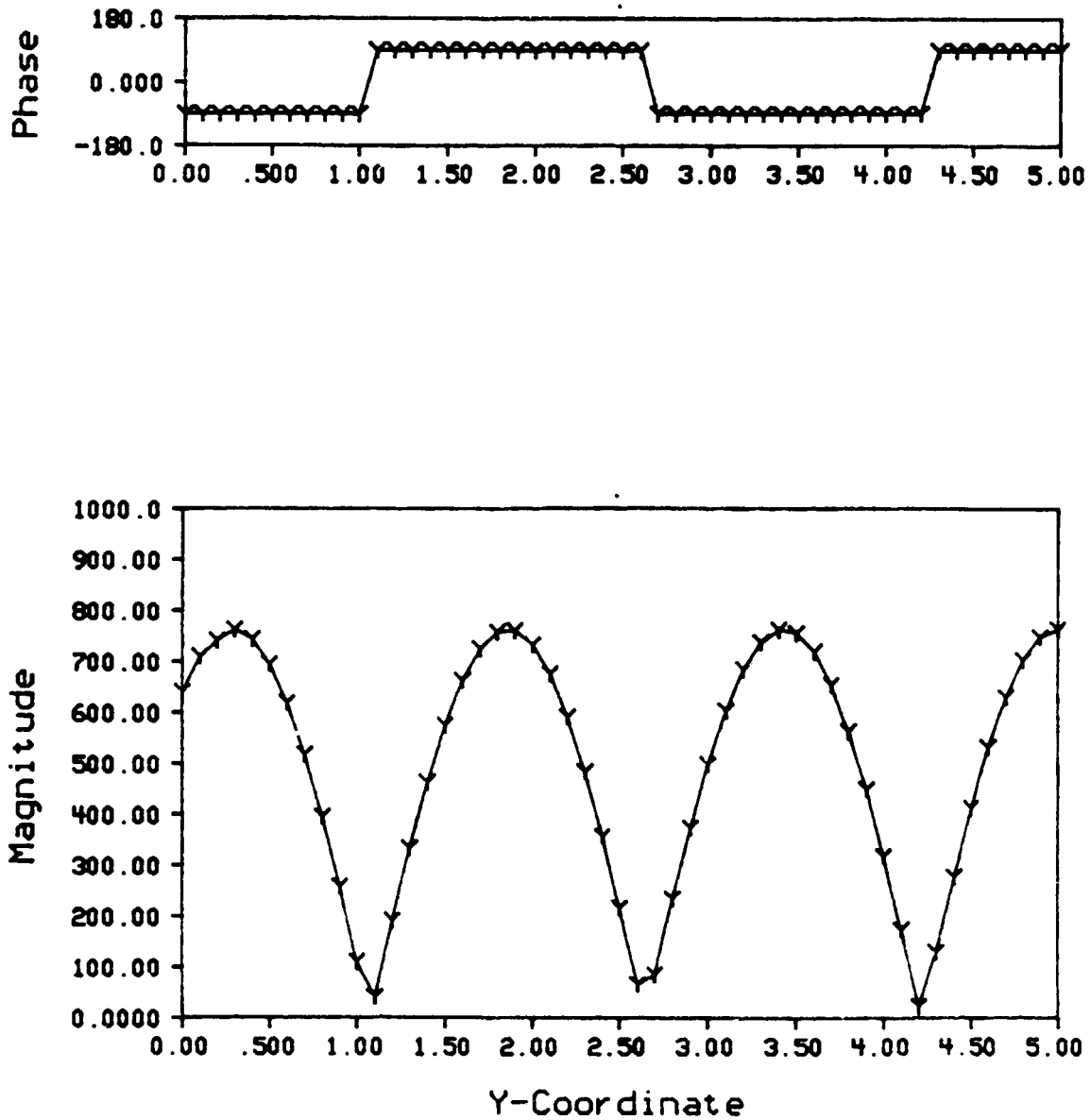


Figure 5.17 - Analytical Pressure Distribution For A Driven/Closed Cavity At $k=2$

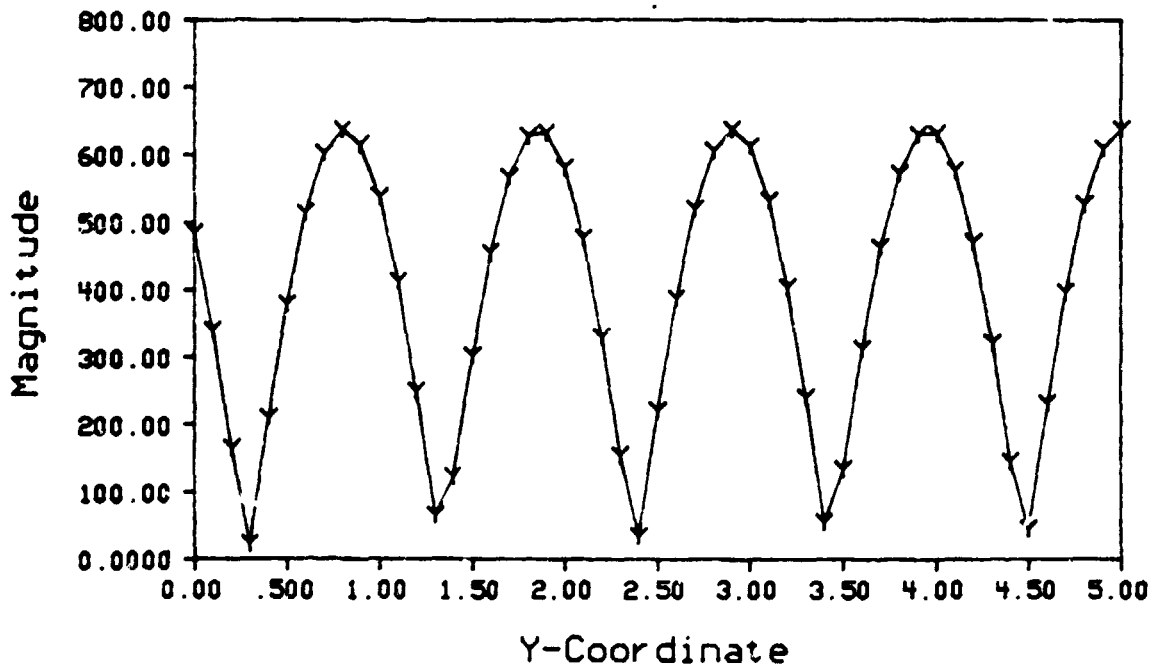
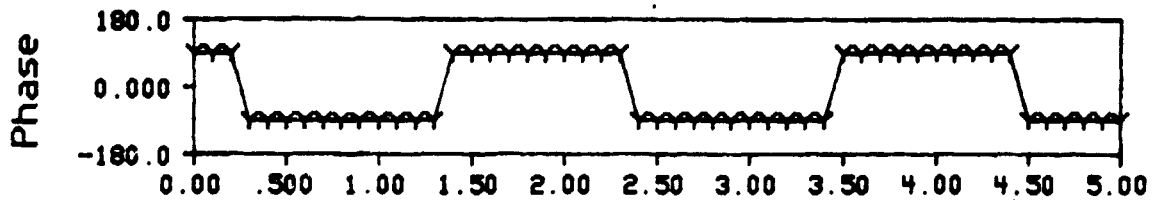


Figure 5.18 - Analytical Pressure Distribution For A Driven/Closed Cavity At $k=3$

Boundary element models incorporating the three corner and edge methods were used to numerically evaluate a driven/closed cavity. However, the driving velocity was not uniform as assumed in the analytical solution. An attempt to produce such a situation is impossible in the first and third models because the normal velocity at the corner nodes must be compatible on both walls. Imposing such a boundary condition would cause the adjacent walls to be non-rigid in the first and third models. Consequently, a velocity profile having a magnitude of 1 at the center but varying linearly to zero at the edges was applied to the driving wall (i.e., the wall at y equal to zero). Pressure distributions were calculated for wave numbers of k equal to 1, 2 and 3 just as for the analytical solution. The numerical results are shown in figures 5.19, 5.20 and 5.21 for the first model (the true box), figures 5.22, 5.23 and 5.24 for the second model (the gapped box) and figures 5.25, 5.26 and 5.27 for the third model (the rounded box).

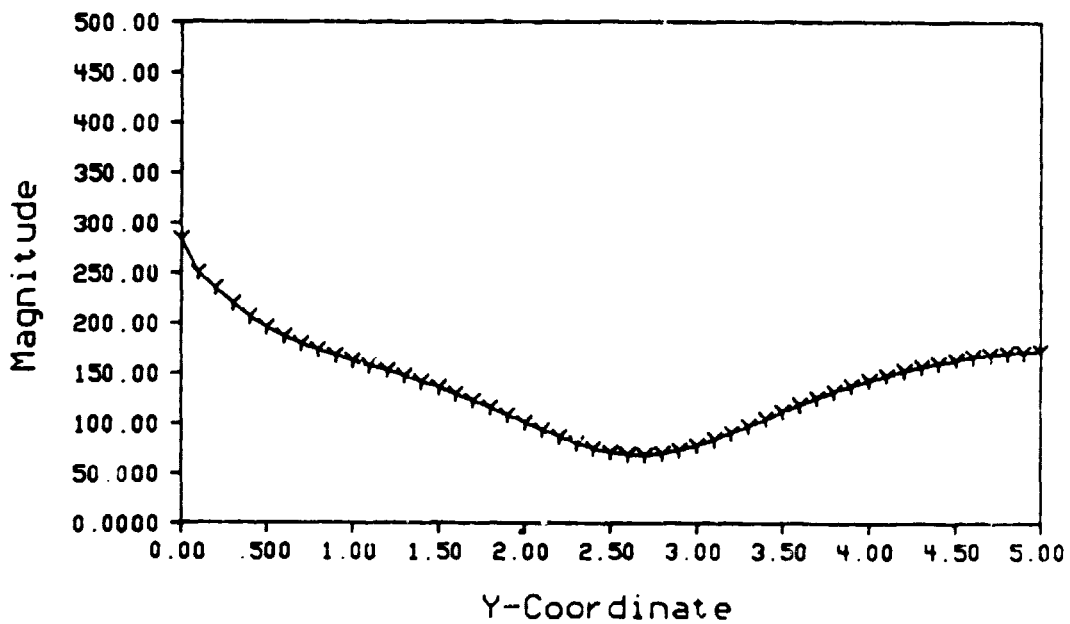
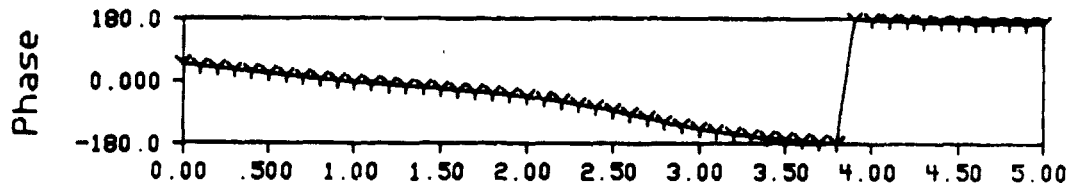


Figure 5.19 - Pressure Distribution For First Box Model At $k=1$

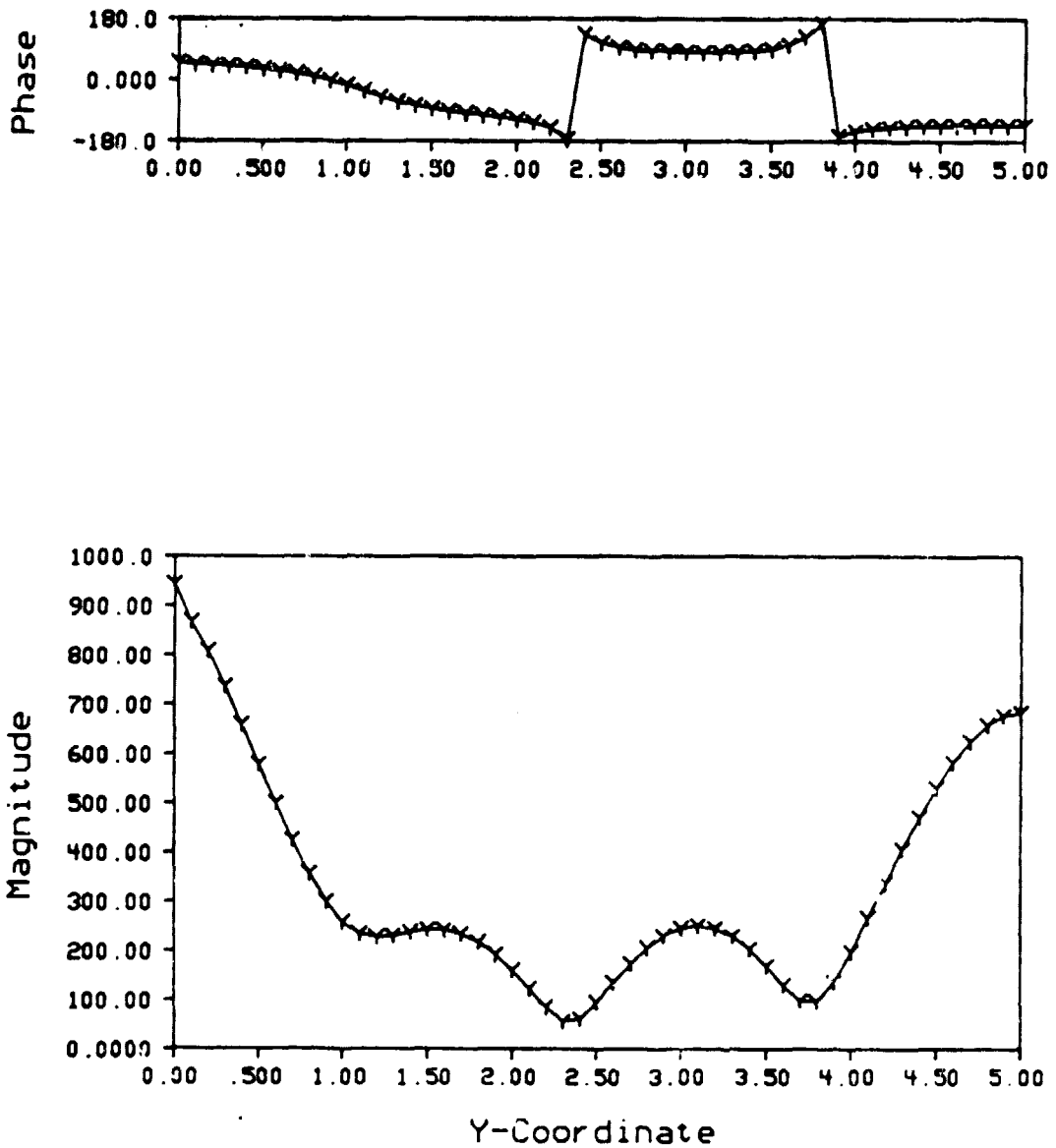


Figure 5.20 - Pressure Distribution For First Box Model At $k=2$

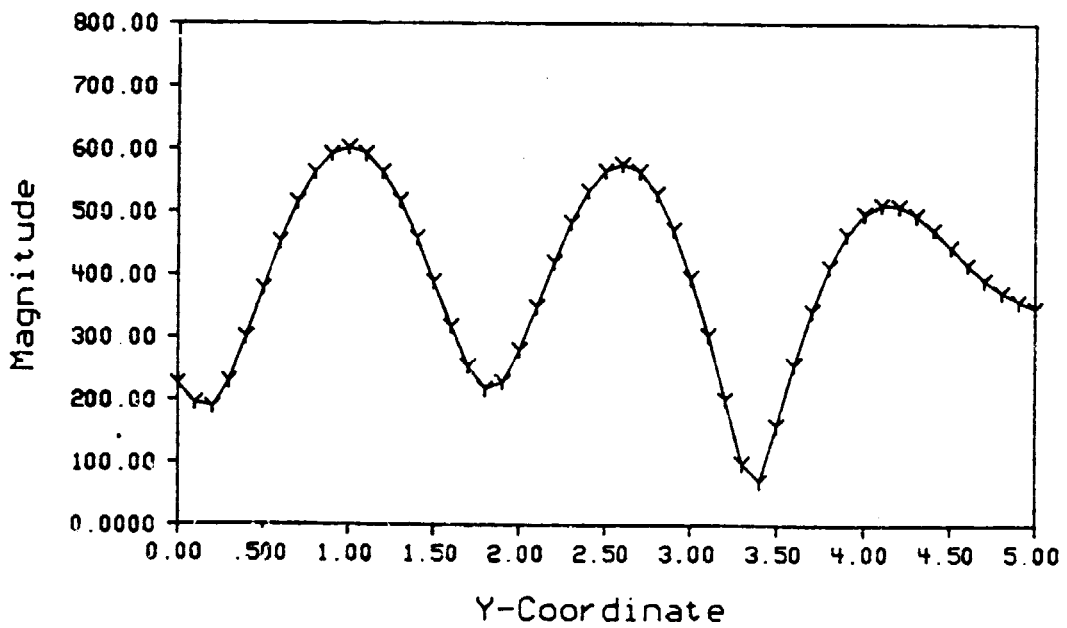
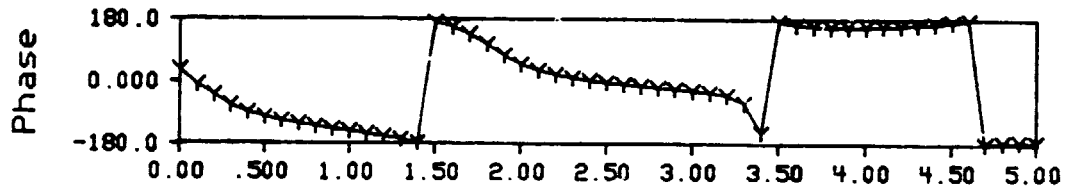


Figure 5.21 - Pressure Distribution For First Box Model At $k=3$

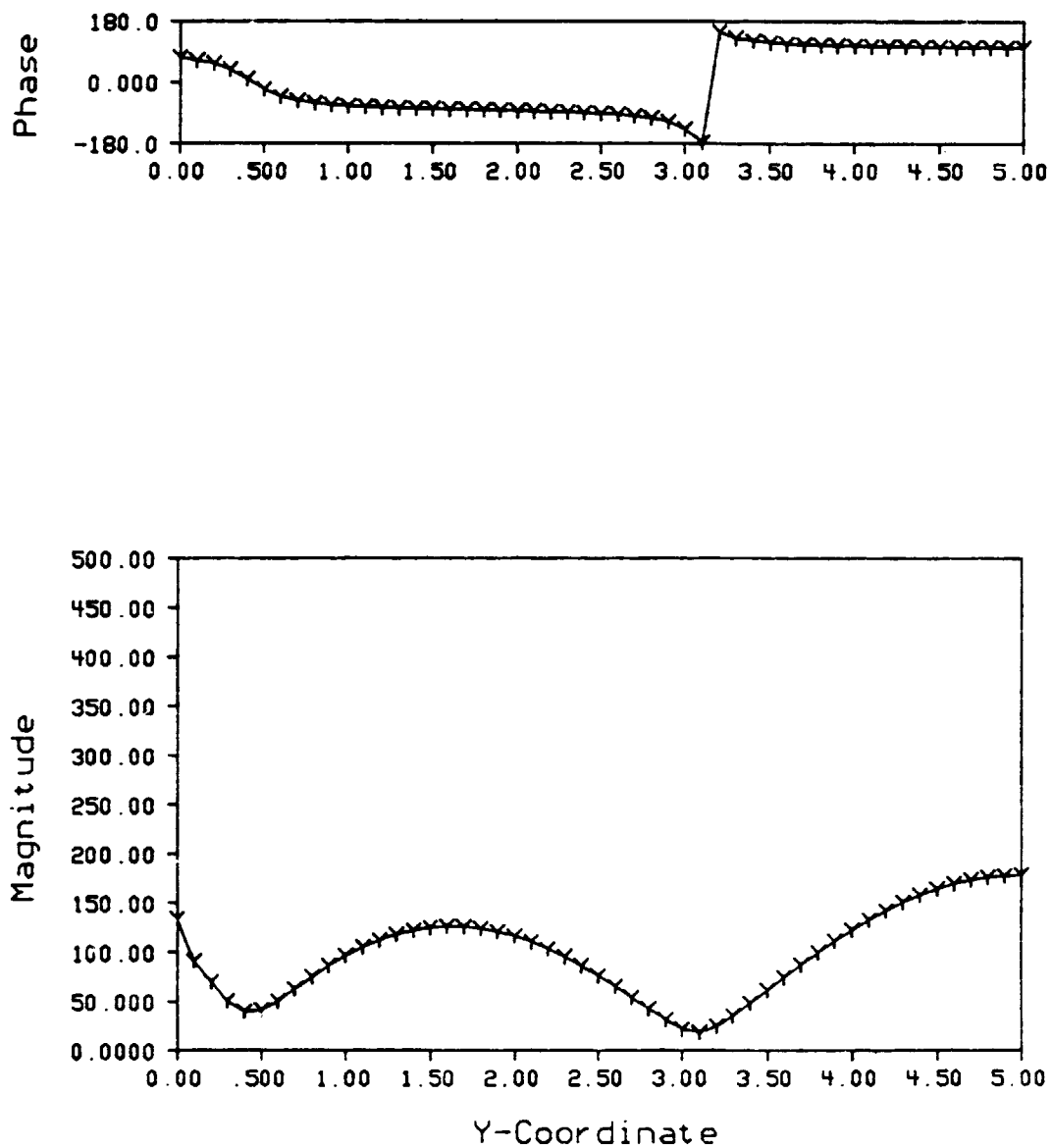


Figure 5.22 - Pressure Distribution For Second Box Model
At $k=1$

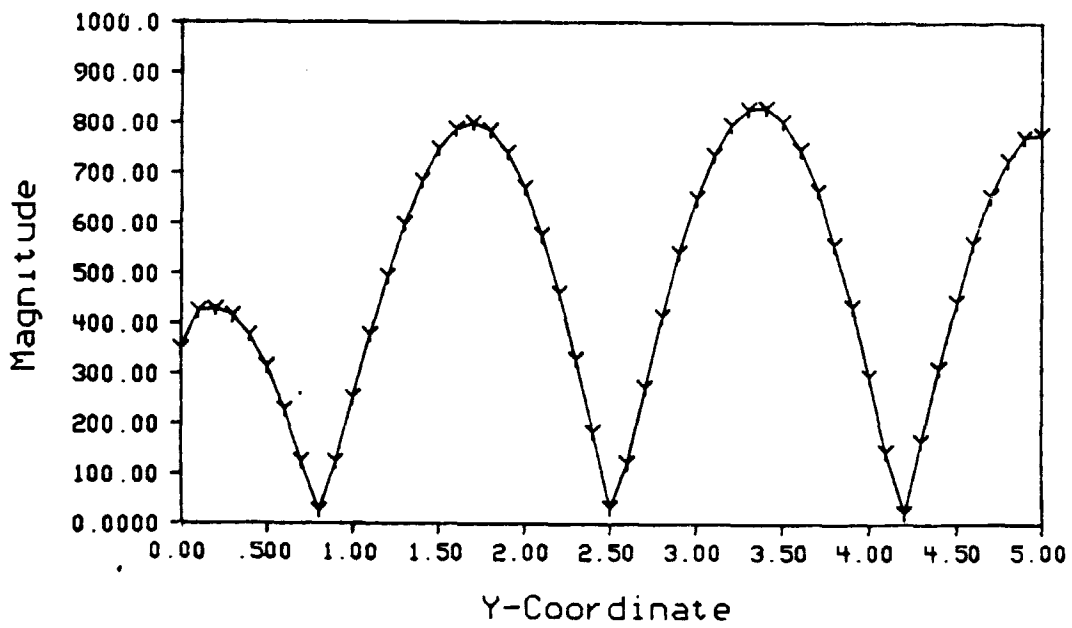
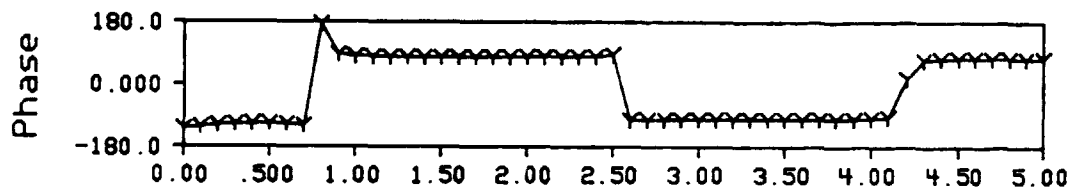


Figure 5.23 - Pressure Distribution For Second Box Model
At $k=2$

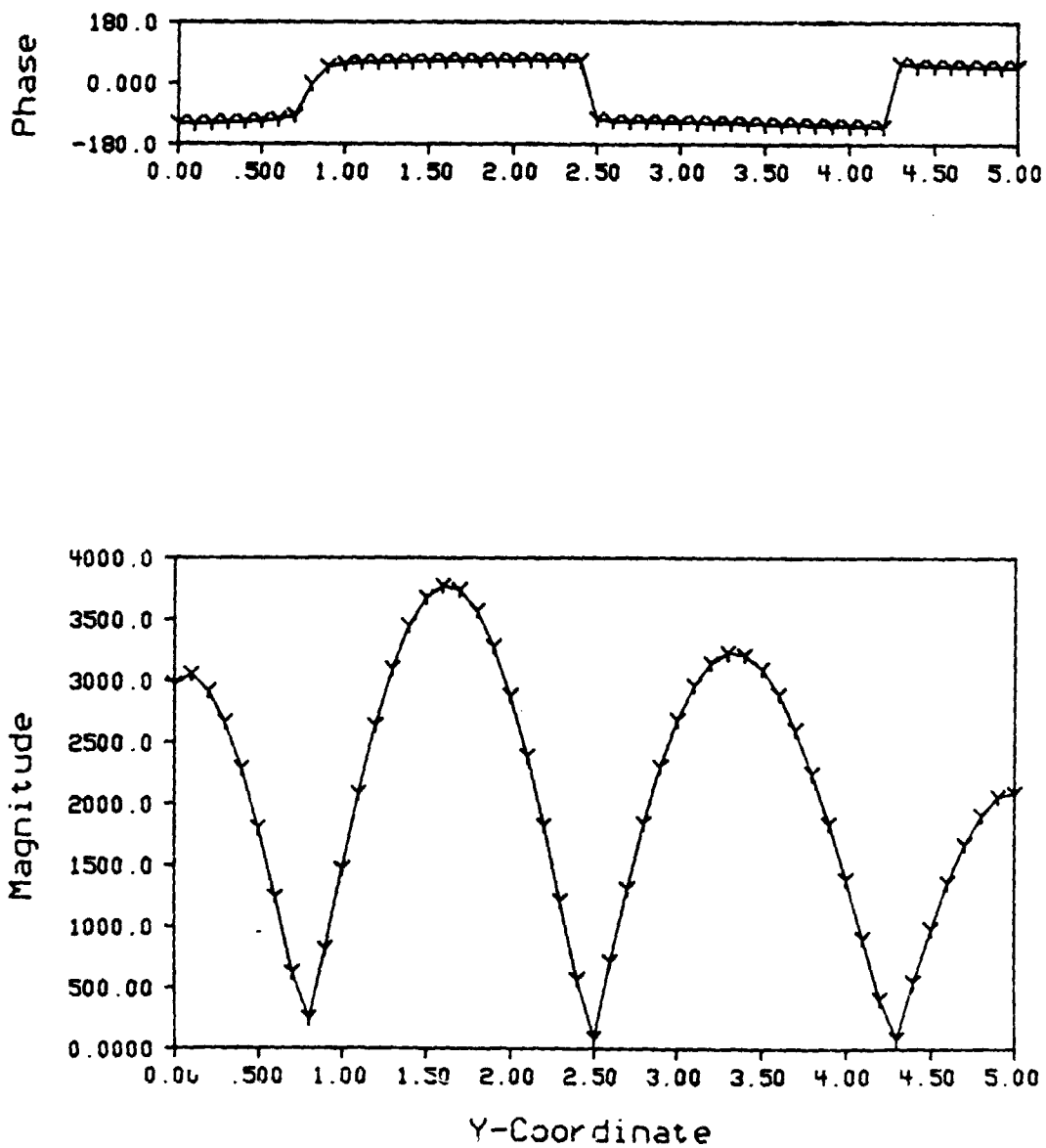


Figure 5.24 - Pressure Distribution For Second Box Model
At $k=3$

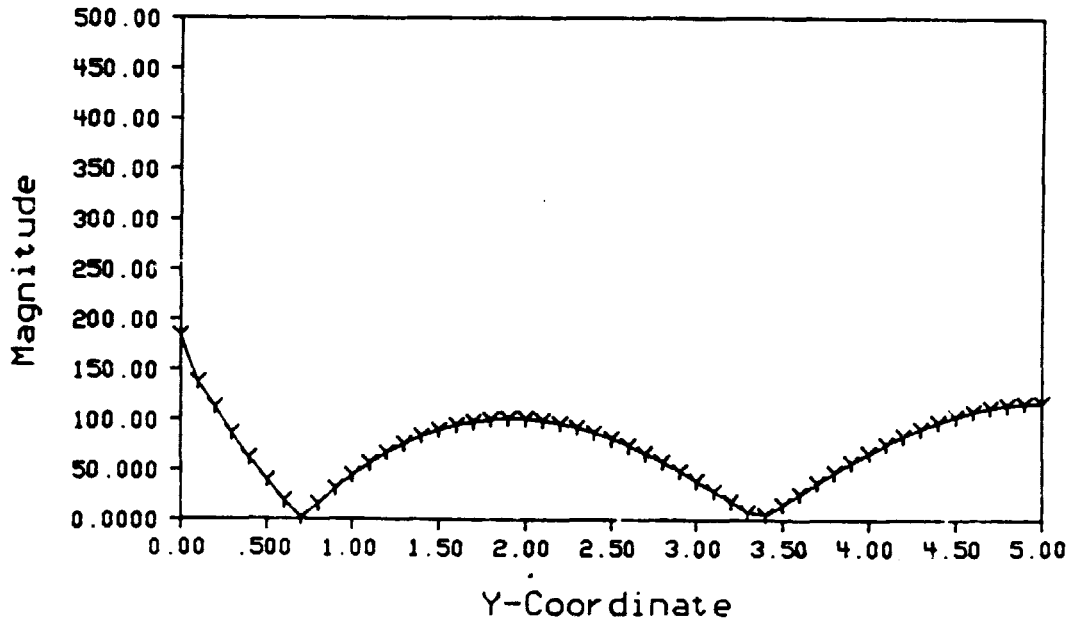
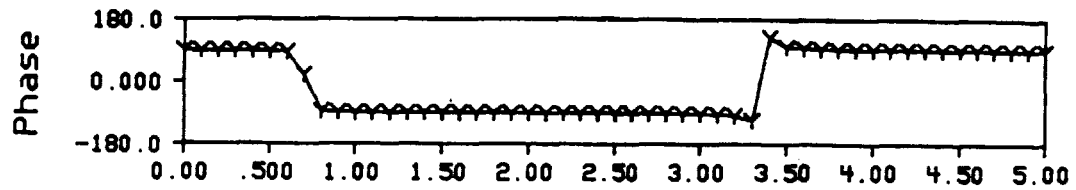


Figure 5.25 - Pressure Distribution For Third Box Model At $k=1$

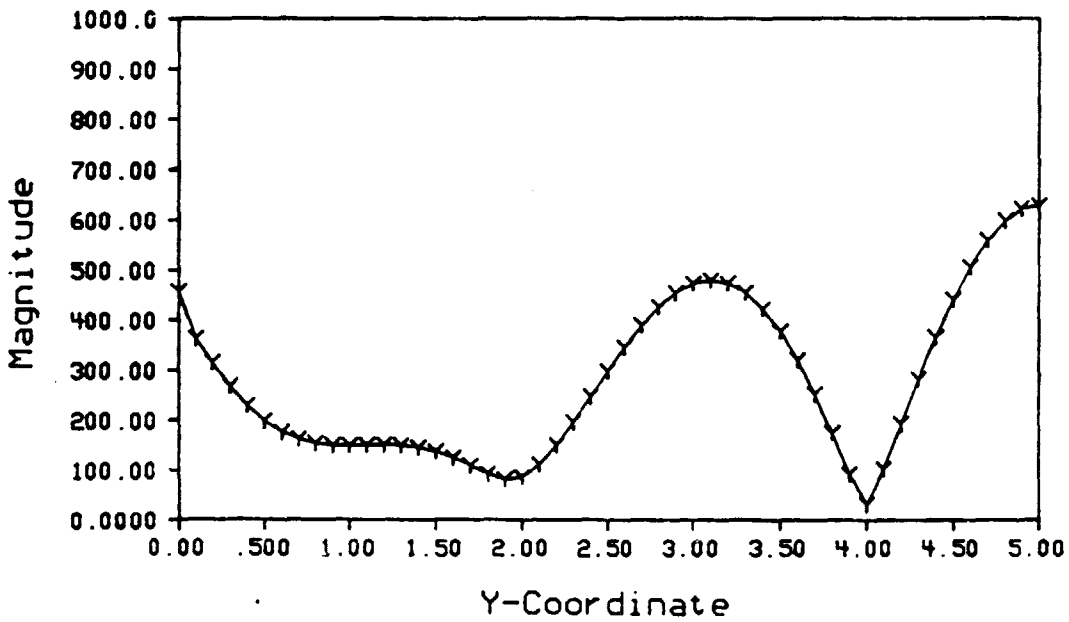
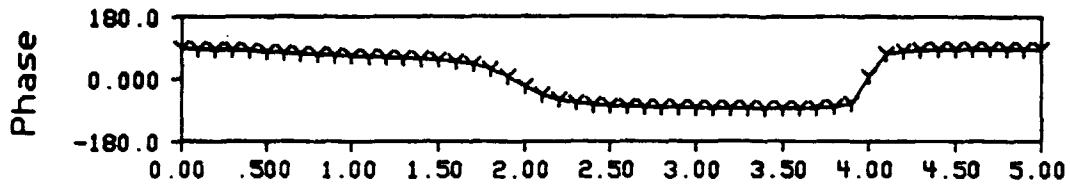


Figure 5.26 - Pressure Distribution For Third Box Model At $k=2$

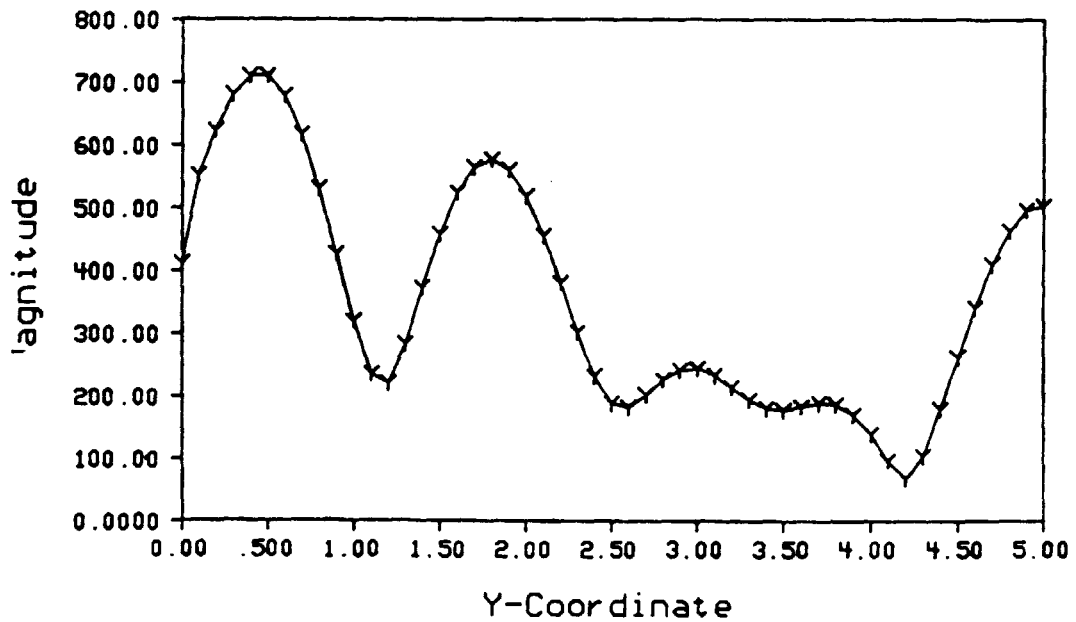
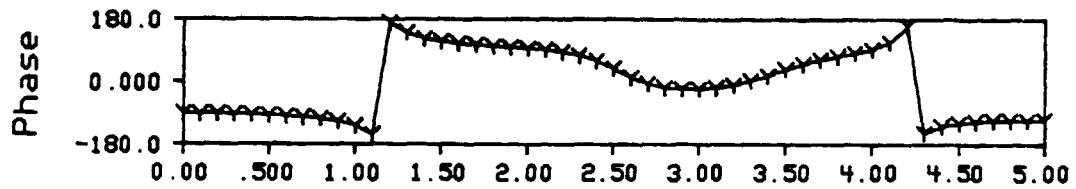


Figure 5.27 - Pressure Distribution For Third Box Model At $k=3$

Two points must be made regarding the numerical models. Firstly, the excitation at the driving wall is not uniform as in the analytical solution. Secondly, the numerical models are three-dimensional. Thus, one can not expect purely one-dimensional results, especially when the excitation at the driving wall is not purely one-dimensional. These points need be highlighted to provide explanations for the differences between the analytical and numerical solutions.

With the previous points in mind, some qualitative judgements can be made on the three numerical models. The analytical solutions in figures 5.16 through 5.18 can be used as guidelines to evaluate the three models. For all three frequencies, the analytical solutions are cosinusoidal in nature. The numerical results for the first model appear to exhibit some form of sinusoidal behavior for the second and third wave numbers but not as clearly defined as would be expected either in magnitude or phase. The second model shows more clearly cosinusoidal behavior in the pressure distribution. Phase shifts of 180° are evident at positions of zero pressure magnitude. There is some variability in the peak magnitudes within an individual pressure distribution. However, it is quite possible that the variability is due to cross-coupling with modes in the other two orthogonal directions since the absolute maximums occur near the center of the cavity

(e.g., figure 5.24). Finally, the third model, the rounded corner model, shows cosinusoidal behavior at the first wave number but not at the second or third wave numbers. The pressure magnitudes are not regular peaks nor are any clearly defined phase shifts evident. As a result of this numerical study, the second method of modeling the corners and edges, that of providing gaps, appears to be the best of the three methods and is also the one often recommended in the literature (e.g., [12]). It should also be noted that another solution which should be investigated for acoustical problems is the use of 'noncompatible' elements. In 'noncompatible' elements, the node points lie in the interior of the element rather than on the edges. Many of the problems encountered here will not be a consideration with 'noncompatible' elements.

After determining that the gapped edge model provided the best results of the three models studied, the gapped edge model was utilized to study the internal source excitation problem of the rectangular cavity. The boundary conditions for the response study were rigid-wall boundary conditions. Excitation of the model was supplied by a source placed in the center of the rectangular cavity. The strength of the source was 1. For a rigid-walled rectangular cavity, the pressure distribution in terms of modal response will be of the form [53]

$$p = \sum_l \sum_m \sum_n \bar{A}_{lmn} \cos\left(\frac{l\pi x}{L_x}\right) \cos\left(\frac{m\pi y}{L_y}\right) \cos\left(\frac{n\pi z}{L_z}\right) \quad (5.19)$$

where L_x , L_y and L_z are the dimensions of the rectangular cavity in the x, y and z directions, respectively and \bar{A}_{lmn} is the modal amplitude. The modal amplitude will depend on the closeness of the driving frequency to a natural frequency and also on the coupling of the exciter to the mode. Since an applied source is placed at the center of the cavity for excitation purposes, the odd modes will not be excited. (Odd modes means that the variables l, m or n in equation 5.19 are odd numbers.) The applied source creates pressure antinodes in the center of the cavity. Hence, only even modes should be excited.

The numerically determined response plots for the rigid-walled rectangular cavity are shown in figures 5.28, 5.29 and 5.30. The pressures shown in the response plots are associated with a point located in the center of a wall of the cavity. For example, the x direction response is for a point located in the center of a wall having a constant x coordinate (i.e., a wall parallel to the yz plane). The response plots indicate resonant frequencies by the significant peaks in the magnitudes and shifts in the phase. Incidentally, the difficulties in the low frequency regime are apparent again in these response plots below a wave number of about 0.25.

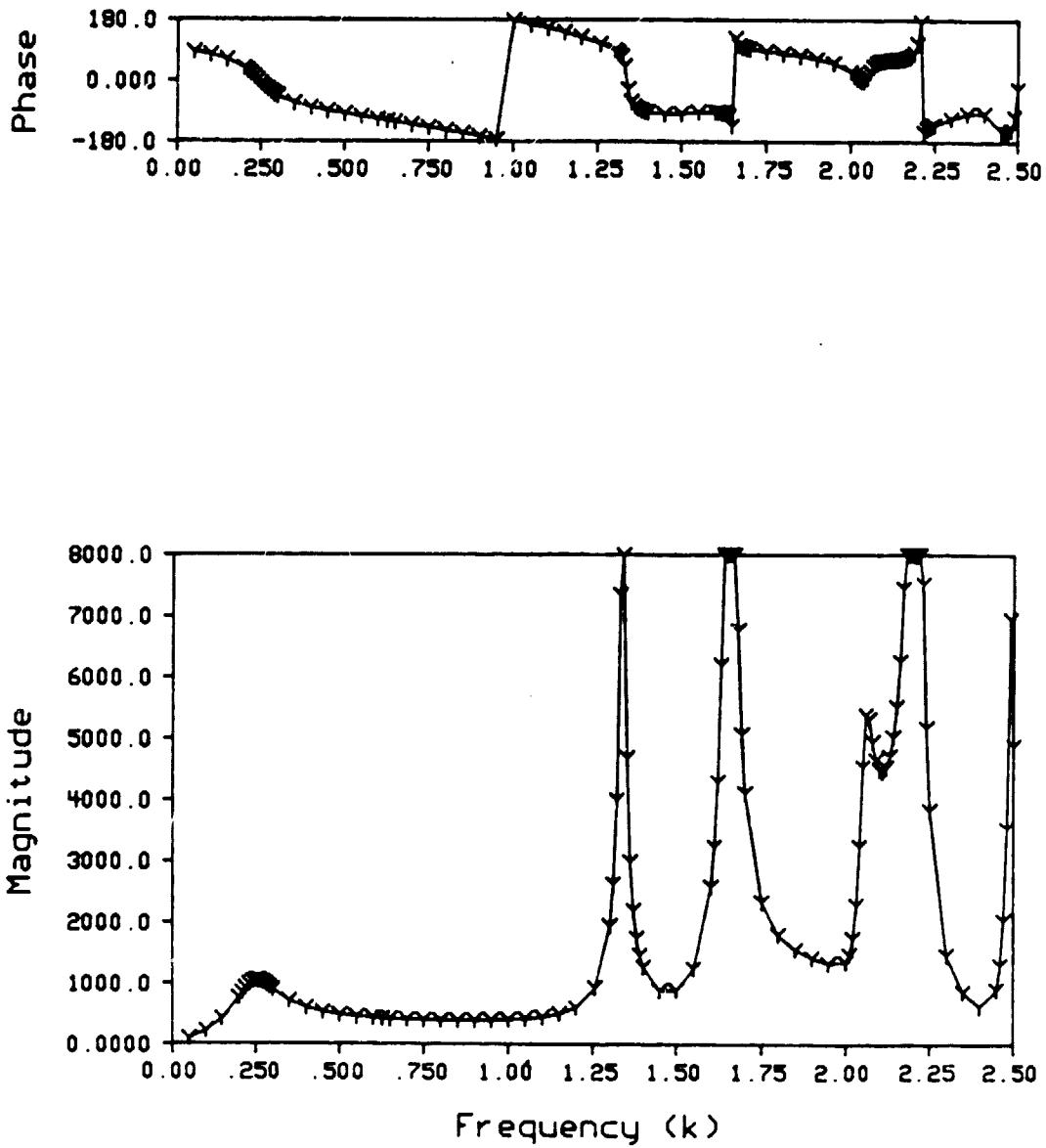


Figure 5.28 - Rectangular Cavity Pressure Response - X Direction

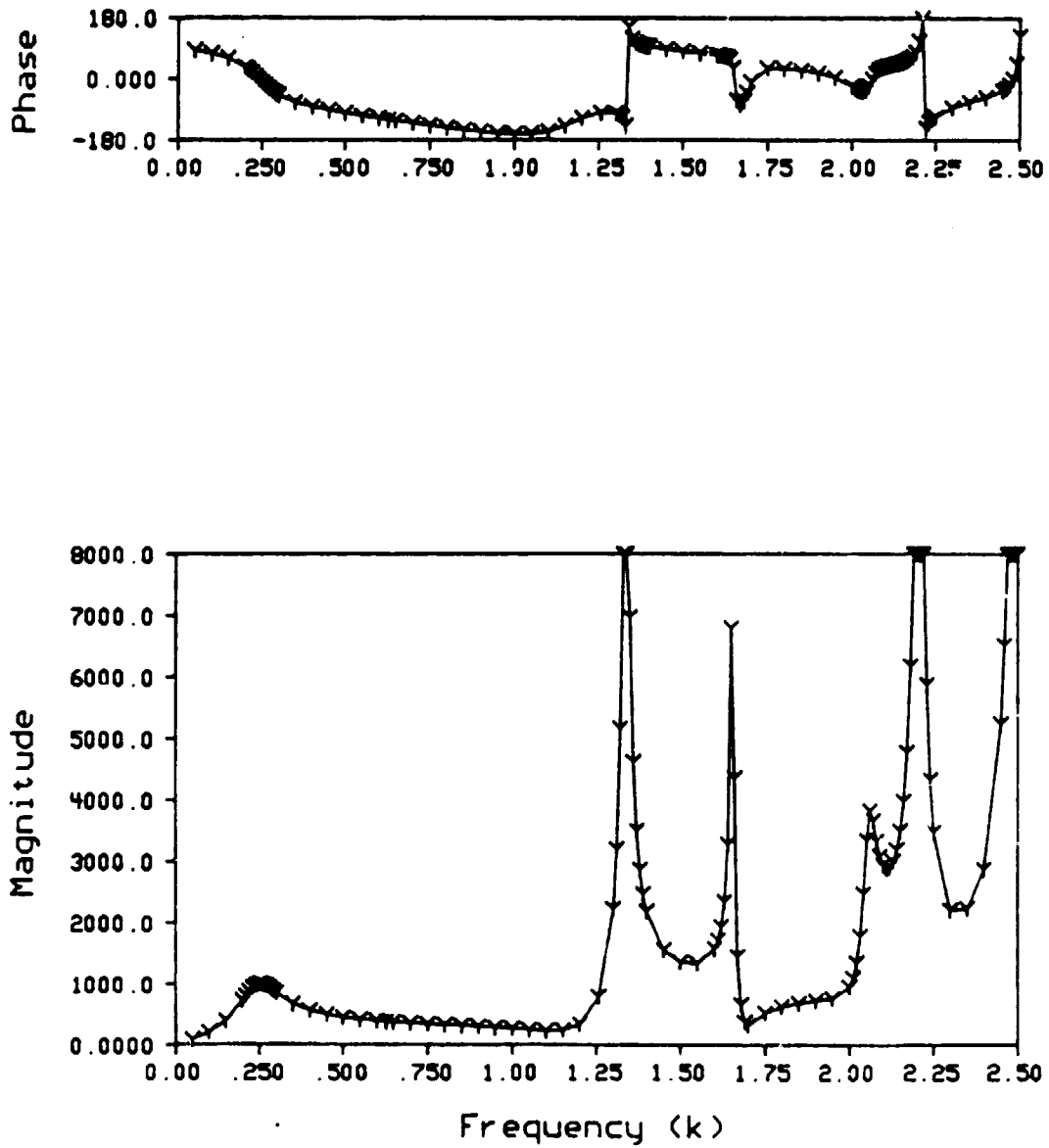


Figure 5.29 - Rectangular Cavity Pressure Response - Y Direction

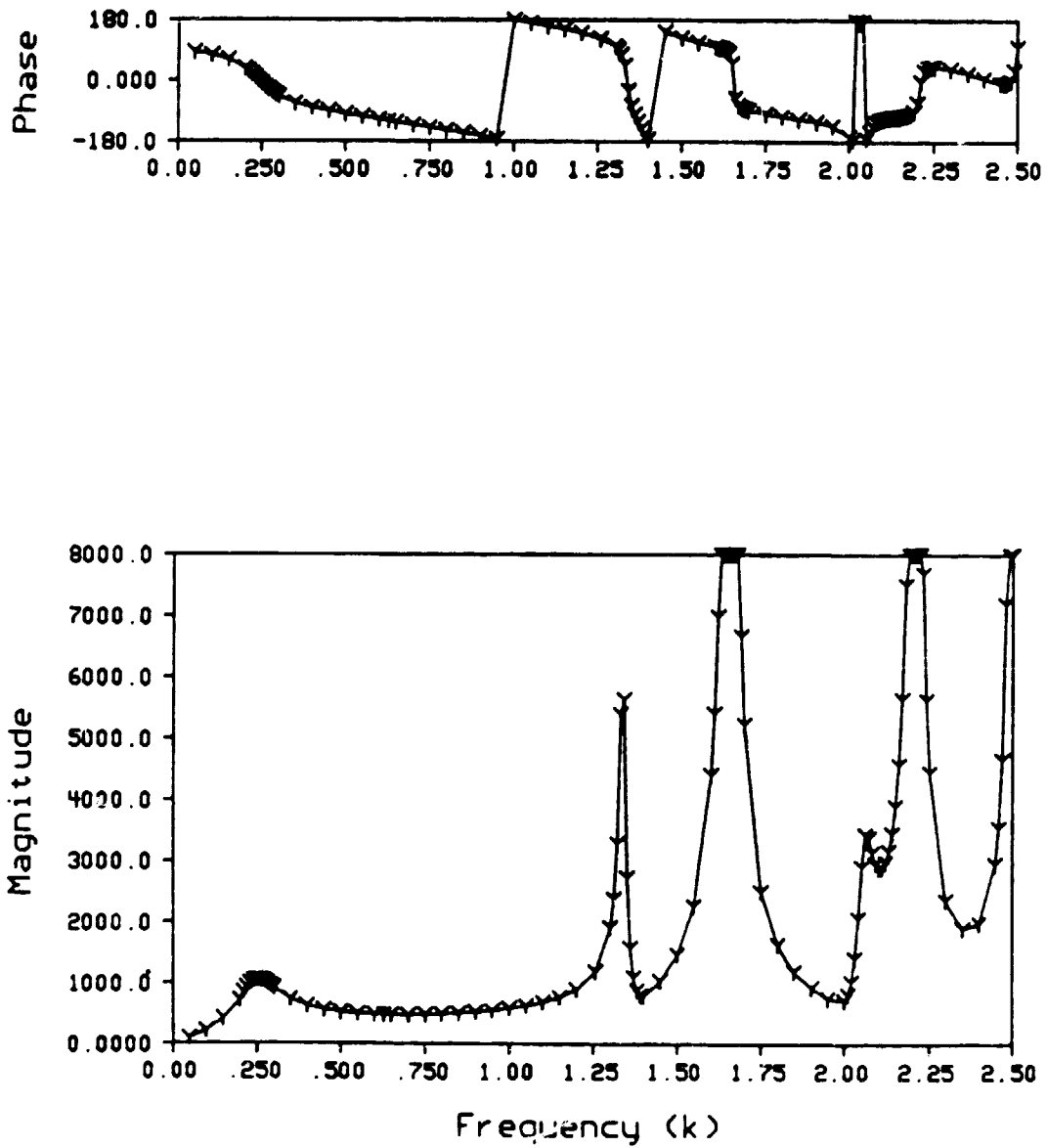


Figure 5.30 - Rectangular Cavity Pressure Response - Z Direction

Pressure distributions within the rectangular cavity were generated from the numerical results to identify the pressure response shapes occurring at resonant frequencies. Near the resonant frequencies the response should be dominated by the respective mode shape. Between resonance, it would be expected that the response would be lower and would be a superposition of all the near-frequency resonant mode shapes. Since the cavity and pressure distributions are three-dimensional, the pressure distributions were determined for planes perpendicular to one of the orthogonal directions and passing through the center of the rectangular cavity. Thus, for each response at which a distribution is determined, three plots are generated; one in each of the three orthogonal planes. Furthermore, the magnitude at the center of all the magnitude plots is infinite and the phase at the center of the phase plots is -90° because of the applied source. As a result, the response of the center point is truncated to the level of the maximum pressure magnitude.

From the cavity response, the first resonant frequency occurs at a wave number of 1.34 (460 Hz). The pressure distribution within the rectangular cavity was generated at that wave number. The pressure distribution of the variations in the z direction is shown in figure 5.31. Likewise, figure 5.32 is the y variations and figure 5.33 is the x variations. Figure 5.31 indicates a possible

cosinusoidal variation in magnitude along the y coordinate which is confirmed by the clearly defined 180° phase shift along the y coordinate. Relatively constant pressures are displayed in figure 5.32. The sinusoidal variation in the y coordinate is evident again in figure 5.33. It is readily apparent that the $(0,2,0)$ mode is the resonant mode shape at 460 Hz. Analytically, the $(0,2,0)$ mode shape occurs at $k = \frac{2\pi}{5}$ or 432 Hz. The conclusion is that the boundary element model successfully located the first resonant frequency with about a 6% upward shift in the frequency.

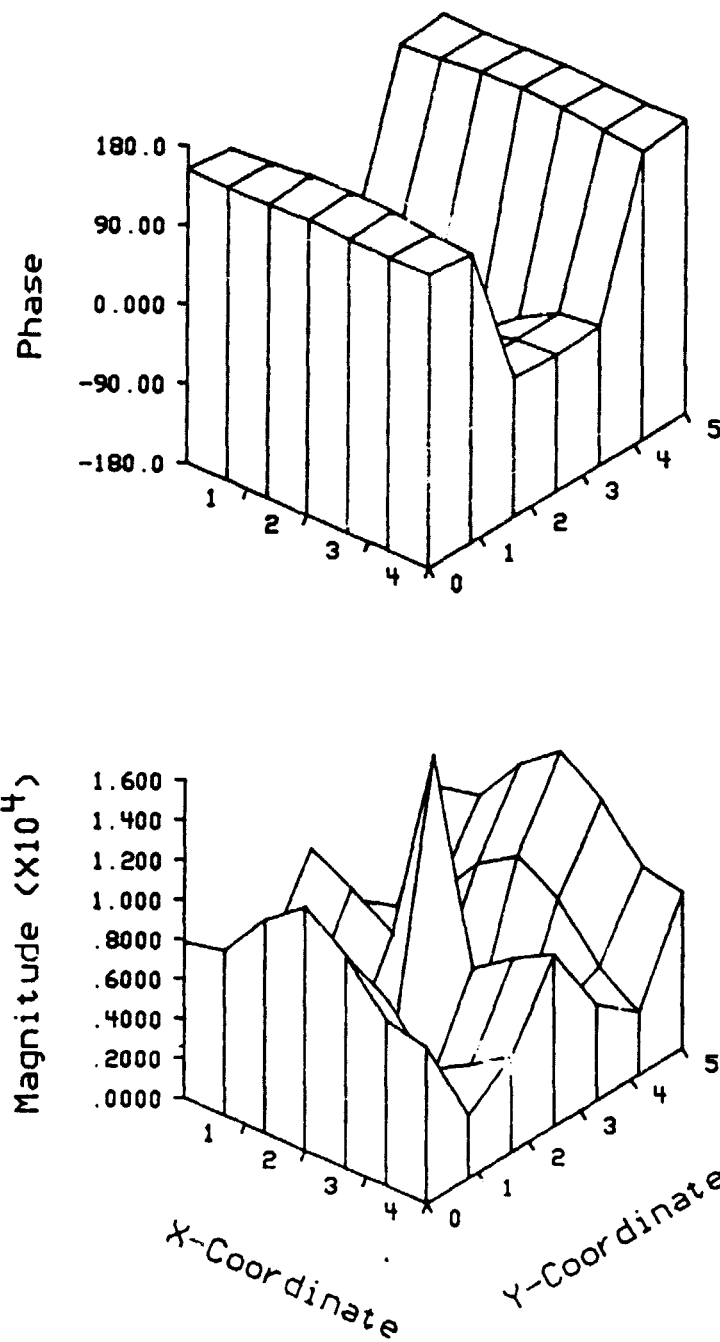


Figure 5.31 - Rectangular Cavity Pressure Distribution At $k=1.34$ (XY Plane)

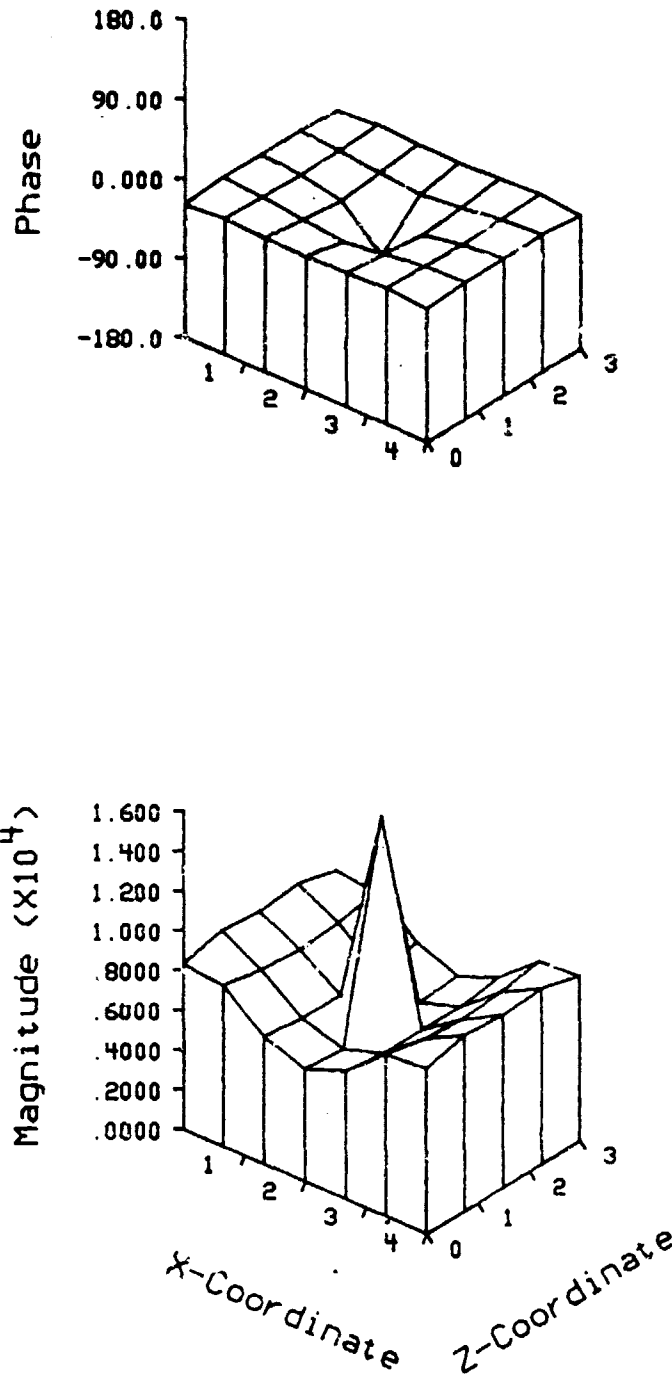


Figure 5.32 - Rectangular Cavity Pressure Distribution At $k=1.34$ (XZ Plane)

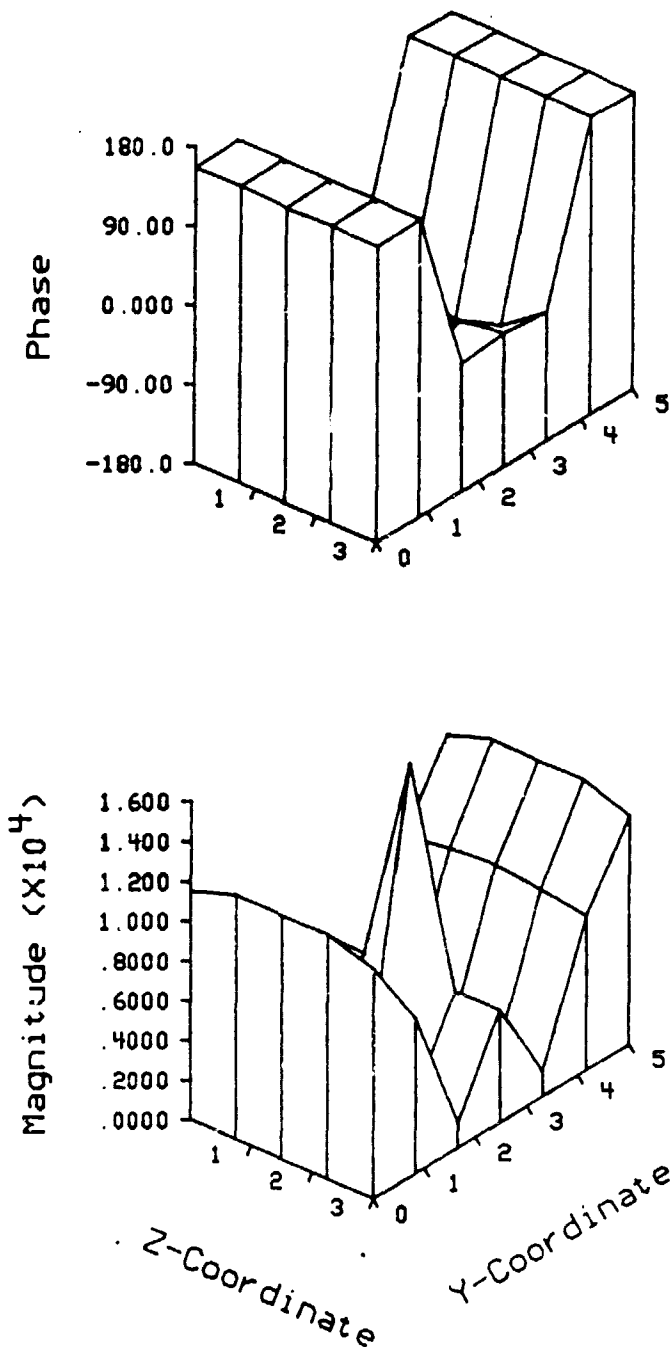


Figure 5.33 - Rectangular Cavity Pressure Distribution At $k=1.34$ (ZY Plane)

The second resonance condition occurs at a wave number of about 1.65 (566 Hz). The pressure distributions within the rectangular cavity are given in figures 5.34 through 5.36. A cosinusoidal variation along the x direction is indicated by the magnitudes and by the 180° phase shifts in figures 5.34 and 5.36. Hence, the (2,0,0) mode shape appears to be the dominant mode at 566 Hz. The (2,0,0) mode occurs analytically at $k = \frac{2\pi}{4}$ or 539 Hz. For the second resonant condition, the boundary element model located the resonance with a 5% upward shift in the frequency.

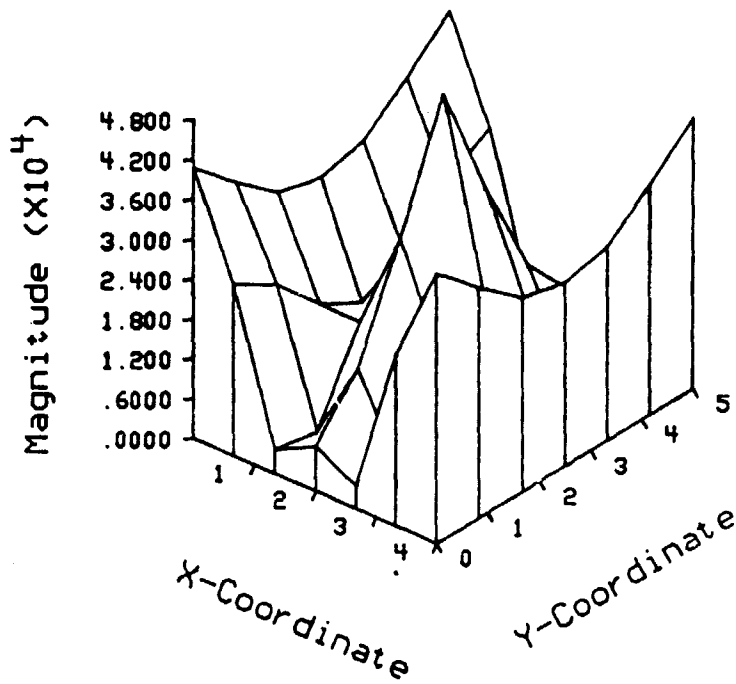
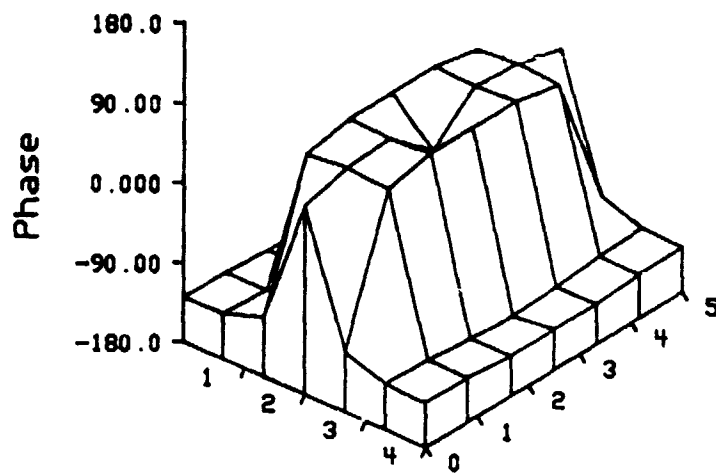


Figure 5.34 - Rectangular Cavity Pressure Distribution At $k=1.65$ (XY Plane)

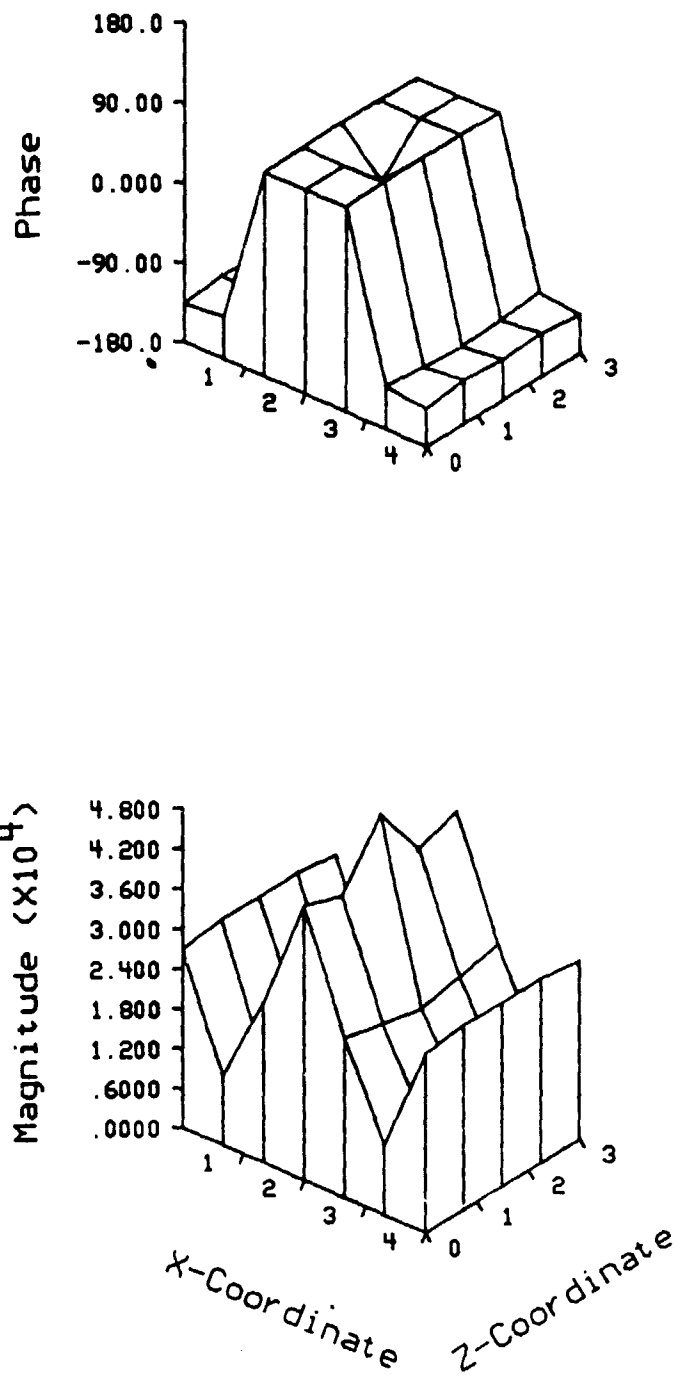


Figure 5.35 - Rectangular Cavity Pressure Distribution At $k=1.65$ (XZ Plane)

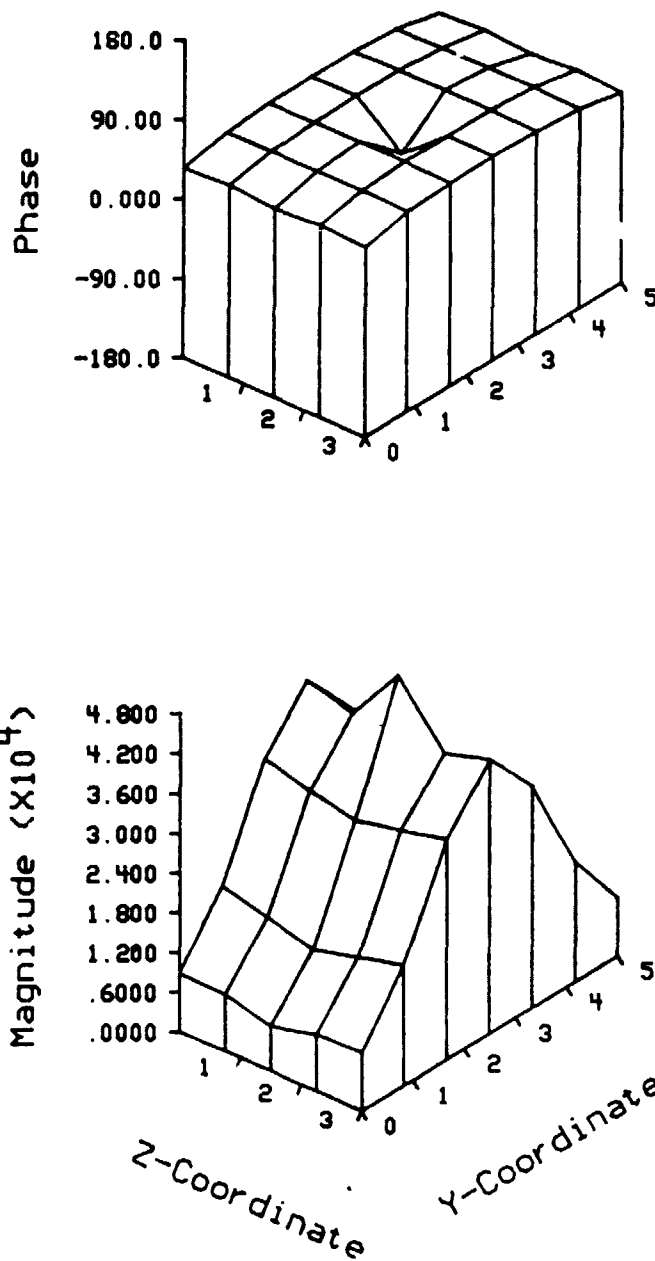


Figure 5.36 = Rectangular Cavity Pressure Distribution At $k=1.65$ (ZY Plane)

The third resonant pressure distribution is at a wave number of 2.06 (707 Hz). In the response of figures 5.28 through 5.30, two closely-spaced peaks appear between the wave numbers of 2 and 2.25. The first peak is the one at 707 Hz. Figures 5.37 through 5.39 are the pressure distributions of the third resonant condition. In figure 5.37, it seems as though a cosinusoidal variation exists along both the x and y directions. However, it is not entirely clear from the phase relationship that this is indeed the case. By examining figure 5.38, it becomes more obvious that just such a variation is present in the x direction. Similarly, the y direction variation is better viewed in figure 5.39. The resulting conclusion is that the (2,2,0) mode is the dominate mode at this frequency. Theoretically, the (2,2,0) mode occurs at a wave number of $\sqrt{\left(\frac{2\pi}{4}\right)^2 + \left(\frac{2\pi}{5}\right)^2} = 2.01$ (689 Hz). For the third resonance in the rectangular cavity response, the boundary element model located the resonant frequency with only a 3% upward shift.

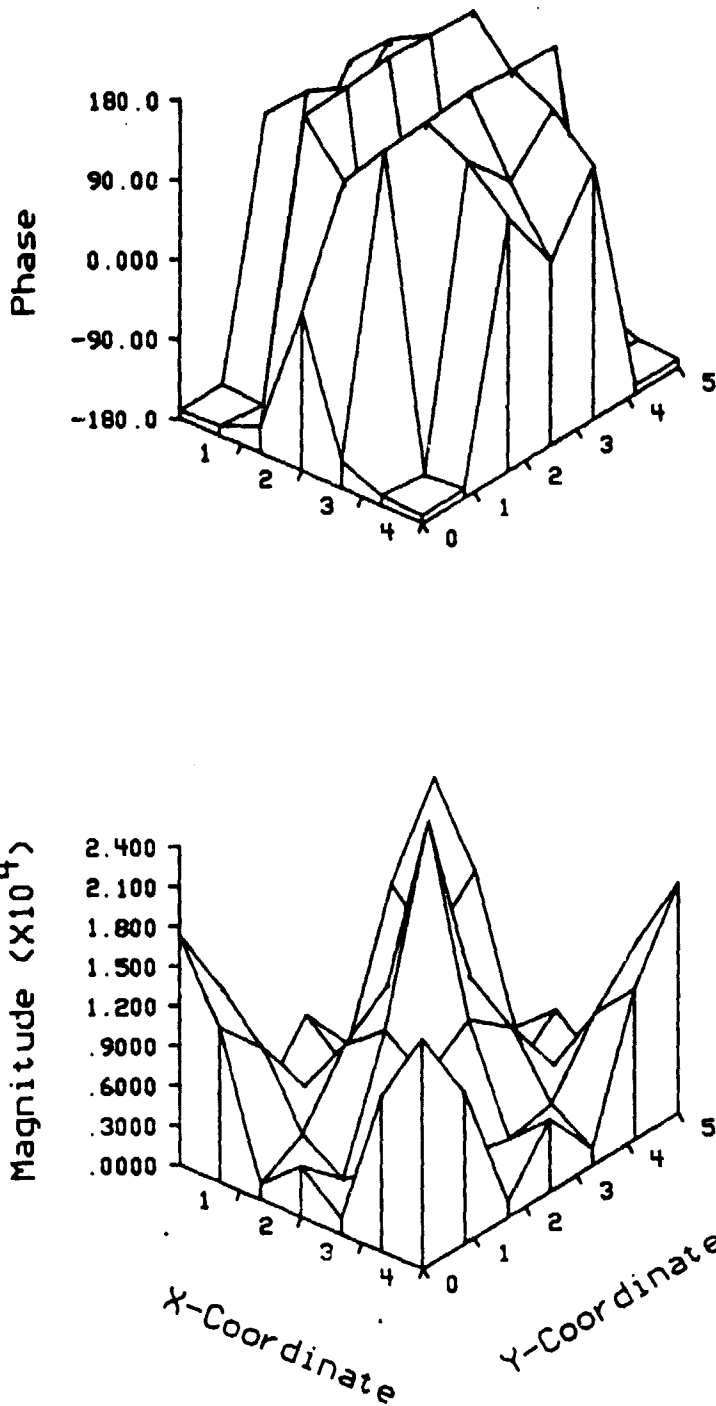


Figure 5.37 - Rectangular Cavity Pressure Distribution At $k=2.06$ (XY Plane)

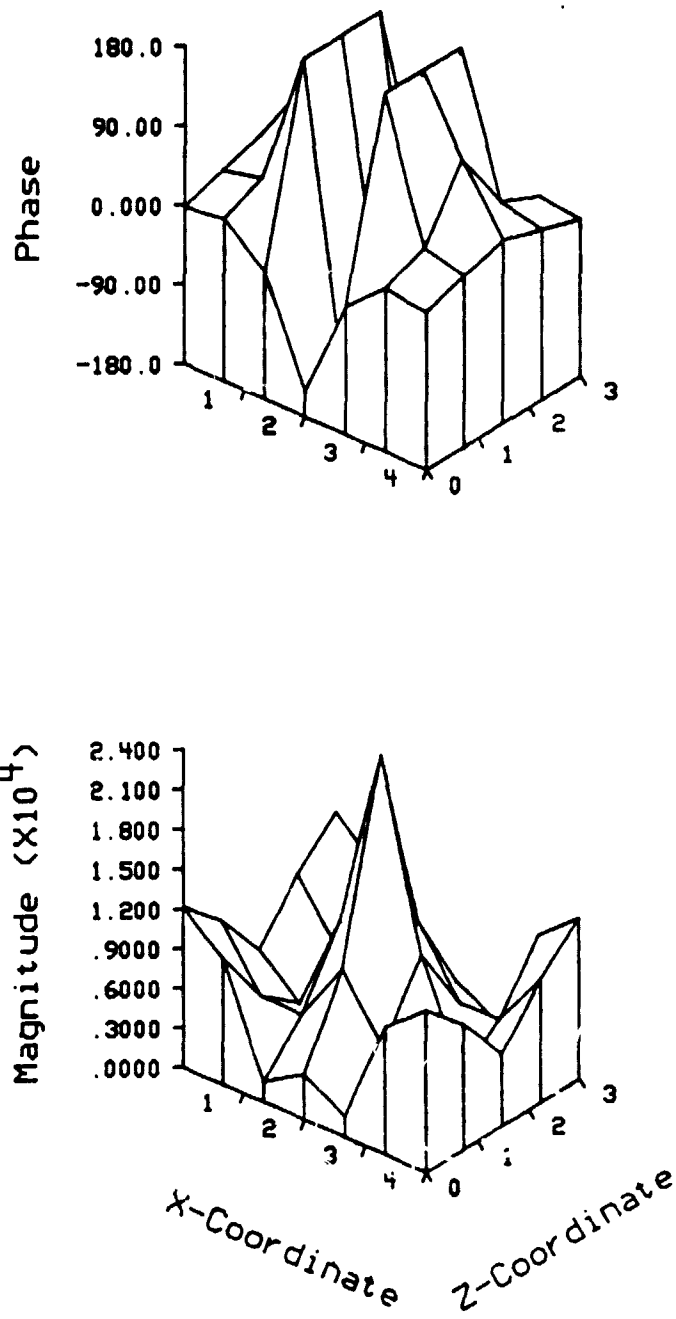


Figure 5.38 - Rectangular Cavity Pressure Distribution At $k=2.06$ (XZ Plane)

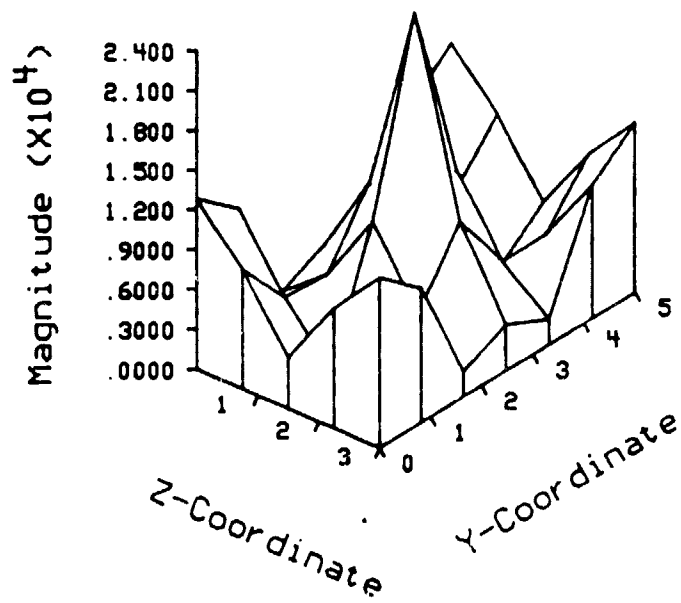
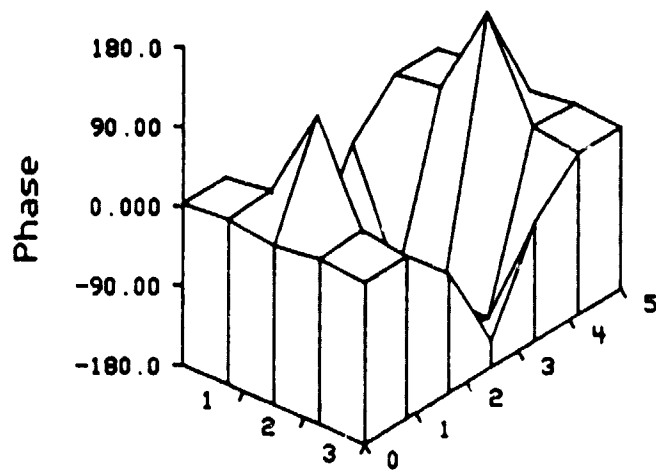


Figure 5.39 - Rectangular Cavity Pressure Distribution At $k=2.06$ (ZY Plane)

Although the pressure distribution will not be presented for the resonant peak at the wave number of 2.21 (758 Hz), some comments can be made regarding it. The next expected mode shape should be the (0,0,2) mode which, theoretically, is excited at a wave number of 2.09 (717 Hz). The numerically determined pressure distribution at 758 Hz was characteristic of the (0,0,2) mode but also retained the nature of the (2,2,0) mode which occurred at a slightly lower frequency. Because the two resonances are so closely related in terms of frequency, both the (2,2,0) mode and the (0,0,2) mode are apparent in the distribution at 758 Hz. A situation such as this is likely to happen whenever the modal density is high in a particular frequency range of interest.

A series of pressure distributions were generated for a non-resonant frequency of the rigid-walled rectangular cavity. The distributions in figures 5.40 through 5.42 are for a wave number of 1 (343 Hz) which is a frequency lower than the first resonant frequency of 460 Hz. The pressure distributions plainly show that at this non-resonant frequency, the applied source is the sole determinant of the pressure field characteristics. This type of distribution should be expected as all the resonant response will be low at this frequency.

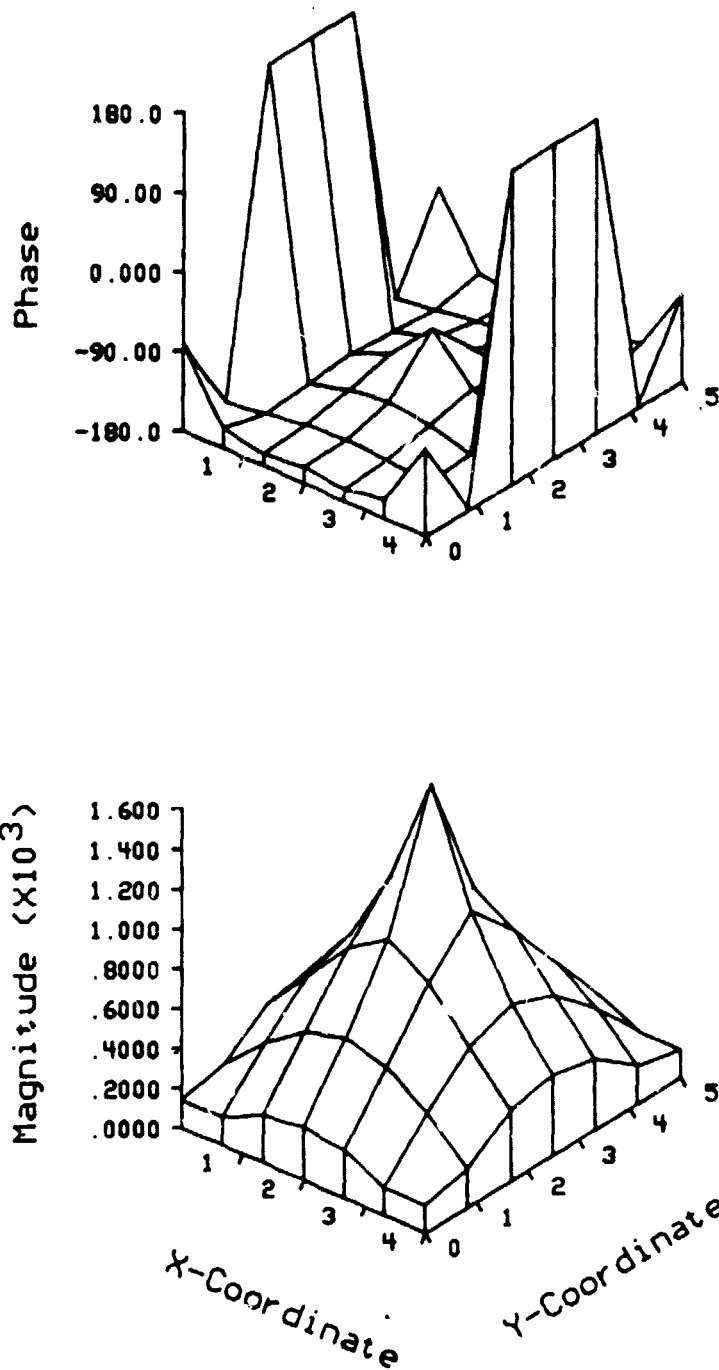


Figure 5.40 - Rectangular Cavity Pressure Distribution At $k=1$ (XY Plane)

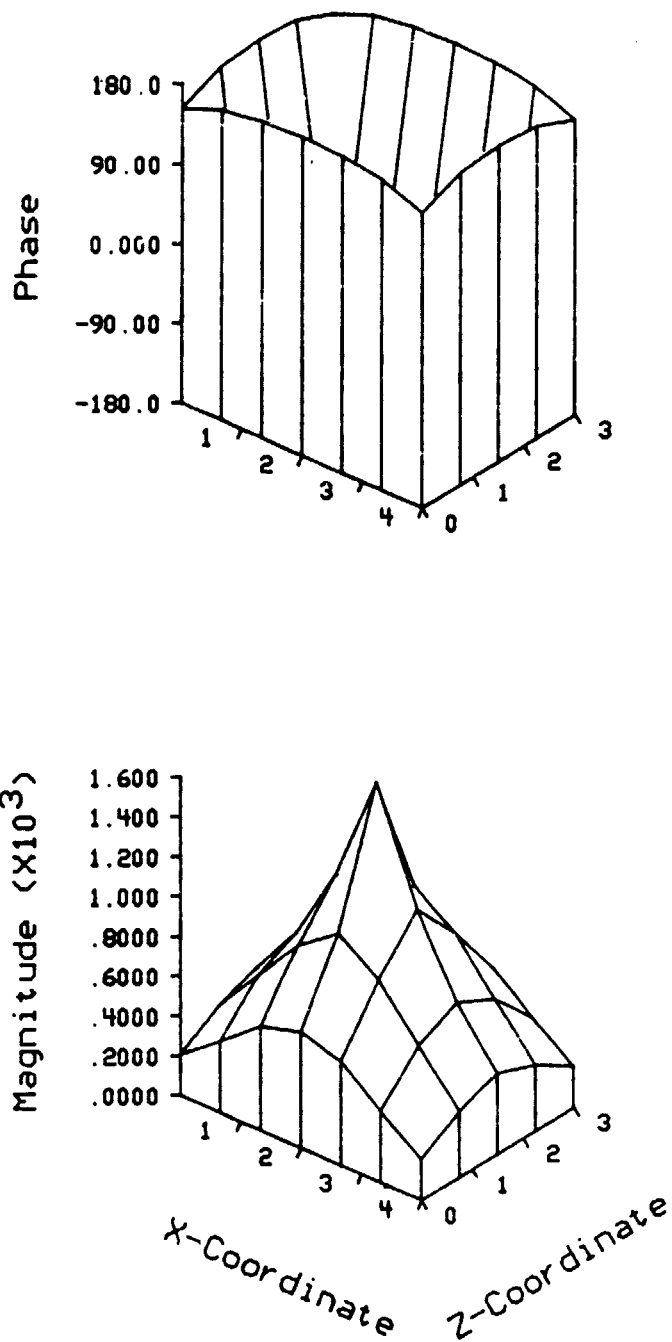


Figure 5.41 - Rectangular Cavity Pressure Distribution At $k=1$ (XZ Plane)

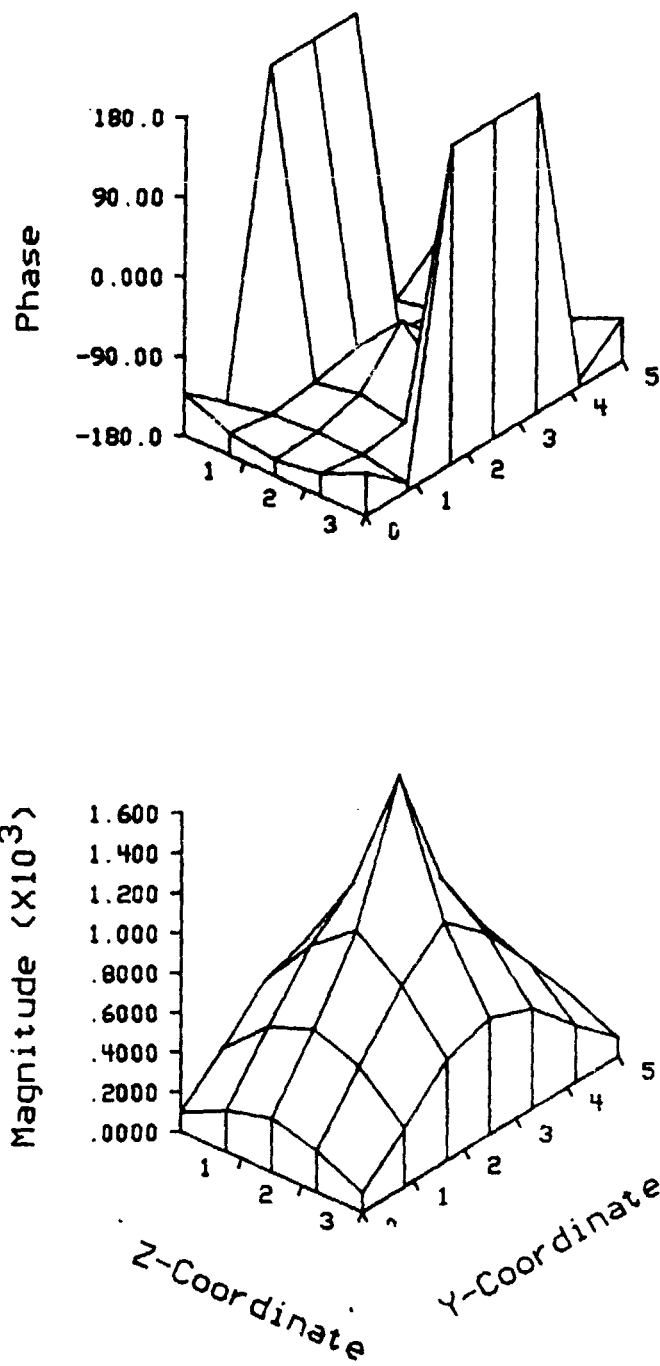


Figure 5.42 - Rectangular Cavity Pressure Distribution At $k=1$ (ZY Plane)

5.4 Summary

The first section of this chapter presented numerical results and, analytical results where applicable, of sound fields in a spherical cavity. Excellent correlation was obtained except in the low frequency regime. A hypothesis for the low frequency difficulties was presented and partially supported through literature references. Using the spherical cavity model, all three boundary condition types (pressure, velocity and impedance) and the applied source capabilities were verified. In addition, the sphere model was used to briefly examine the acoustical radiation prediction capabilities of the program for a pulsating sphere.

The remainder of the chapter presented results obtained for a 4x5x3 rectangular cavity. Three different techniques for modeling corners and edges were presented. The best of the three modeling techniques was to model the corners and edges by leaving slight gaps. A model of the cavity having gaps at the corners and edges was utilized to develop a cavity response and pressure distributions both on and off the resonant frequencies. The resonant frequencies were located and identified with good accuracy using the boundary element model.

CHAPTER 6

CONCLUSIONS

The objective for this research was to develop a numerical tool based on indirect boundary element theory to predict the sound field within an acoustical cavity. In addition, two additional features were desired. The first additional feature was that the three boundary condition types; pressure, velocity and impedance, be formulated and implemented in the development. Secondly, the implementation of acoustic point sources was desired.

A code to implement these objectives was developed and verified. In general, the conclusions which can be drawn from this experience are;

1. The indirect boundary element method is capable of all analyses for which direct boundary element methods have been demonstrated in the literature. In addition, IBEM techniques require only one boundary integral in most

cases. This will be more efficient than DBEM's in many instances.

2. Forced response in three-dimensional cavities is a straightforward application of boundary element methods. Corners and edges cause difficulties as they do with radiation problems. Further conclusions in this regard are included in the next paragraph.
3. Implementation of internal source capabilities is reasonably straightforward and potentially quite powerful in future applications such as active noise control. Boundary element methods are decidedly better than finite element methods for representing internal point sources since BEM's can accommodate singularities.
4. The application of impedance boundary conditions was successfully demonstrated. It should be pointed out that the formulation used in this development is not limited to locally reacting impedance.

One suggestion can be made regarding the problem with corners and edges evidenced in the rectangular box model. The application of a 'noncompatible' element may resolve these difficulties. A 'noncompatible' element is one in which the nodes of the element are not located along the edges of the element as for the isoparametric element used in this research but located internal to the element. By

locating the nodes, or the locations of the boundary conditions, within the element, the boundary conditions will never be situated at a boundary discontinuity. Thus, the 'free terms' in the velocity and impedance boundary condition equations will always maintain a value of $\pm\frac{1}{2}$ and, more importantly, the difficulties with the boundary discontinuities can be avoided.

The boundary element procedure developed for this research can be applied to noise source identification. Although this concept was not specifically pursued in the case studies, the identification of acoustical generators and optimization of the cavity acoustical characteristics can be guided with the application of this boundary element procedure.

In summary, it appears from this work that the indirect boundary element method should be the numerical method of choice for a large percentage of investigators interested in forced response problems in both interior and exterior domains. This is especially true when only a limited number of frequencies and response locations are desired.

LIST OF REFERENCES

LIST OF REFERENCES

- [1] A.K. Noor and W.D. Pilkey, editors, State-of-The-Art Surveys on Finite Element Technology, ASME, 1983.
- [2] R.J. Bernhard, "Using Structural Dynamics Code To Do Acoustic Finite Element Analysis", Herrick Laboratory Report 85-5, Purdue University, 1985.
- [3] C.-I J. Young and M.J. Crocker, "Prediction of Transmission Loss in Mufflers by the Finite Element Method", J. Acous. Soc. of Am., Vol. 57, No. 1, 1975, pp. 144-148.
- [4] C.-I J. Young and M.J. Crocker, "Finite Element Acoustical Analysis of Complex Muffler Systems With and Without Wall Vibrations", Noise Control Engineering, Sept.-Oct. 1977, pp. 86-93.
- [5] R.J. Astley and W. Eversman, "A Finite Element Formulation of the Eigenvalue Problem in Lined Ducts with Flow", J. of Sound and Vib., Vol. 65, No. 1, 1979, pp. 61-74.
- [6] A. Craggs, "The Application of Acoustic and Absorption Finite Elements to Sound Fields in Small Enclosures", Finite Element Applications in Acoustics, ASME, 1981, pp. 1-19.
- [7] L. Cederfeldt, "On the Use of the Finite Element Method on Some Acoustical Problems", ASME paper 81-WA/NCA-1, 1981.
- [8] S-F. Ling, J.F. Hamilton and J.J. Allen, "The Use of Two Dimensional Isoparametric Finite Elements for

- Determining the Sound Field in Axisymmetric Lined Ducts", Finite Element Applications in Acoustics, ASME, 1981, pp. 99-110.
- [9] G.R. Doyle, Jr. and L.L. Faulkner, "Three-Dimensional Finite Element Acoustic Pressure Analysis with Complex Impedance", Finite Element Applications in Acoustics, ASME, 1981, pp. 57-72.
- [10] A. Craggs, "An Acoustic Finite Element Approach for Studying Boundary Flexibility and Sound Transmission Between Irregular Enclosures", J. of Sound and Vib., Vol. 30, No. 3, 1973, pp. 343-357.
- [11] S.H. Sung, "Automotive Applications of Three-Dimensional Acoustic Finite Elements", SAE paper no. 810397, 1981.
- [12] P.K. Banerjee and R. Butterfield, Boundary Element Methods in Engineering Science, McGraw-Hill, London, 1981, p.4.
- [13] L.H. Chen and D.G. Schweikert, "Sound Radiation from an Arbitrary Body", J. Acous. Soc. of Am., Vol. 35, No. 10, 1963, pp. 1626-1632.
- [14] G. Chertock, "Sound Radiation from Vibrating Surfaces", J. Acous. Soc. of Am., Vol. 36, No. 7, 1964, pp. 1305-1313.
- [15] L.G. Copley, "Integral Equation Method for Radiation from Vibrating Bodies", J. Acous. Soc. of Am., Vol. 41, No. 4, 1967, pp. 807-816.
- [16] W. Williams, N.G. Parke, D.A. Moran and C.H. Sherman, "Acoustic Radiation from a Finite Cylinder", J. Acous. Soc. of Am., Vol. 36, No. 12, 1964, pp. 2316-2322.
- [17] L.G. Copley, "Fundamental Results Concerning Integral Representations in Acoustic Radiation", J. Acous. Soc. of Am., Vol. 44, No. 1, 1968, pp. 28-32.
- [18] A.J. Burton and G.F. Miller, "The Application of Integral Equation Methods to the Numerical Solution of Some Exterior Boundary-Value Problems", Proc. Roy. Soc. Lond., A.323, 1971, pp. 201-210.
- [19] H.A. Schenck, "Improved Integral Formulation for Acoustic Radiation Problems", J. Acous. Soc. of Am., Vol. 44, No. 1, 1968, pp. 41-58.

- [20] C.M. Piaszczyk and J.M. Klosner, "Acoustic Radiation from Vibrating Surfaces at Characteristic Frequencies", J. Acous. Soc. of Am., Vol. 75, No. 2, 1984, pp 363-375.
- [21] R.R. Smith, J.T. Hunt and D. Barach, "Finite Element Analysis of Acoustically Radiating Structures with Applications to Sonar Transducers", J. Acous. Soc. of Am., Vol. 54, No. 5, 1973, pp. 1277-1288.
- [22] J.J. Engblom and R.B. Nelson, "Consistent Formulation of Sound Radiation From Arbitrary Structure", J. of Appl. Mech., June 1975, pp. 295-300.
- [23] W.L. Meyer, W.A. Bell, B.T. Zinn and M.P. Stallybrass, "Boundary Integral Solutions of Three Dimensional Acoustic Radiation Problems", J. Sound and Vib., Vol. 59, No. 2, 1978, pp. 245-262.
- [24] A.F. Seybert, B. Soenarko, F.J. Rizzo and D.J. Shippy, "Application of the BIE Method to Sound Radiation Problems Using An Isoparametric Element", ASME paper no. 82-WA/NCA-1, 1982.
- [25] R. Seznec, "Diffraction of Sound Around Barriers: Use of the Boundary Elements Technique", J. Sound and Vib., Vol. 73, No. 2, 1980, pp. 195-209.
- [26] D.T.I. Francis, M.M. Sadek and S.A. Tobias, "Prediction of Acoustic Emission of Impact Forming Machines from Design Drawings", ASME paper no. 81-WA/NCA-5, 1981.
- [27] S. Vajpayee, M.M. Nigm and M.M. Sadek, "Acoustic Diagnosis of a Hydraulic Hammer", ASME paper no. 81-WA/NCA-8, 1981.
- [28] H. Benner and G.H. Koopmann, "Sound Power Prediction Using the Helmholtz-Kirchhoff Integral Equation", ASME paper no. 81-WA/NCA-4, 1981.
- [29] G.H. Koopmann and H. Benner, "Method for Computing the Sound Power of Machines Based on the Helmholtz Integral", J. Acous. Soc. of Am., Vol, 71, No. 1, 1982, pp. 78-89.
- [30] G.H. Koopmann and J.C. Perrand, "Crack Location by Means of Surface Acoustic Intensity Measurements", ASME paper no. 81-WA/NCA-6, 1981.
- [31] G.H. Koopmann and M. Mezache, "Radiation Characteristics of a Slender Box-Type Structure", ASME

paper no. 82-WA/NCA-9, 1982.

- [32] G.R.C. Tai and R.P. Shaw, "Helmholtz-Equation Eigenvalues and Eigenmodes for Arbitrary Domains", J. Acous. Soc. of Am., Vol. 56, No. 3, 1974, pp. 796-804.
- [33] T. Tanaka, T. Fujikawa, T. Abe and H. Utsuno, "A Method for the Analytical Prediction of Insertion Loss of a Two-Dimensional Muffler Model Based on the Transfer Matrix Derived From the Boundary Element Method", ASME paper no. 84-WA/NCA-7, 1984.
- [34] A. Sestieri, D. Del Vescovo and P. Lucibello, "Structural-Acoustic Coupling in Complex Shaped Cavities", J. Sound and Vib., Vol. 96, No. 2, 1984, pp. 219-233.
- [35] C.A. Brebbia and S. Walker, Boundary Element Techniques in Engineering, Newnes-Butterworths, London, 1980.
- [36] P.K. Banerjee and R. Butterfield, Developments in Boundary Element Methods - 1, Applied Science Publishers, London, 1979.
- [37] L.E. Kinsler, A.R. Frey, A.B. Coppens and J.V. Sanders, Fundamentals of Acoustics, Third Edition, John Wiley & Sons, New York, 1982, p.113.
- [38] W.A. Kaplan, Advanced Mathematics for Engineers, Addison-Wesley, Reading, Mass., 1981, p.475.
- [39] Op. cit., Ref. 35, pp. 33-34.
- [40] Op. cit., Ref. 12, p. 122.
- [41] Op. cit., Ref. 35, pp. 30-31.
- [42] Op. cit., Ref. 12, p. 52-53.
- [43] Op. Cit., Ref. 37, p. 111.
- [44] E.B. Becker, G.F. Carey and J.T. Oden, Finite Elements An Introduction Volume I, Prentice-Hall, Englewood Cliffs, New Jersey, 1981, p. 198.
- [45] Op. cit., Ref. 44, p. 93.
- [46] Op. cit., Ref. 44, p. 199.

- [47] Op. cit., Re.. 44, p. 190.
- [48] Op. cit., Ref. 35, p. 68.
- [49] H. Engels, Numerical Quadrature and Cubature, Academic Press, London, 1980.
- [50] D.J. Zimmerle and R.J. Bernhard, "Integration of Certain Singular Boundary Element Integrals for Applications in Linear Acoustics", Herrick Laboratory Report 85-21, Purdue University, 1985.
- [51] Op. cit., Ref. 37, p. 112-113.
- [52] Op. cit., Ref. 37, p. 163.
- [53] Op. cit., Ref. 37, p. 216.